UNIVERSITY OF SOUTHAMPTON

Faculty of Engineering and Physical Sciences
Zepler Institute

# Femtosecond Laser Written Diffractive Optical Devices

*by*

**Qi Sun**

*A thesis for the degree of*
*Doctor of Philosophy*

October 2021

University of Southampton

Abstract

Faculty of Engineering and Physical Sciences
Zepler Institute

Doctor of Philosophy

**Femtosecond Laser Written Diffractive Optical Devices**

by Qi Sun

This thesis presents the development of optical diffractive and scattering-based devices fabricated by femtosecond laser direct writing. Structures investigated include waveguides, Fresnel lenses, diffractive gratings and scattering chips. Firstly, the laser induced refractive index change was estimated as $7\times10^{-4}$ to $6\times10^{-3}$ for writing powers of $P_w$=35 mW to 55 mW in silica. It was determined by fabricating waveguides and analysing their mode field diameter. A new writing method for controlling laser induced stress distribution was developed for improving the uniformity of inscribed structures and reducing laser-induced damage. A 36% diffraction efficiency improvement for a 50/50 grating was achieved compared to the standard multiscan writing technique. A two-layer Fresnel lens with a focal efficiency of 55% was also demonstrated. The writing technique was applied to create an integrated waveguide structure within multi-core fibre, thus forming a directional bend sensor, for which a sensitivity of -1.4 nm/degree was achieved. For a diffractive Fresnel lens, the design and the propagation simulation were demonstrated. For the high aspect ratio structure, Bessel beam writing has been utilised for a faster fabrication. A new method for refractive index estimation has been tested with the blazed diffractive grating. The diffraction efficiency of the grating has been investigated in both silica and lead silicate, a 57% diffraction efficiency was achieved with Gaussian beam writing. Finally, a laser-fabricated scattering chip based on induced voids was presented in this thesis, with applications as a wavemeter, spectrometer, and interferometric distance sensor. The algorithm based on the correlation and singular value decomposition has been demonstrated.

# Contents

# List of Figures

# List of Tables

# Declaration of Authorship

I declare that this thesis and the work presented in it is my own and has been generated by me as the result of my own original research.

I confirm that:

1. This work was done wholly or mainly while in candidature for a research degree at this University;
2. Where any part of this thesis has previously been submitted for a degree or any other qualification at this University or any other institution, this has been clearly stated;
3. Where I have consulted the published work of others, this is always clearly attributed;
4. Where I have quoted from the work of others, the source is always given. With the exception of such quotations, this thesis is entirely my own work;
5. I have acknowledged all main sources of help;
6. Where the thesis is based on work done by myself jointly with others, I have made clear exactly what was done by others and what I have contributed myself;
7. Parts of this work have been published as: Sun, Qi, et al., Sci. Rep. 10.1 (2020): 1-8.
   Arrizabalaga, Oskar, et al., Sci. Rep. 10.1 (2020): 1-10.
   Sun, Qi, et al. CLEO, OSA, p. cm_5_1, 2019.
   Sun, Qi, et al. FiO. OSA, 2018. paper JW3A.12.
   Sun, Qi, et al. ACP, OSA, 2019. paper T4D.5.

Signed:..... Date:.....

## Acknowledgements

I would like to express my gratitude to all those who helped me during my PhD research.

I would like to thank my supervisor, Prof. Gilberto Brambilla, for his constant encouragement and guidance. I also owe my gratitude to Dr. Martynas Beresna, who has offered me valuable suggestions during the research and studies. I also gratefully acknowledge the help of Dr. Timothy Lee, for providing me with unfailing support and helping me developed a good research habit.

I acknowledge all the help and support from our research group members, Rand, Wanvisa, Yun, Andrei and Imran.

I would especially like to thank my amazing family for the love, support, and constant encouragement I have gotten over the years.

# Definitions and Abbreviations

| | |
|---|---|
| FZP | Fresnel Zone Plate |
| SHG | Second Harmonic Generation |
| NA | Numerical Aperture |
| MFD | Mode Field Diameter |
| LD | Laser Diode |
| BBO | Barium Borate |
| AMSE | Average mean square error |
| MCF | Multisore fibre |
| SCS | Differential scattering cross section |
| TLS | Tunable laser source |
| std. | Standard deviation |
| SVD | Singular value decomposition |
| PCA | Principle component analysis |
| WLI | White light interferometry |
| FOC | Fibre optic coupler |
| SLED | superluminescent diode |
| FC | Fibre collimator |
| BS | Beam splitter |
| PZT | Piezo-electric translator |
| OSA | Optical spectrum analyzer |
| FBG | Fibre Bragg grating |
| $\Delta n$ | Laser induced refractive index change |
| $h$ | Thickness of FZP |
| $N$ | Number of diffractive optics structure layers |
| $\Delta\phi$ | Induced phase change of FZP |
| $Z_R$ | Rayleigh range of Gaussian beam |
| $w_0$ | Beam waist size |
| $\lambda$ | Wavelength of light |
| $k$ | Wave vector of light |
| $U_1$ | Field distribution in source plane |
| $U_2$ | Field distribution in observation plane |
| $\alpha$ | Half-angle of axicon |

| | |
|---|---|
| $n_{ax}$ | Refractive index of axicon |
| F | Focal length of Fresnel zone plate |
| n | Number of rings on FZP |
| $r_n$ | Radius of nth zones of FZP |
| $D$ | Spatial density of laser pulses |
| $P_w$ | Average laser power before objective |
| $P_{w0}$ | Power after iris in improved SHG laser system |
| $k_B$ | Laser pulse burst |
| $s$ | Separation between each laser scan line |
| $v$ | Laser writing speed |
| $f$ | Repetition rate of femtosecond laser |
| $h_s$ | Thickness of each layer |
| $p_x$ | Dot spacing between scattering matrix in $x$ direction |
| $p_y$ | Dot spacing between scattering matrix in $y$ direction |
| $\delta\sigma$ | Principle stress difference |
| $R$ | Retardance |
| $C$ | Photoelastic coefficient between two principal stresses in silica |
| $T$ | Thickness of waveguide in $z$ direction |
| $R^+$ | Left side of the retardance distribution of waveguide |
| $R^-$ | Right side of the retardance distribution of waveguide |
| $\overline{R}(x)$ | Average of $R^+$ and $R^-$ |

# Chapter 1

# Introduction

## 1.1 Motivation

Based on femtosecond laser writing technique, my PhD research can be divided into two parts, which cover the design, fabrication and testing of (i) diffractive optical elements (includes Fresnel lenses and diffractive gratings) and (ii) scattering media based devices. The original motivation of the diffractive element research was to investigate a compact lens system for phone camera module. I found that inside a smartphone camera module, there exist many pieces of lenses; some modify the aberration, others for dispersion compensation. However, with the flexibility of fs laser writing, it is possible for us to combine two or more lenses into one substrate. For example, we can write a Fresnel lens into a traditional refractive lens for dispersion compensation, or even a single layer Fresnel zone plate with a variable index change could have a similar function. To achieve this, I need to have a good control of the laser induced refractive index change. In order to optimize the parameters of laser writing, I started with the waveguide which is a simple structure and easy to characterise.

For the scattering chip part, the motivation was to fabricate a spectrometer system based on scattering optics, rather than a simple diffraction grating as is often used in commercial spectrum analysers. The key advantage would be lower cost and more compact size, while maintaining fine resolution and a useful wavelength range. The system includes 3 parts: the light is first collected by the optical fibre and then scattered by the scattering medium, the speckle pattern is then captured by the camera. By analyzing the speckle pattern, I can then reconstruct the incoming light wavelength. With the help of the fs laser writing technique, it is possible to fabricate a highly stable and reproducible scattering medium embedded inside the silica to build a scattering based spectrometer system.

## 1.2 Background

In this chapter, there are three main sections, beginning with the background of femtosecond laser writing. It contains a discussion of the main factors (refractive index change, laser induced stress and structure dimensions) which affect optical performance of the laser written structures. The second part covers the background of the diffractive optics elements, which reviews the progress towards diffraction efficiency improvement for Fresnel zone plates (FZPs) and explains the theoretical background behind the propagation solution method for FZP simulations. The third part is the background of the optical scattering-based techniques for wavelength measurement.

### 1.2.1 Femtosecond Laser Writing

#### 1.2.1.1 Laser Writing Mechanism

About 25 years ago, the possibility of processing transparent materials with tightly focused femtosecond laser pulses was presented by Hirao's group Davis et al. (1996). Since then, femtosecond lasers have been widely investigated for material processing. The laser wavelength, often in the visible or infrared, is chosen so that the photon energy is typically much larger than the bandgap of the material. For example, the bandgap of silica is 9 eV while the photon energy for the 1030 nm source and 515 nm source are 1.2 eV and 2.4 eV respectively. A single photon thus cannot be absorbed in the linear interaction regime. However, when a tightly focused femtosecond laser pulse with high peak pulse intensity interacts with the material, nonlinear absorption can occur. Electrons in valance band can be excited by multi-photon absorption, by simultaneously absorbing several photons where the sum of their energies exceeds the bandgap energy. As long as the laser field is present, free carriers generated through photo-ionization will continue to interact with optical fields, which can further transfer the energy to other electrons through collisions, liberating them and resulting in the formation of more free carriers. The chain reaction of the collisions is called avalanche ionization Wright (1964). The high pulse energy is then transferred into the electrons and then lattice, causing local structural modifications. This will then result in a permanent change of the material's refractive index or even leave a void Gattass and Mazur (2008).

In fused silica, depending on laser parameters, there are 3 types of modifications (shown in Fig. 1.1): continuous modification, nanostructure formation and nano-void formation Hnatovsky et al. (2005a). Fig. 1.2 shows typical ranges for the pulse duration and pulse energy needed to achieve the different modification types in silica. Low intensity in a narrow processing window induces soft positive isotropic

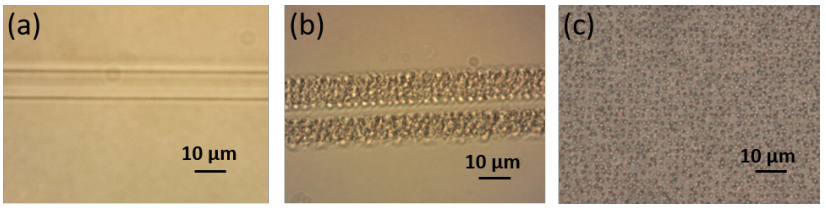


FIGURE 1.1: Femtosecond laser modification types: (a) Type I continuous modification, (b) Type II nanostructure formation and (c) Type III nano-void formation.

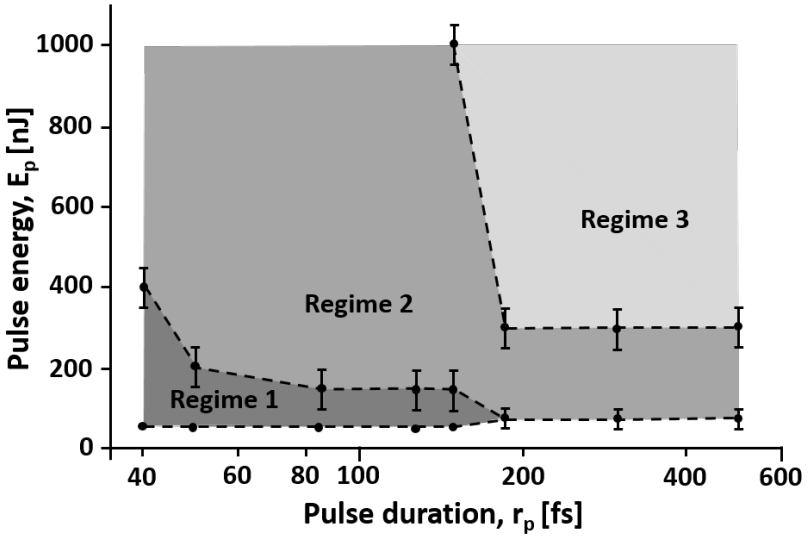


FIGURE 1.2: Typical pulse energy and duration ranges for regimes corresponding to the three modification types (continuous modification, nanostructure formation and nano-void formation) of fs laser writing in fused silica Hnatovsky et al. (2005b)

refractive index changes (type I) Davis et al. (1996); intermediate intensity results in birefringent anisotropic zones (type II) Sudrie et al. (1999); and high intensity generates voids in glass (type III) Glezer and Mazur (1997).

Due to the nonlinear nature of absorption, the laser-induced change is confined to material at the focal volume, which enables inscription of 3D structures including waveguides Pavlov et al. (2017), couplers Riesen et al. (2014), spatially variant waveplates Beresna et al. (2011) and diffractive optical elements (DOEs) Zhang et al. (2016b). Also, femtosecond laser writing has been applied in data storage Zhang et al. (2016a) and selective etching Bellouard et al. (2004); Hnatovsky et al. (2006).

The most common ultrafast laser used today for micromachining is the Ti:sapphire laser system (e.g. RegA series, Coherent Ltd.). It can produce 70-150 fs pulses with repetition rates up to tens of MHz and a pulse energy of 4 $\mu J$ at 250 kHz (which corresponds to maximum average power at 1 W). However, because of the short lifetime of the upper state, the Ti:sapphire laser system needs an external pump to reach a high intensity Beresna et al. (2014). As a result, the complexity of the system is increased. Also, although 1 W of average power is enough for fundamental laser

writing, for higher order harmonic generation, it will limit the harmonic power and hence laser modification range. Another popular laser micromachining system is the Yb:Fibre laser system (e.g. FCPA $\mu$Jewel, IMRA ltd.), which has a high-repetition rate up to 5 MHz (used for heat accumulation investigation in Eaton et al. (2005)). As a fibre laser, it has no external cooling system, which results in a small size. However, compared to solid-state lasers, the low output power (2 $\mu$J at 200 kHz which corresponds to 0.4 W) limits the usage range. Our choice of writing source is the Light Conversion Pharos 05-200-PP 1030 nm 200 fs laser, which is based on an Yb:KGW crystal. It has a moderate size with 6 W maximum average power at 200 kHz, which is sufficient for both fundamental and higher order harmonic generation writing.

#### 1.2.1.2 Laser Induced Refractive Index Change

For many applications, the induced refractive index change $\Delta n$ is the most important parameter. For waveguide writing, higher index change provides a tighter confinement of the propagation mode. For diffractive device writing, phase change, which is determined by laser-induced $\Delta n$, is important to the efficiency of the final device. The index change is highly dependent on the writing beam properties, including its pulse energy, pulse duration, pulse density, repetition rate, wavelength, scanning speed, focusing numerical aperture and the writing configuration. In this thesis, the pulse duration is fixed at 200 fs and the repetition rate normally used is 200 kHz, which is the maximum for our laser model. Furthermore, the second harmonic 515 nm wavelength is usually used for writing (rather than 1030 nm), as the shorter wavelength can be exploited to achieve a higher index change Shah et al. (2005) and offers potentially higher resolution. The remainder of the parameters will be optimised according to the optical device under fabrication.

Previous works have demonstrated that the index change can be controlled by energy deposition density and pulse duration Guo et al. (2004). For fused silica, the highest $\Delta n$ induced by a femtosecond laser reached $2.2 \times 10^{-2}$, which was achieved under tight focusing conditions (an oil immersion lens with NA = 1.25) and a short writing-beam wavelength of 522 nm Eaton et al. (2011). Depending on the substrate material, the maximum $\Delta n$ will also be different. In this thesis, fused silica glass will be used as the substrate in most experiments.

Pulse energy and writing speed also play an important role. By writing directional coupler inside a borosilicate sample, Streltsov et al. found that with constant pulse energy, changing the writing speed of the laser will change the magnitude of $\Delta n$ Streltsov and Borrelli (2001). They then presented research on $\Delta n$ versus pulse energy and laser writing velocity with both fused silica and borosilicate glass Streltsov and Borrelli (2002). Fig. 1.3 shows the results in fused silica. In Fig. 1.3(a), $\Delta n$ increases with pulse energy but saturated around $0.7\mu J$. In Fig. 1.3(b), $\Delta n$ shows a sharp

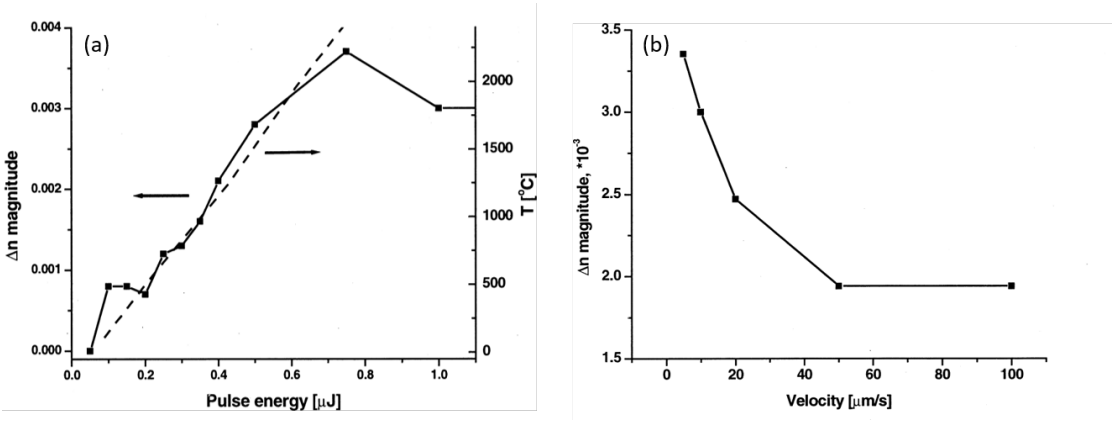


FIGURE 1.3: Dependence of $\Delta n$ in silica (Corning HPFS) verse (a) pulse energy with fixed laser scanning velocity of 10 $\mu m$ and (b) scanning velocity. The laser source has the wavelength of 800 nm, pulse duration of 40 fs and repetition rate of 20 kHz. Streltsov and Borrelli (2002).

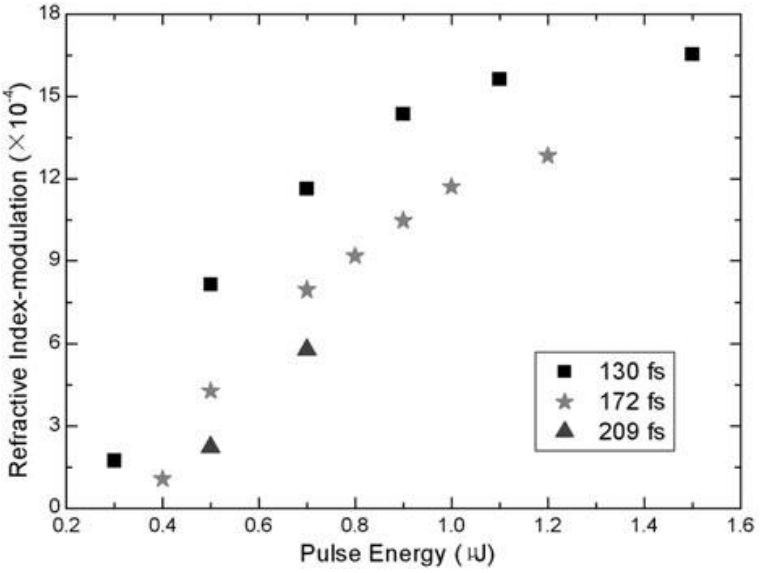


FIGURE 1.4: Refractive index modulation against pulse energy at pulse durations of 130 fs, 172 fs and 209 fs Guo et al. (2004).

decrease with increasing writing speed and the dependence became weaker above $\sim 50\mu m/s$. So for us, a moderate pulse energy and slow writing speed would be benefit for a higher $\Delta n$.

After that, Guo et al. investigated the effect of different pulse duration on $\Delta n$ by writing gratings inside fused silica Guo et al. (2004). The refractive index change was obtained by measuring the diffractive efficiency of the gratings. Fig. 1.4 shows the $\Delta n$ modulation increases with a shorter pulse duration. The highest $\Delta n$ obtained was $5.8 \times 10^{-4}$ and $1.6 \times 10^{-3}$ for a pulse duration of 209 fs and 130 fs, respectively. Their study indicated that the shorter laser pulse is more suitable for fabricating a higher refractive index modulation in fused silica.

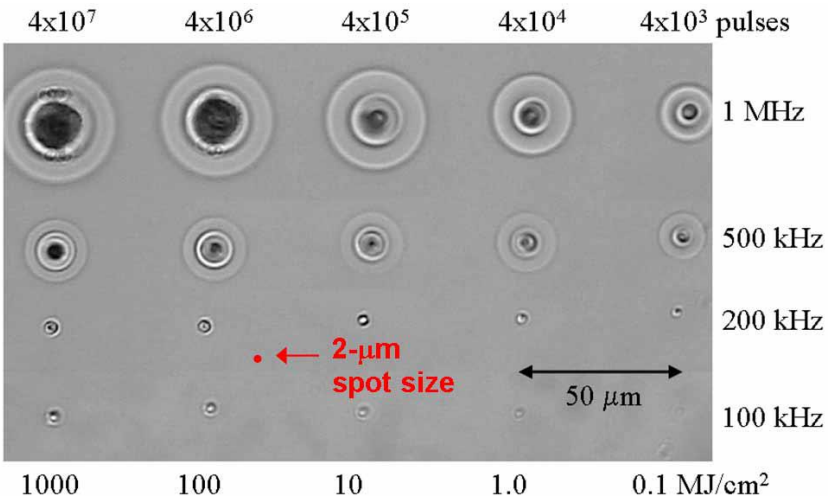


FIGURE 1.5: Static exposure tests in AF45 borosilicate glass with 450 nJ pulse energy from a 1045 nm femtosecond laser Eaton et al. (2005).

In this thesis, waveguide writing is an important tool for testing laser writing parameters and estimating laser induced refractive index change. In literature, there are two popular methods for waveguide fabrication: the first is the 'multiscan' Nasu et al. (2005) where multiple lines are written closely together to form a waveguide structure. Similar scanning techniques will be used to fabricate the waveguides in this thesis. For the second method, with the heat-accumulation effect, it is possible to form a waveguide with a single laser scan. As a result of heat accumulation, the refractive index structures are formed by the localized melting that is built up over many laser pulses, and then cools rapidly to resolidify after the laser exposure. In borosilicate glass, single scan method has achieved a low propagation loss at 0.062 dB/cm Chen et al. (2018). The single scan method requires a high repetition rate, for example, as for borosilicate glass, cumulative heating was evident at repetition rates greater than 200 kHz (shown in Fig. 1.5). However, for silica, the evidence of cumulative heating with a repetition rate up to 1 MHz is not found Eaton et al. (2005) (although such heating effects are observable using a faster 26 MHz repetition rate Osellame et al. (2005)). This is partly attributed to much higher bandgap energy (more than two times) of fused silica than borosilicate. For our system which has a repetition rate limited to 200kHz, we therefore must fabricate the waveguide by the multiple laser scanning method.

The quality of the laser written structure is not only dependent on the laser parameters discussed above. The arrangement of the laser induced stress can also contribute to a better optical device performance. During writing, laser radiation initiates a redistribution of the glass network leading to stress. The stress leads to a partial change in the refractive index Champion and Bellouard (2012), a decrease in the resistance to chemical corrosion and weakened mechanical performance of the materialMarcinkevičius et al. (2001). With different laser energy deposition levels,

these modifications can induce either a tensile or compressive stress distribution Bellouard et al. (2016) around the laser affected zone which will then result in a positive or negative change of refractive index. Because of the stress relaxation mechanism, at a high energy density level, the strong stress inside the material will lead to the formation of cracks Champion et al. (2013).

Thus for a laser written structure, the distribution of stress will play an important role. Typically, the material is modified by scanning the writing beam in a multiscan raster line pattern' Nasu et al. (2005), which can lead to an asymmetric stress distribution and even crack formation. However, applying different scanning techniques can better control the refractive index distribution and reduce the negative impact of the stress Sun et al. (2020).

Moreover, as a result of laser induced localized densification, the glass network is also rearranged by the surrounding stress in the laser affected zone Chan et al. (2001). With higher compressive stress, the Si-O-Si bond angle of silica decreases Sugiura and Yamadaya (1992) and the size of the $SiO_4$ ring is also reduced to a lower number Bellouard et al. (2008). For laser assisting etching (cite), higher index change Bellouard et al. (2008) and lower number $SiO_4$ rings Agarwal and Tomozawa (1997) tend to give a faster etching rate, so the stress control method could also be applied to improve the fs laser assisting etching process.

In this section, a parameter study of laser-induced refractive index change (including laser pulse energy, pulse duration, writing speed and repetition rate) has been investigated. This gives us a reference for choosing a suitable laser system and writing parameters. However, for the purpose of writing diffractive elements, we need to achieve a high $\Delta n$ while minimising writing time. Therefore, in the next section, we will talk about the use of a Gaussian-Bessel beam which has a much longer modification depth than a Gaussian writing beam.

#### 1.2.1.3 Gaussian-Bessel Beam Writing

Many applications require modification of large material volumes or writing high aspect-ratio structures, which is challenging but essential. Such examples include glass cutting, inscription of micro-fluidic channels, photonic circuits, and diffractive optical elements (DOEs). It is notable that for DOE performance, high diffraction efficiency requires that enough total optical phase change is provided by the structure. This is not only affected by $\Delta n$ but also physical thickness of the phase retarder. As the maximum $\Delta n$ in silica is typically $\sim 10^{-3}$, this implies that sufficient phase change can be achieved only with a thick enough layer of the modified material.

Defining the thickness of the DOE as $h$ and total phase change (i.e. phase difference between light propagating through modified and that through unmodified material)

as $\Delta\phi$, then we have

$$\Delta\phi = h \cdot \Delta n \cdot k \tag{1.1}$$

where $k = 2\pi/\lambda$ is the wave vector of incident light. From the equation, we see that the total phase change could be modified by not only $\Delta n$, but also the thickness $h$. With focused Gaussian beam writing, which is the most common beam shape used in material processing, the writing depth can be characterised by the Rayleigh range $Z_R$ near the focus, which is

$$Z_R = \frac{\pi n w_0^2}{\lambda} \tag{1.2}$$

where $n$ is the refractive index of the material, $w_0$ is the beam waist radius and $\lambda$ is the wavelength of the beam. During writing, to produce enough intensity for nonlinear modification, the beam is generally focused tightly with a high-NA lens. As a result, the beam size and thus the Rayleigh range become small, which limits the investigation of writing depth. To overcome this, the use of a Gaussian-Bessel beam can allow a much larger depth of field compared to the Gaussian beam Mikutis et al. (2013), Compared to the normal Gaussian beam, a Gaussian-Bessel beam has a much longer focal depth with more uniform intensity distribution as a result of its non-diffractive nature Durnin et al. (1988).

The Bessel beam was first noted by Durnin in 1987 Durnin (1987). The electric field of an ideal Bessel beam is described by a Bessel function of the first kind:

$$E(r, \phi, z) = A_0 exp(ik_z) J_n(k_r r) exp(\pm in\phi) \tag{1.3}$$

where $J_n$ is the $n^{\text{th}}$ order Bessel function, $r$ and $\phi$ are transverse and polar coordinates, $z$ is the coordinate in the propagation direction, $k_z$ and $k_r$ are the longitudinal and radial wavevectors. Fig. 1.6 shows the intensity profiles of zeroth and first-order Bessel beam.

A true Bessel beam cannot be created, as it is unbounded and would require an infinite amount of energy. Review article Duocastella and Arnold (2012) introduced approximation Gaussian-Bessel beam generation methods including using aperture, axicon, spatial light modulator, tunable acoustic gradient lens and optical fibre. For its highly efficient (low loss) and flexible purposes, we will focus on the axicon-generated Gaussian-Bessel beam in this section. For a shorter expression, I will use the term Bessel beam instead Gaussian-Bessel beam in the rest thesis.

The axicon, or a conical lens, was first demonstrated in 1954 by John H. McLeod McLeod (1954). It has a large apex angle and is designed to refract light along the optical axis. After passing through the axicon, the light (usually from a Gaussian input beam) will propagate across the optical axis and form a relatively extended depth of

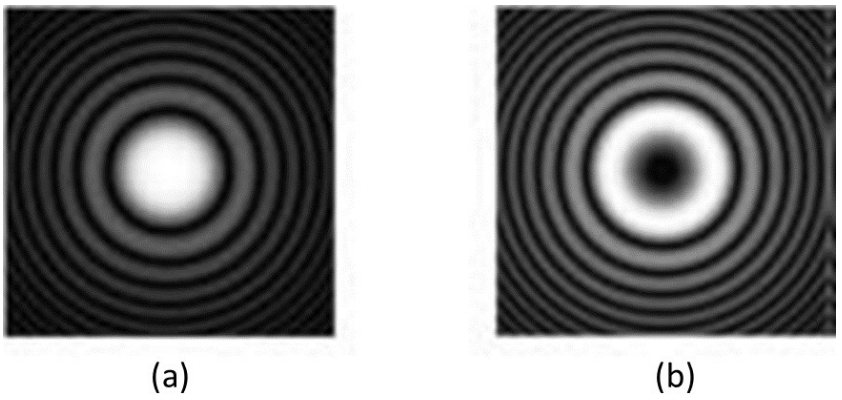


FIGURE 1.6: Intensity profiles of (a) zeroth order ($J_0$) Bessel beam and (b) first order ($J_1$) Bessel beam McGloin and Dholakia (2005).

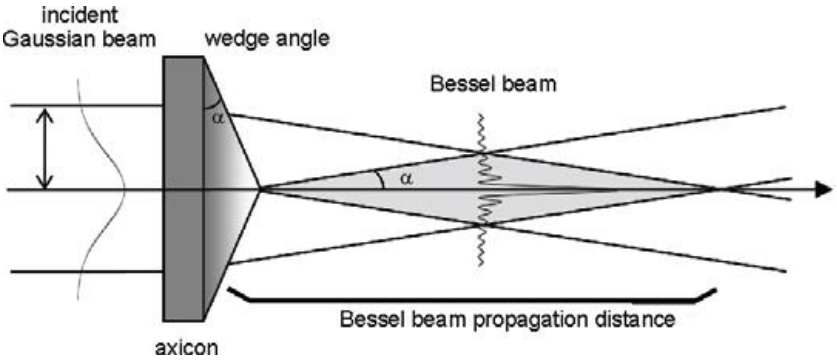


FIGURE 1.7: Schematic of Gaussian-Bessel beam generation with axicon Duocastella and Arnold (2012).

field. After the Bessel beam propagation distance (Fig. 1.7), a circular shape with constant ring thickness of the beam will be formed.

With their relatively long depth of field, Bessel beams were employed to fabricate high aspect ratio structures, e.g. microchannels Yashunin et al. (2015), nanocraters Courvoisier et al. (2009) and through-silicon vias He et al. (2017). For diffractive elements, Mikutis et al. demonstrated a high efficiency ($\sim$ 90%) Bessel beam written grating with the experimental set up in Fig. 1.8 Mikutis et al. (2013).

After the axicon, the depth of field $z^t_{max}$ of the Gaussian-Bessel beam can be calculated by

$$z^t_{max} = \frac{w_0 cos(\alpha_0)}{sin(\alpha_0)} \tag{1.4}$$

Here, $w_0$ is the radius of input Gaussian beam, and $\alpha_0 = \alpha(n_{ax} - n_0)/n_0$, where $n_0$ and $n_{ax}$ are the refractive indices of the ambient and axicon, and $\alpha$ is the axicon's half-angle measured in respect of its base (for 179° axicon, $\alpha$ is then 0.5°).

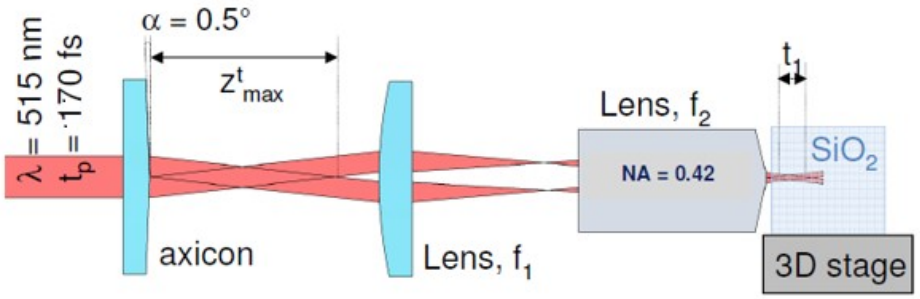


FIGURE 1.8: Schematic of experimental setup for Gaussian-Bessel beam generation. Bessel beam is formed by an axicon with an apex angle of 179° and then downsized by a telescope system Mikutis et al. (2013).

After the refocusing lens, they finally achieved a writing depth inside sample $t_1 = 116\mu m$ which corresponds to $z_t^{max}$=8.7mm. The experiment demonstrates the Bessel beam's advantage for high aspect-ratio structure writing, and we will investigate their application in writing DOEs with a similar set up in a later chapter.

### 1.2.2 Diffractive Optical Elements

#### 1.2.2.1 Fresnel Lens

Diffractive Fresnel lenses serve to focus light while occupying a much thinner volume than a traditional refractive lens. The ideal diffractive Fresnel lens design is essentially a phase mask offering the same phase profile as a traditional lens, but with all integer multiples of $2\pi$ rad subtracted. The resulting phase profile only varies between 0 to $2\pi$ rad and so can be implemented in a thin volume. In practice, the continuously varying nature of the phase profile is difficult to accurately fabricate, so the phase is discretised into two or more phase levels.

The simplest case, with 2 phase levels, is the Fresnel zone plate (FZP), which will be discussed first. The FZP is a diffractive element which consists of several circularly symmetric rings designed to produce constructive interference at the focal point. Fig. 1.9 shows the schematic of a phase FZP, where the blue rings are the laser modified zone with higher refractive index (e.g. modified silica), the grey rings are the unmodified material (e.g. unmodified pure silica). Note that there are in fact two different types of the FZP: amplitude and phase FZP For the amplitude FZP case, the blue zones would be transparent to the light while the grey zones would be opaque. In this thesis, we are focusing on the phase version of the FZP as it offers lower optical loss.

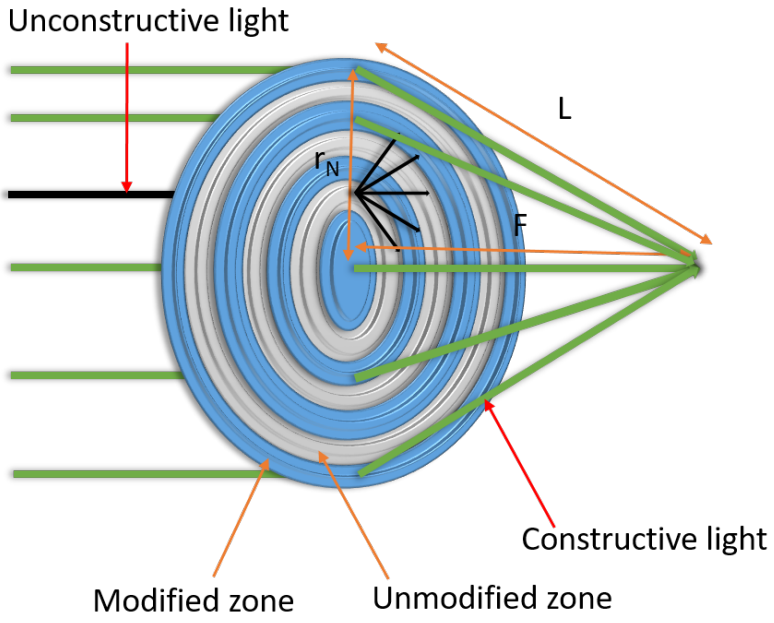


FIGURE 1.9: Schematic of phase FZP. Blue zones indicate laser modified material with higher refractive index and grey zones are unmodified material. With an appropriately designed phase profile, the FZP produces constructive interference at the designed focal point as indicated by green rays path. Black rays shows an example of destructive interference paths.

Constructive interference at the focal point requires the optical path difference between $L$ (optical distance between a given point on the FZP and focal point) and focal length $F$ to satisfy

$$\frac{(N-1)\lambda}{2} < L - F < \frac{N\lambda}{2} \tag{1.5}$$

where $N = \{1, 3, 5, \ldots\}$ is an odd integer corresponding to the ring number of the point on the FZP, $\lambda$ is the wavelength of incident light. Therefore, at the boundaries of the modified and unmodified zone, we have

$$L - F = \frac{N\lambda}{2} \tag{1.6}$$

According to the Pythagorean theorem, The optical path $L$ can be related to the radius of Fresnel rings $r_N$, since

$$L^2 = r_N^2 + F^2 \tag{1.7}$$

According to equation 1.6 and 1.7, we can calculate the radius of the nth zone, which is

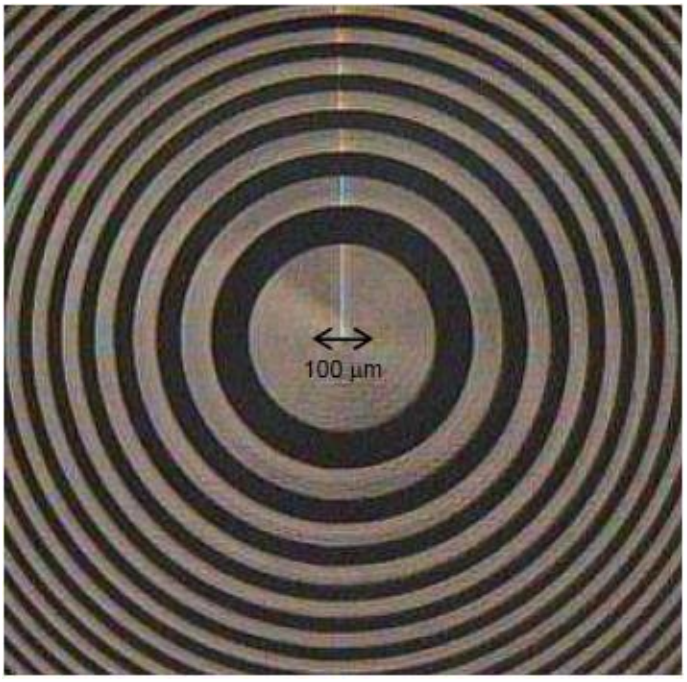


FIGURE 1.10: Microscope image of central part of FZP positioned between crossed polarisers. The FZP has maximum radius of 1 mm, 158 zones, and is designed for wavelength $\lambda_d$ = 632.8nm Bricchi et al. (2002). The FZP was positioned between crossed polarisers and the dark zones correspond to the even numbered Fresnel rings of pure unmodified silica, the bright rings are the birefringent laser processed areas.

$$r_N^2 = N\lambda(F + \frac{N\lambda}{4}) \tag{1.8}$$

The Fresnel zone plate is highly appreciated because of the small volume compared to a traditional lens, and ease of replication. The critical figure of merit of the FZP is the diffraction efficiency, i.e. the ratio of power in the central focal peak to the total incident power. The demonstration in Bricchi et al. (2002) of a Fresnel zone plate provided a high diffraction efficiency of 39% at 404 nm, which is close to the theoretical limit of 40.5% (Fig. 1.10).

For longer wavelengths at 550 nm and 642 nm, 34% and 26% of best efficiency are observed. However, the efficiency is polarisation dependent; for the other polarisation direction, the diffraction efficiency for 404 nm is reduced to 11%. FZPs can indeed reduce the amount of material required for fabrication compared to normal refractive lens, but with the efficiency limit of 40.5%, it is not sufficient for most optical applications.

For a perfect Fresnel lens, the maximum induced phase change is $2\pi$. However, for the FZP, which has limited phase steps, the FZP design divides $2\pi$ phase change into several levels, and the more levels the FZP has, the closer the efficiency can get compared to a perfect Fresnel lens (more details will be discussed in Chapter 4). For

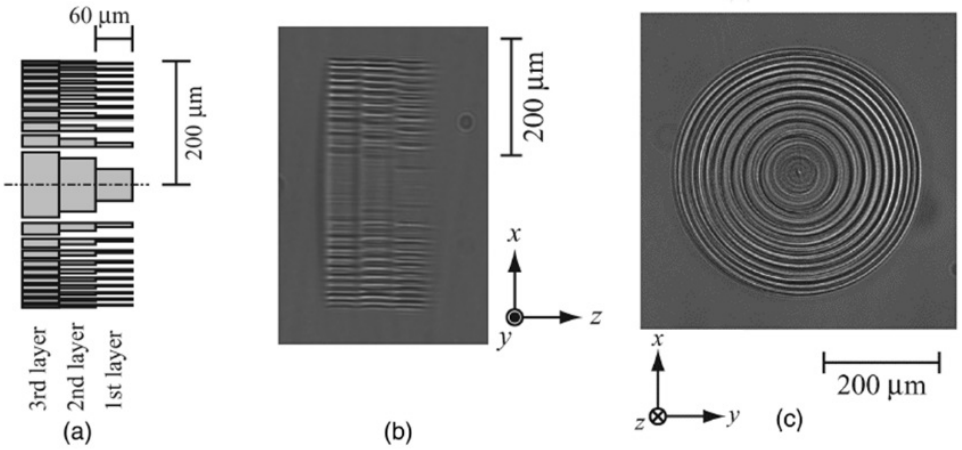


FIGURE 1.11: (a) Four-level (three-layer) phase diffractive lens. (b) Cross-section and (c) top view Yamada et al. (2004).

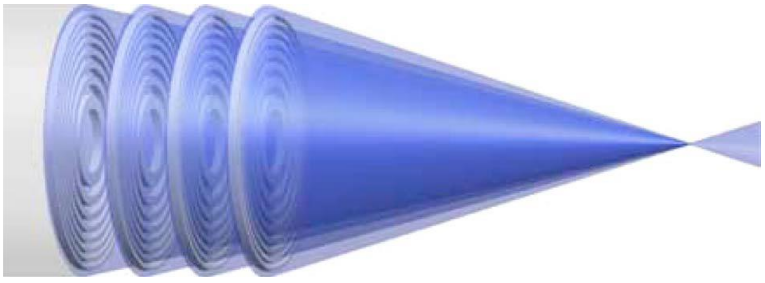

FIGURE 1.12: Example of a volume Fresnel zone plate having four FZP layers Srisungsitthisunti et al. (2009).

higher efficiency FZPs, Yamada et al. demonstrated a two-level diffractive lens with maximum efficiency of 37.6% and four-level lens (Fig. 1.11) with the efficiency of 56.9% for 632.8 nm inside synthesised silica Yamada et al. (2004).

With a multilayer FZP, the efficiency will significantly increase. However, there exists a trade-off between fabrication time and efficiency. With a relatively low writing speed of $5\mu m/s$, to write a $400\mu m$-diameter 4-level lens, the fabrication time is extremely long and requires 21 hours. Long writing time limits the practical use of this technique.

After that, Srisungsitthisunti et al. fabricated a volume zone plate, which is the combination of several normal FZPs in a coherent way (Fig. 1.12). To reduce the fabrication time, they replaced each full ring of each zone to central ring. This reduced the fabrication time for each layer to 40-60min. With an 8-layer volume zone plate, the efficiency increased to 71.5% Srisungsitthisunti et al. (2007).

From the examples reviewed in this section, the multilayer FZP will indeed improve the diffraction efficiency. To study the efficiency of FZPs, in next section, we will introduce a beam propagation method for simulating FZPs.

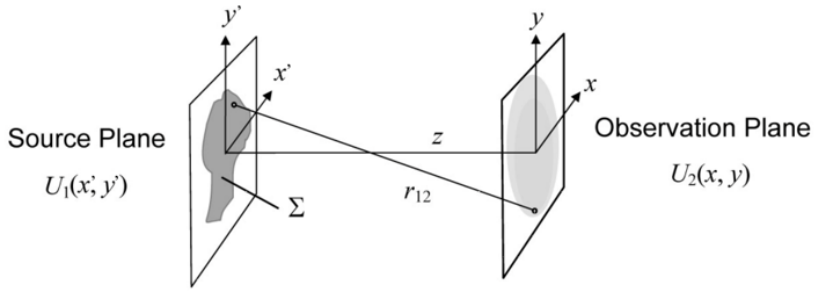


FIGURE 1.13: Light from the source plane propagates onto the observation plane according to the RS-equation Voelz (2011).

#### 1.2.2.2 Simulation Theory

According to the Huygens-Fresnel principle, every point on a wavefront is itself the source of spherical wavelets. In our case, the source plane $U(x', y')$ is the FZP, and to calculate the field at the observation plane which, we need to sum up all the contributions from point sources on source plane.

Using the first Rayleigh-Sommerfeld (RS) diffraction solution Voelz (2011), as we are using 1D model, we can calculate the one-dimensional field in a distant observation plane by

$$U_2(x) = \frac{z}{j\lambda} \int_{\Sigma} U_1(x') \frac{exp(jkr_{12})}{r_{12}^2} dx' \tag{1.9}$$

$U_1(x')$ and $U_2(x)$ are the field distributions in source plane and observation plane respectively. $\lambda$ is the optical wavelength; $k$ is the wavenumber; $z$ is the distance between the centres of the source and observation coordinate systems. $r_{12}$ is the distance between a position on the source plane and a position in the observation plane. $x'$ is the variable of the integration, and the integral limits correspond to the region of the source $\Sigma$.

When the observation plane and source plane are parallel, the equation becomes a convolution integral, which is

$$U_2(x) = \int U_1(x') h(x - x') dx' \tag{1.10}$$

where

$$h(x) = \frac{z}{j\lambda} \frac{exp(jkr)}{r^2} \tag{1.11}$$

And modelling the field in one transverse direction, $x$, propagating along the longitudinal direction $z$, we have:

$$r = \sqrt{z^2 + x^2} \tag{1.12}$$

The convolution integral is time-consuming to evaluate in the space domain, and instead it is quicker to solve by fast Fourier transform according to Fourier convolution theorem

$$U_2(x) = \mathcal{F}^{-1}\{\mathcal{F}\{U_1(x)\}\mathcal{F}\{h(x)\}\} \tag{1.13}$$

An equivalent expression is given by

$$U_2(x) = \mathcal{F}^{-1}\{\mathcal{F}\{U_1(x)\}H(f_X)\} \tag{1.14}$$

The Rayleigh-Sommerfeld transfer function is then given by

$$H(f_X) = exp(jkz\sqrt{1 - (\lambda f_X)^2}) \tag{1.15}$$

The only requirement for this expression is $r \gg \lambda$, which means the distance between the source and observation position must be much greater than the wavelength. Since our FZP is designed for the compact camera module, the focal length is about 1 cm; therefore, the requirement can be easily achieved in our case.

### 1.2.3 Scattering Based Optical Devices

Accurate wavelength measurement is fundamental to a wide range of applications encompassing bio-molecular and chemical fingerprinting, materials analysis, as well as terrestrial and astronomical remote sensing. The conventional approach for extracting spectral information relies on angular dispersion, for example via a diffraction grating, which spatially separates the spectral components so their respective powers can be measured. The resolution depends on the distance between the dispersive element and the detector. Conventional grating based spectrometers thus require large footprints or complex setups to fold the optical path. An alternative approach is to exploit scattering rather than dispersion to implement spatial mapping of spectral components. Large spectral separation can be achieved within a much smaller volume as scattering effectively folds the optical path. The light field is split into multiple spatial modes as it propagates through scattering medium. The

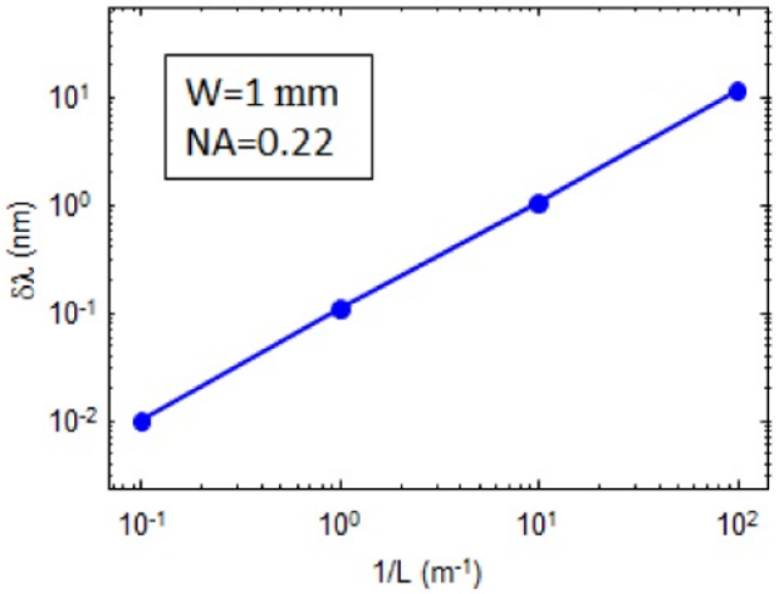


FIGURE 1.14: The resolution of the multimode fibre based spectrometer vs the length of the fibre Redding et al. (2013b).

interference of the modes produces an intricate speckle pattern, which despite appearing random, is deterministic and highly wavelength dependent.

Scattering spectrometers have been demonstrated using several different scattering elements. Speckle spectrometers reaching a very fine resolution (1 pm) were demonstrated using a hundred meters of multimode fibre Redding et al. (2014), where the speckle pattern is formed by excitation and subsequent beating of many higher order modes. The resolution in this arrangement is proportional to the length of the fibre. Fig. 1.14 shows the relation between the resolution of the multimode based fibre and the the length of the fibre.

To achieve a 0.1 nm resolution, at least 1 m of fibre is required Redding et al. (2013b). Unfortunately, the long length of the fibre makes it susceptible to environmental perturbations leading to temporally unstable speckle patterns. As the mode coupling and beating which produces speckles is highly dependent upon the exact fibre configuration, these systems require constant re-calibration and must remain unchanged after the calibration for each test Redding and Cao (2012). For integrating sphere based spectrometer systems Metzger et al. (2017), although sub-femtometer resolutions can be obtained, the large size limits applications to specialist and laboratory settings.

Much better performance should be achievable by exploiting a compact scattering medium which would be evenly affected by the environment, thus producing just a uniform detuning in the worst case scenario.

In 2013, a compact spectrometer chip based on scattering medium was proposed to increase the optical path length of light Redding et al. (2013a), allowing better spectral resolution within the same physical distance. However, as the scattering medium is designed in a single plane, the chip can only operate in 2 dimensions. Later, a compact 3D wavelength meter using an alumina drop was demonstrated Mazilu et al. (2014). By analysing the intensity pattern caused by the multiple scattering in the drop, the illumination wavelength could be determined with 13 pm accuracy. However, the higher spectral resolution also comes with a trade-off of high sensitivity to vibrations and alignment drifts. It is therefore important to maintain stability while adapting the level of scattering to optimally match the required spectral resolution for the application. In this thesis, an alternative form of scattering spectrometer has been proposed Sun et al. (2019), relying on the multiple scattering present in highly disordered bulk media to encode spectral information in complex wavelength-dependent speckle patterns. The disordered medium is fabricated by fs laser writing to induce a permanent scattering matrix in silica, with a high level of stability and reproducibility.

## 1.3 Thesis Overview

In the following Chapter 2, fundamental parameters for laser writing will be discussed, and the laser writing setup and the component functions will be explained.

Chapter 3 aims to find the effects of different laser parameters on the resulting glass material modification properties by performing tests to inscribe straight waveguides under different settings. We will evaluate the refractive index change of written waveguides with its mode field diameter (MFD). Furthermore, by improving the waveguide writing method, a stress control technique for fs laser written structures will be discussed. Aside for helping us to evaluate the induced index change, the waveguide structures themselves have numerous applications, which we demonstrate by presenting a waveguide assisted multicore fibre directional sensor.

In Chapter 4, having estimated the $\Delta n$ induced by laser writing, we will start to design, fabricate and test the femtosecond laser written Fresnel lens. We will first simulate the Fresnel zone plate in MATLAB to determine the focal properties and diffraction efficiency. Then for experimental writing, the suitability of Gaussian and Bessel inscription beams will be compared. Next, the focal and imaging characterisations of the written FZP will be evaluated at different wavelengths and the diffraction efficiency will be also measured. Finally, by inscribing and characterising diffractive gratings, an alternative method for estimating induced index will be presented.

In Chapter 5, the main purpose of the work is to implement a more compact spectrometer based on exploiting the benefits of a scattering medium, which can be engineered using laser direct writing. A femtosecond laser pulse, tightly focused in silica glass, induces a spherical shock wave, which disrupts the material creating a nanovoid without any collateral damage. Due to the high refractive index contrast between the void and substrate, strong optical scattering can be achieved.

In Chapter 6.1, the main future work fields are discussed. For the diffractive elements, we could integrate the Fresnel lens into the traditional lens by utilising the flexibility of fs laser writing. For the scattering chip, we could use it as a ”light converter” which converts the strain, temperature and polarization state into speckle pattern.

# Chapter 2

# Experimental Setups for Laser Writing and Characterisation

In this chapter, the design and practical implementation of the experimental setups used for laser inscription and characterisation of the fabricated samples will be outlined. Fundamental parameters for laser writing will be discussed, and the laser writing setup and the component functions will be explained. The fs laser written optics characterisation setup in this thesis will be presented, including waveguide output mode characterisation, Fresnel lens focal and imaging property characterisation, grating diffraction efficiency characterisation and scattering chip based wavelength and surface position reconstruction characterisation.

## 2.1 Femtosecond Laser Writing System

### 2.1.1 Laser Writing Parameters

Our writing source is a Pharos 05-200-PP femtosecond laser from Light Conversion Ltd., Lithuania, with an operating wavelength of $\lambda$=1030 nm, $\tau$=200 fs pulse duration and a variable repetition rate up to $f$=200 kHz. The maximum average power varies with repetition rate; e.g. $P_w$=6 W at $f$=200 kHz, and $P_w$=1 W at $f$=1 kHz. Inscription is performed with either the 1030 nm fundamental beam or its second harmonic at 515 nm. In both cases, we normally operate at 200 kHz. The power greatly exceeds the requirements since only 1$\sim$1.5 W is needed if writing with the second harmonic beam, or $<$100 mW if writing with the fundamental beam.

During laser writing, the main parameters are numerical aperture (NA) of the objective lens, density $D$ (pulses/mm) of laser pulses along a scanline, pulse energy $E_p$ (nJ), average laser writing power $P_w$ before the sample, laser pulse burst $k_B$ (repeat

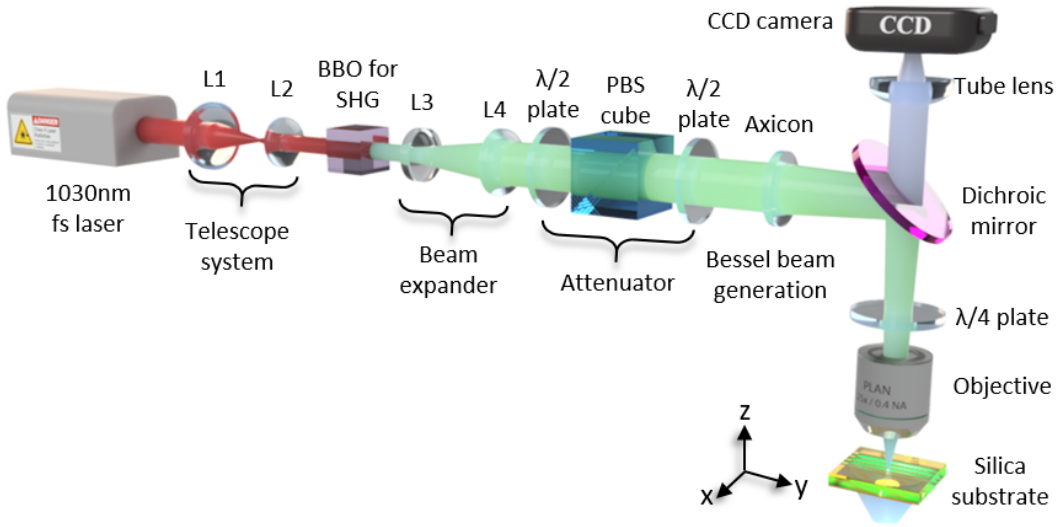


FIGURE 2.1: Laser writing system showing second harmonic generation, beam expander, attenuator and Gaussian-Bessel beam generation. An axicon or conical lens is used to produce Bessel beam Sun et al. (2018); for writing with a focused Gaussian beam, it is not required.

shots/pulse) (number of repeated pulses fired in same spot for each pulse point along scanline) and writing speed $v$ (mm/s). Note that $E_p$ is related to the femtosecond laser repetition rate $f$ and $P_w$ as Eq. 2.1:

$$E_p = P_w / f \tag{2.1}$$

and $D$, $v$ and $k_B$ are related to $f$ as Eq. 2.2:

$$D \cdot k_B \cdot v \leq f \tag{2.2}$$

since the minimum time between pulses of $1/f = 5\mu$s from the laser limits how fast the inscription can scan while still being able to achieve a given pulse density and pulse burst.

### 2.1.2 Laser Writing Setup

Figure 2.1 shows the schematic of the laser system writing setup. In this thesis, three different types of fs laser written structures are discussed: waveguides, diffractive elements and scattering chips. The fundamental 1030 nm beam is only used for the waveguide writing, and 515 nm beam for the others. The Bessel beam generation section is only used for writing the diffractive elements, as the rest use a focused Gaussian writing beam. Besides these differences, the remainder of the setup is similar for all applications discussed in this thesis.

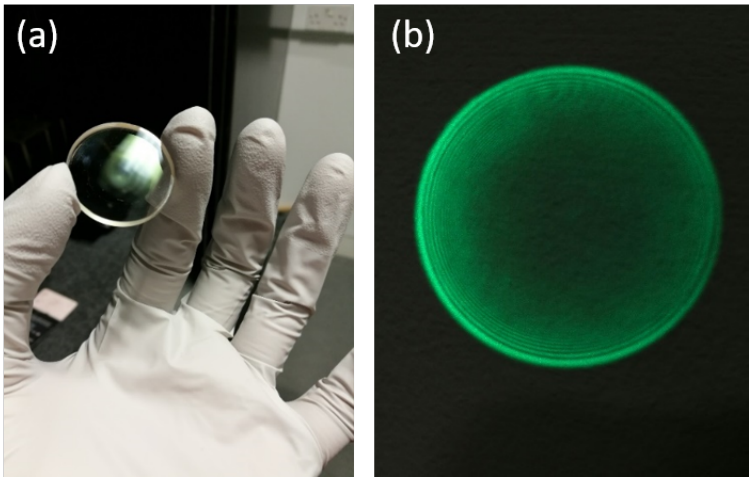


FIGURE 2.2: (a) Photograph of axicon and (b) Bessel rings generated from passing the 515 nm Gaussian beam through the axicon.

Firstly, the beam from the laser output passes through a second harmonic generation (SHG) system which contains a BBO crystal to convert the 1030 nm wavelength laser output into a 515 nm laser beam. To improve the SHG conversion efficiency, the pump intensity is first increased by a telescope system to halve the beam width.

After the SHG generation box, as the beam was halved by the preceding telescope system, there is an expander system which re-expands the 515 nm beam by a factor of 5 to a final beam diameter of $\sim$10 mm. Using a wider beam has the advantage that only the more uniform central portion of the beam is passed through the objective; the irregular parts at the periphery of the beam spot (caused by passing through additional optics needed for SHG) do not enter the objective.

Next, the beam passes through a computer-controlled half-wave plate and polarising beam splitter cube, which function together as an attenuator and enables us to easily control the laser power during the writing. After the waveplate, we generate the Bessel beam with an axicon (Fig. 2.2(a)) if needed. Our plano-convex axicon is the 1-APX-2-VIS-J254-P from Altechna Ltd., with an apex angle of 179°, 25.4 mm diameter and 3.5 mm thickness, which allows us to produce the Bessel rings shown in Fig. 2.2(b).

After the Bessel beam generation, the beam delivery section of the writing system is shown in Fig. 2.3. The femtosecond laser beam is delivered by a series of mirrors onto the objective lens which focuses onto the sample. The quarter waveplate is used here for circular polarisation generation. 3D writing is possible as the objective lens and sample are mounted on $z$ and $x$-$y$ translation stages, respectively. The $x$-$y$ stage (ANT130-160-XY, Aerotech Ltd.) has a travel distance of 160 $\times$ 160 mm with a resolution of 1 nm and $<$1 nm in-position stability. The $z$ stage (ANT130LZS, Aerotech Ltd.) has a resolution of 2 nm and $<$2 nm in-position stability. Both stages are driven from an Aerotech A3200 controller.

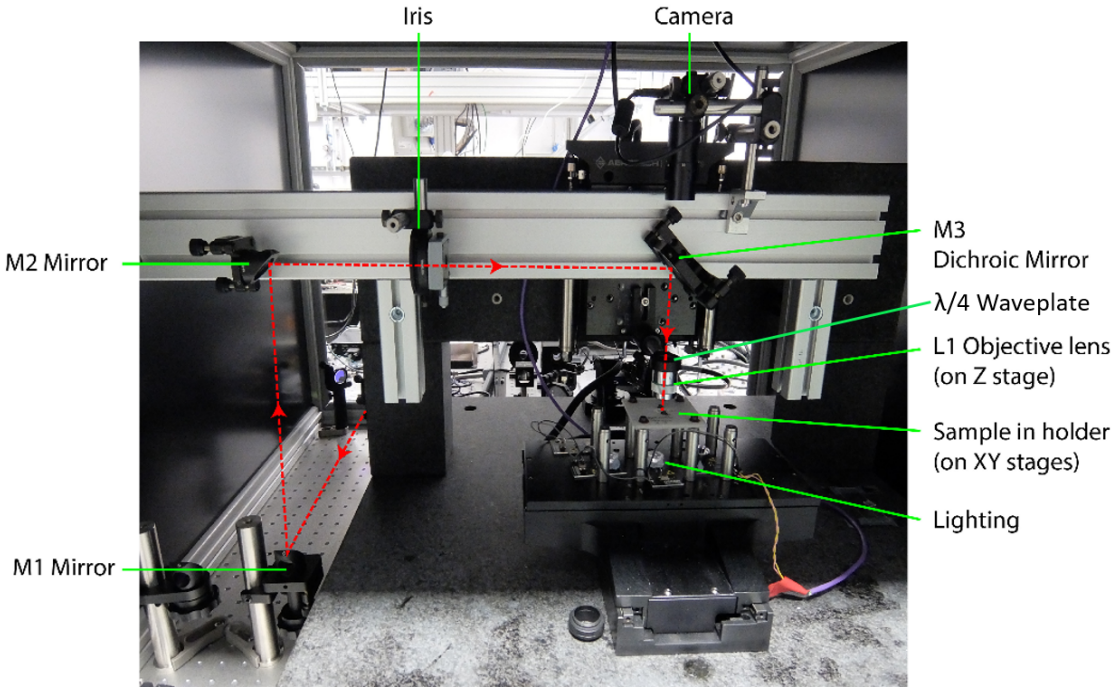


FIGURE 2.3: Beam delivery section of femtosecond laser writing system, located after Bessel beam generation.

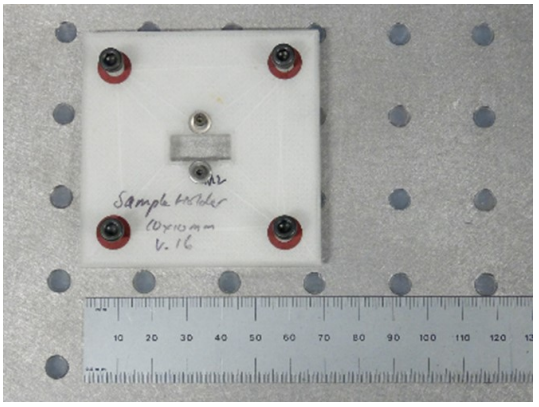

FIGURE 2.4: 3D printed holder for securing sample onto stages during laser writing.

Our sample holder was made by our 3D printer based on a design which can be optimised for different sample sizes (see Fig. 2.4). The stages and laser firing are controlled together by the A3200 controller, which itself is computer controlled. SCA software (Workshop of Photonics) was used for designing the laser writing paths (Fig.2.5) and generating the code for the stage motion and firing commands. During writing, when executing this preset code, the A3200 precisely synchronises the laser pulse firing with the $x$ $y$ $z$ stages' positions to ensure consistent writing. The overhead camera and LED lighting allow in-situ visualisation of the writing process and inspection of the imprinted structure quality.

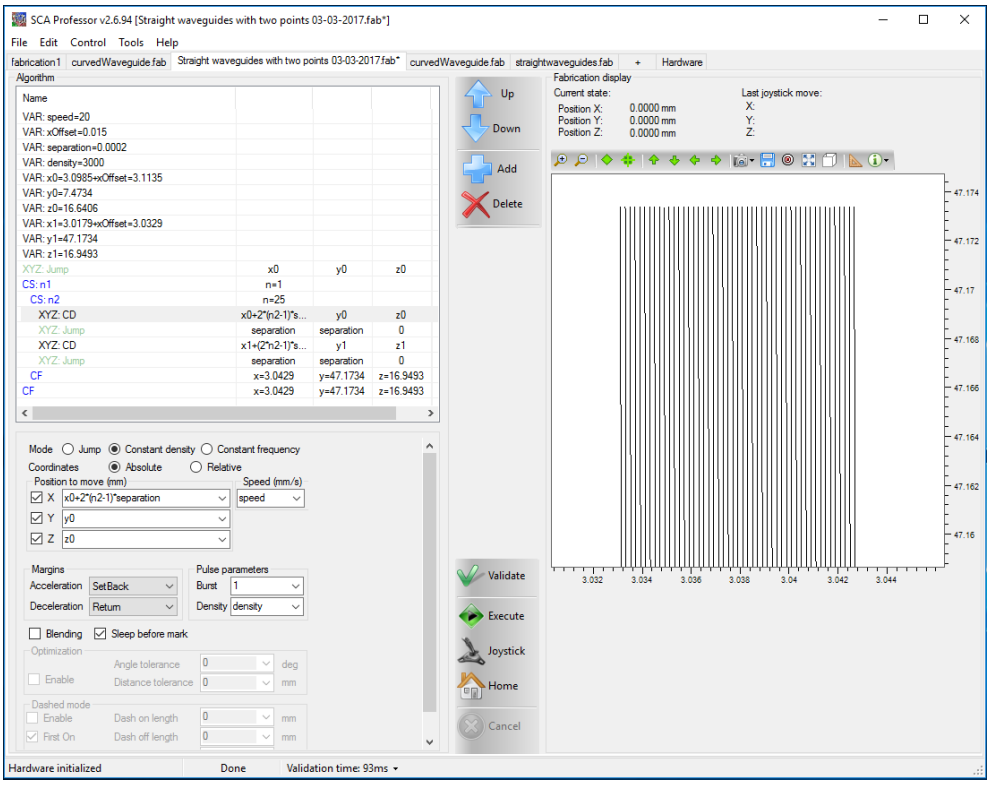


FIGURE 2.5: Screenshot of SCA software used to design fabrication sketches comprised of scanline patterns, and control the stages and laser accordingly via the A3200.

## 2.2 Waveguide Characterisation Setup

The waveguide characterisation procedure aims to measure the mode output profile and loss. As shown in Fig. 2.6, we launch the light from a laser diode (LD) into a fibre which is butt-coupled to the waveguide facet. Then the output beam is focused by a 0.6 NA objective lens onto a power meter or IR camera for characterising the waveguide loss and mode profile, respectively. The overhead microscope and adjustable lighting allow the waveguides to be visualized, facilitating alignment. The fibre, sample and objective lens are all mounted on translation stages for precise alignment.

## 2.3 Diffractive Elements Characterisation

### 2.3.1 Fresnel Lens Characterisation Setup

For the Fresnel lenses, the focal efficiency and imaging properties such as focal distance, dispersion, focal spot size and resolution are the key characteristics to evaluate. To characterise the focal properties of our FZPs, an RGB LED source which

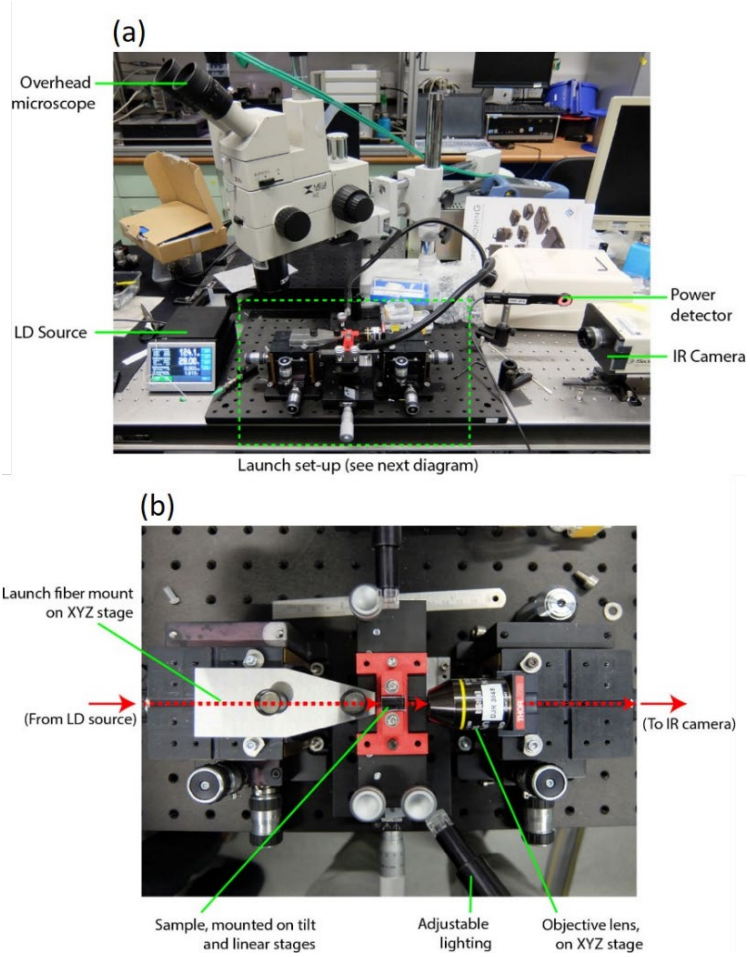


FIGURE 2.6: (a) Characterisation setup for waveguides. Overhead microscope is used for waveguide alignment, power detector for loss measurement and IR camera for mode field detection. (b) Close-up of launch setup section.

can emit three different wavelengths at 458 nm, 528 nm, 629 nm is exploited. Figure 2.7 shows the spectra of the source.

Fig. 2.8 shows the characterisation setup for the FZP focal measurement. The distance between the LED and FZP (20 cm) is much larger than the size of FZP (1.45 mm), so the light incident on the FZP could be considered as a collimated beam. The FZP substrate is fixed on a 3D printed holder (Fig. 2.9(a)) and focuses the light to the camera sensor (Fig. 2.9(b)). The sensor with a resolution of 640×480 was disassembled from a Microsoft LifeCam HD-3000 Webcam and attached to a motorized 3-axis stage (NanoMax 300 from Thorlabs) whose position can be precisely controlled by a PC. The distance between the camera sensor and FZP was around 10 mm. The transverse intensity profile near the focus of the FZP has been characterised at different longitudinal positions. By repeating the experiment with different wavelengths, we were able to compare the focal differences of the LED wavelengths with simulation results.

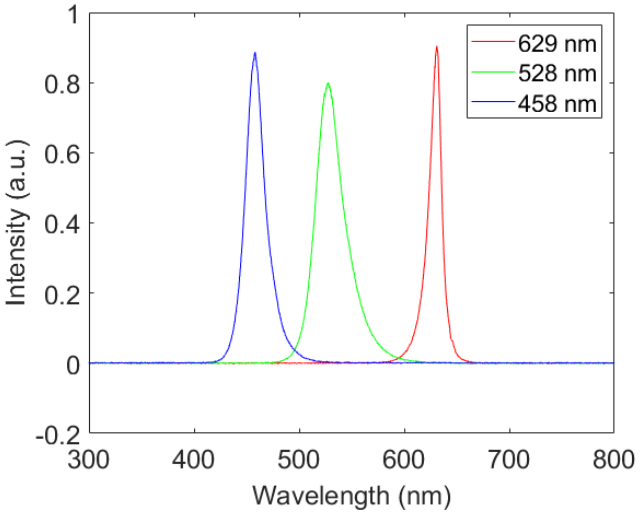


FIGURE 2.7: Spectrum of 3-color RGB LED source for Fresnel lens characterisation. The output peak wavelengths are 629 nm, 528 nm and 458 nm.

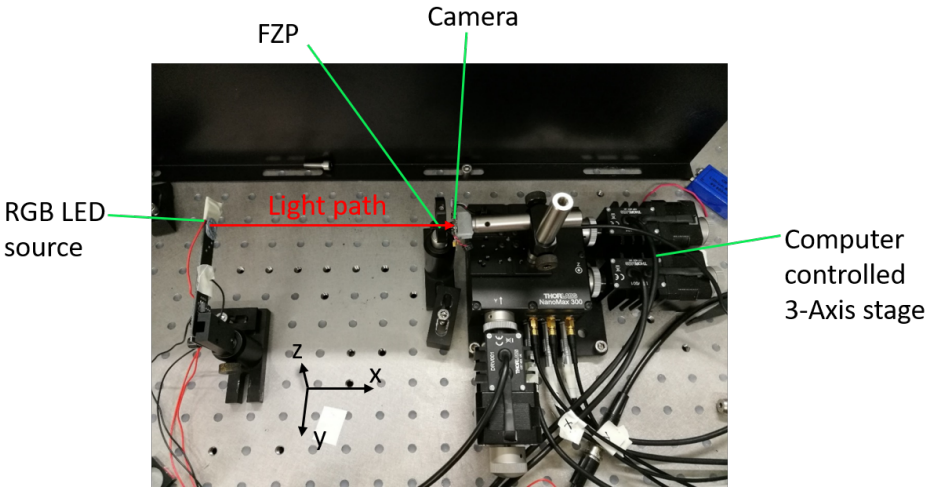


FIGURE 2.8: Setup for characterising FZP focal properties.

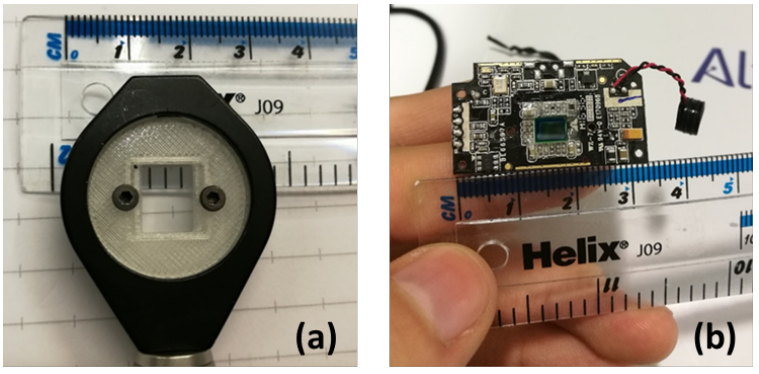


FIGURE 2.9: (a) 3D printed holder for mounting FZP and (b) a web camera module with imaging sensor for FZP focal detection.

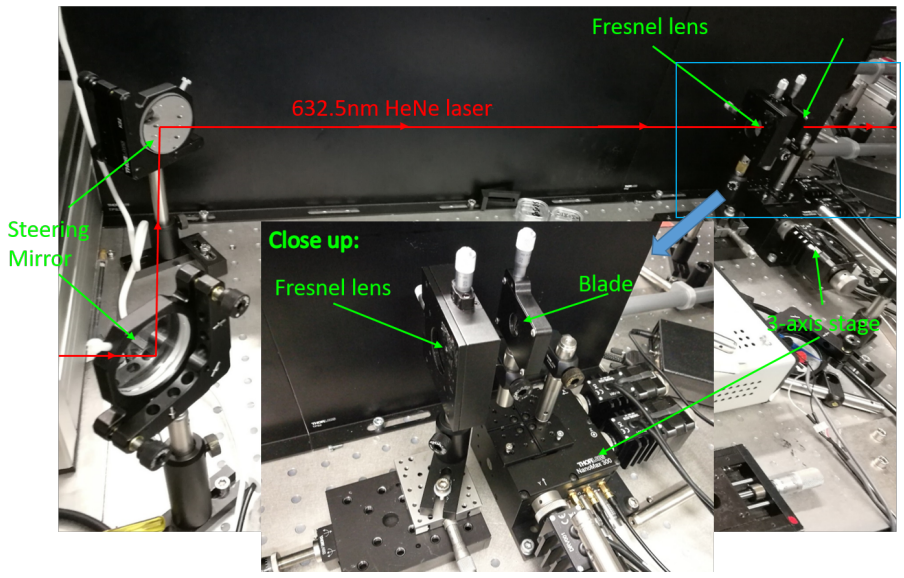


FIGURE 2.10: Characterisation setup for knife-edge profiling and determination of FZP focal efficiency.

In order analyse the focal intensity profile precisely and estimate the focal efficiency, knife edge technique measurements were employed. Figure 2.10 shows the characterisation setup for the Fresnel lens. The path of the HeNe laser beam can be adjusted by two steering mirrors. It then goes through the Fresnel lens which is fixed on the $x$-$y$ stage. The blade shown in the close-up is fixed on the 3-axis stage which can be controlled by a PC through MATLAB.

By moving the blade stage perpendicularly to the laser beam, the transmitted power after the blade can be measured with a power meter. This provides information on the power distribution of the focused beam which can then be translated to the focal beam property and used for estimating the efficiency of Fresnel lens.

Next, Figure 2.11 shows the setup for efficiency characterisation. The HeNe laser output is focused by the Fresnel lens and then collected by an objective with NA=0.25. The collimated beam is then measured by a power meter. The iris is used for selecting only the power from the central focused spot. The Fresnel lens is fixed on a tunable stage to enable precise movement.

For the imaging property characterisation part, experimental setup shown in Fig. 2.12, a calibration slide is used for imaging. For a more precise measurement, we exploited a computer controlled 3-axis stage which has travel lengths up to 4 mm in the $x$, $y$ and $z$ directions controlled using MATLAB with a resolution up to 5 nm.

To further investigate the imaging resolution and field of view, we fabricated different straight-line arrays with different widths using our femtosecond laser (shown in Fig. 2.13).

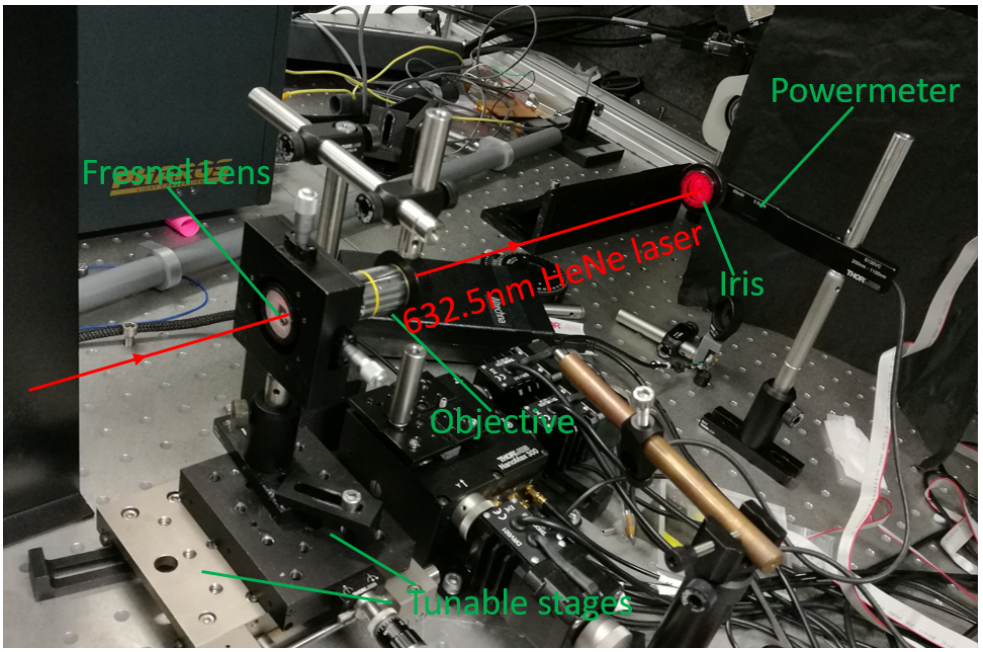


FIGURE 2.11: Focal efficiency characterisation setup for Fresnel lens.

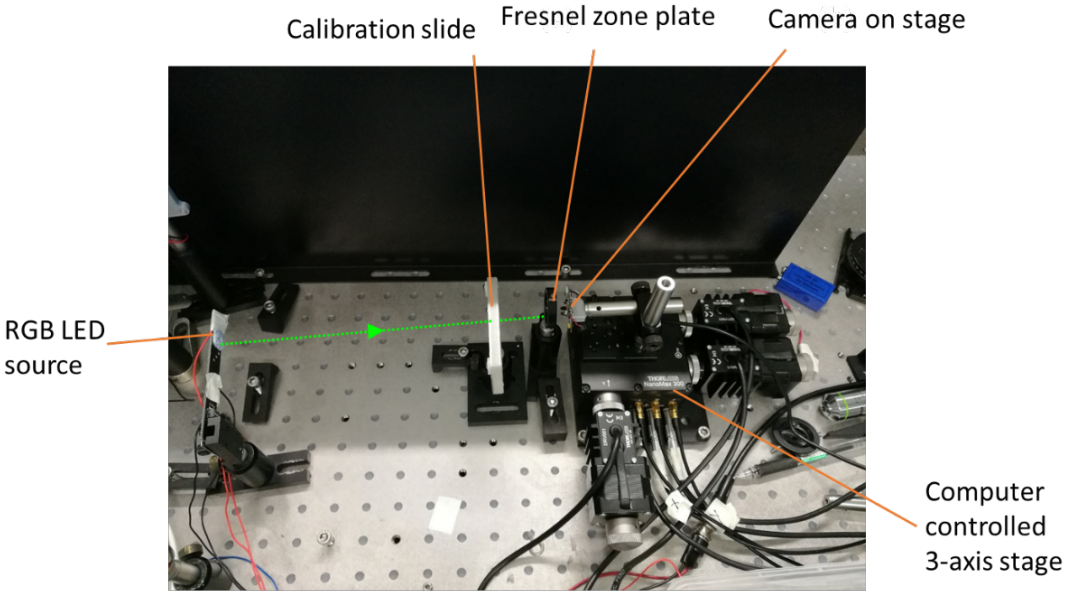


FIGURE 2.12: Experiment setup for calibration slide imaging.

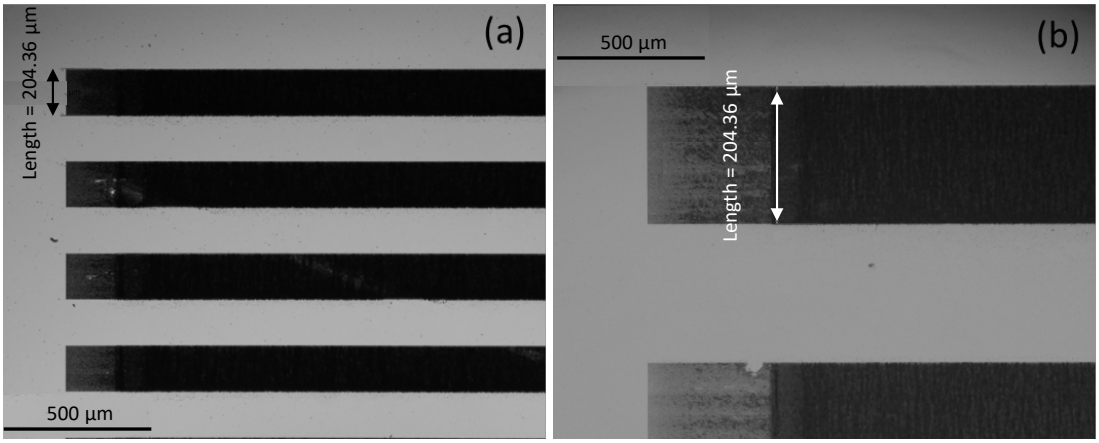


FIGURE 2.13: Microscope images of the fabricated patterns: (a) Array line with 200 $\mu$m and (b) 600 $\mu$m width and gap.

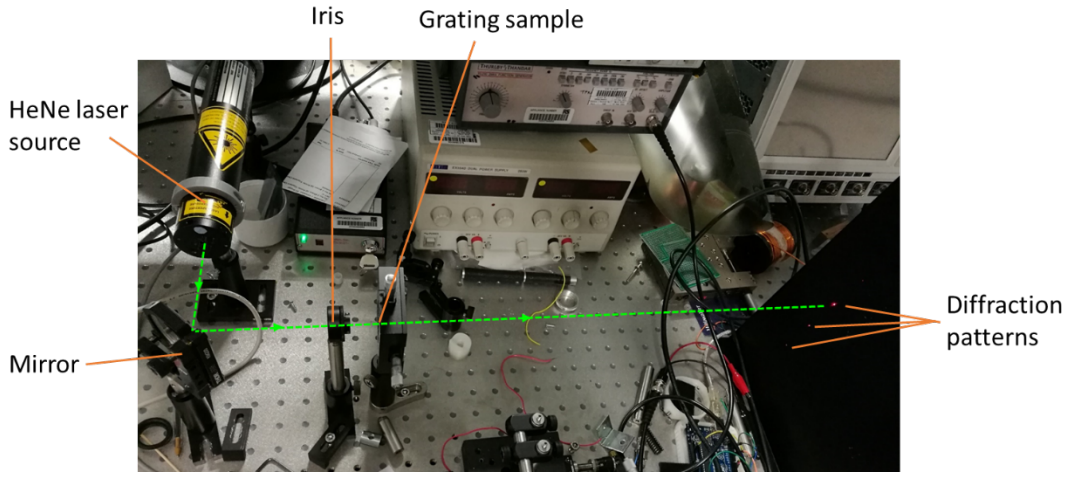


FIGURE 2.14: Characterisation setup for measuring grating diffraction efficiency.

### 2.3.2 Diffractive Grating Characterisation Setup

For the diffractive grating, the diffraction efficiency is characterised. Figure 2.14 shows the experimental setup, a 632.8nm wavelength beam from a HeNe laser passes through an iris, which is used to modify the beam size, then incidents onto the grating sample and creates diffraction patterns. The grating sample is fixed on a holder which can move in transverse directions. By comparing the power of the first diffraction order beam and reference beam (which passes through the sample without incident on the grating) going through the grating, the diffraction efficiency can be estimated. Also, with a polariser, grating diffraction efficiency with two orthogonal linear polarisation states beam input are measured.

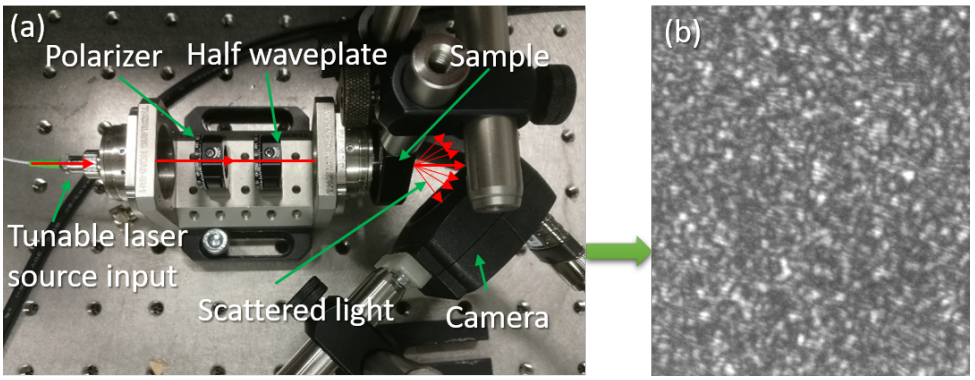


FIGURE 2.15: (a) Setup for characterising scattering sample speckle patterns. (b) Example speckle pattern captured with camera.

## 2.4 Scattering Media Based Devices Characterisation

### 2.4.1 Spectrometer Characterisation Setup

To evaluate the performance of the scattering chip as a spectrometer, it is first necessary to capture the speckle intensity pattern images generated by inputting different wavelengths. This characterisation was performed with a 1040 – 1160 nm tunable laser source (TLS) with ∼30 pm linewidth and optical signal-to-noise ratio of 60 dB. The tuning step of the laser is set to 0.1 nm (Fig. 2.15). The TLS output is launched into a fibre bench with a linear polarizer and a half-waveplate to maintain a fixed angle linear polarisation state. After light passes through the scattering medium, the resulting speckle pattern (see Fig 2.15(b)) is collected by a monochrome CMOS camera with enhanced near-infrared sensitivity (UI-3240LE-NIR-GL, IDS). During calibration, by tuning the TLS wavelength from 1110 to 1115 nm in 0.1 nm steps, we capture the speckle patterns corresponding to each wavelength. This calibration group of speckle patterns can then be used for reconstructing the spectrum of an unknown speckle pattern.

### 2.4.2 Interferometric Surface Topography Setup

The scattering chip was also used as a surface height topography profiler, by integrating it with a Michelson interferometer. Broadband light is back-reflected from a surface to create an interference spectrum by the interferometer, which passes through the scattering chip. Different surface heights generate different interference spectra and hence different speckle patterns. The experimental setup in Fig. 2.16 is used to calibrate the scattering chip's speckle patterns to different surface heights, and to evaluate the operating range and resolution. The apparatus comprises three main parts, all linked with a single-mode fibre (Nufern 780HP): the light source, a remote probe and the scattering chip detection assembly. In this implementation (Fig. 2.16)

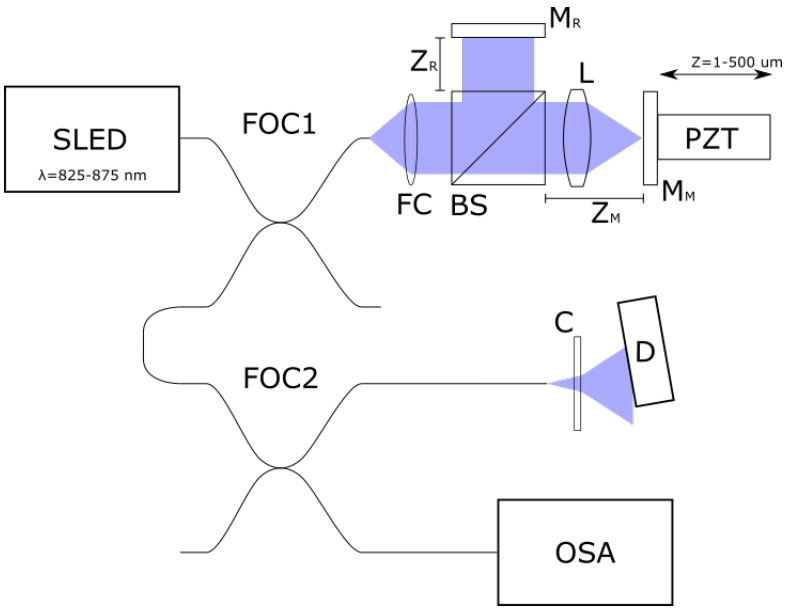


FIGURE 2.16: Optical layout of the scattering chip interferometer. SLED - superluminescent diode; FOC1 and FOC2 - 50:50 fibre optic couplers; FC - GRIN fibre collimator; BS - beam splitter; L - doublet lens; $M_M$ - calibration mirror; $M_R$ - reference mirror; PZT - piezo-electric translator; C - scattering chip; D - CMOS detector; OSA - optical spectrum analyzer.

we use a Michelson probe for surface topography measurement, constructed from off-the-shelf cage system components. This may be replaced by any miniature interferometric probe optimised for distance, topography, strain, temperature or pressure measurement as necessary.

Light from a broadband ($\lambda_c$=850 nm, $\delta\lambda$=50 nm) superluminescent diode (SLED) is coupled into a single-mode fibre before being split by a 50:50 fibre optic coupler (FOC1). The light from one arm of FOC1 arrives at the Michelson probe and is coupled into free-space by a GRIN fibre collimator (FC) before being split into the reference and measurement arms of the probe by a beam splitter (BS). In the probe reference arm light is reflected from the reference mirror, $M_R$, with the phase advancing by an amount $2kZ_R$. Meanwhile in the measurement arm a doublet lens (L) focuses the measurement beam onto the calibration mirror ($M_M$) mounted upon a piezo-electric translator (PZT) before it passes back through to recombine with the reference beam at the beam splitter with the phase in the measurement arm having advanced by $2k(Z_M + d)$ where $d$ is the change in measurement path length incurred by changing the PZT position. Following recombination of the two beams at the beamsplitter the light is recoupled back into the fibre.

The recoupled measurement and reference beams next travel a common-mode path back through FOC1 before being split by FOC2. One arm of the coupler leads to an optical spectrum analyser (Thor Labs OSA201C) which is included only as a tool for alignment of the probe and to provide spectral interferograms for comparison. Light

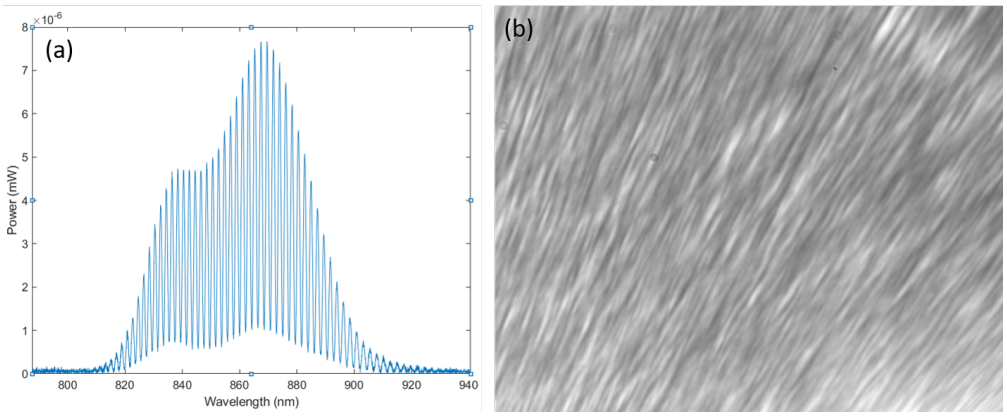


FIGURE 2.17: (a) A typical spectral interferogram, as captured from a ThorLabs OSA and (b) a white light speckle pattern exhibiting directional blurring of speckles noticeable when compared to a monochromatic speckle pattern (e.g. Fig. 2.15(b)).

exiting the second arm of FOC2 is incident upon the glass slide housing the speckle chip. A CMOS camera D (Pixel Link D721MU-T) captures the scattered light and speckle patterns are saved to the computer for post-processing.

The wavenumber ($k$) dependent phase of light arriving at the OSA is thus:

$$\theta(k) = 2kZ_R - 2k(Z_M + d) \tag{2.3}$$

where $d$ is the change in length of the measurement arm due to movement of the PZT or a measurement sample and, $Z_M$ and $Z_R$ are the measurement and reference arm path lengths respectively. The resulting spectral interferogram observed at the OSA can thus be described as follows:

$$I(k) = B\{k\} + A\{k\}cos(\theta\{k\}) \tag{2.4}$$

where $B\{k\}$ is the contribution of non-interfering DC light and $A\{k\}$ is the power spectral density of the light source, in this case a double-Gaussian. An example spectral interferogram from the OSA is shown in Fig. 2.17 (a) next to a speckle pattern from the scattering chip in Fig. 2.17(b) for the same measurement path length.

## 2.5 Conclusions

In this chapter, the laser writing setup, inscription parameters and characterisation setups for later applications were explained part by part. For inscription, we use either a 1030 nm wavelength femtosecond laser beam or its second harmonic at 515 nm focused onto a sample. The inscription region can be scanned in 3D using the $x$-$y$ and $z$ translation stages, which are computer controlled via a stage-controller with the help

of fabrication design software to compose the scanline paths. Depending on the requirement of the application, not all the components in the laser setup are used for the work described in the later chapters. In particular, for inscribing waveguides and scattering points, we simply focus the writing beam using an objective into the substrate, whereas to fabricate diffractive elements, we may also introduce an axicon to generate a Bessel beam. This allows us to optimise the beam focus profile according to the geometry under fabrication.

# Chapter 3

# Laser Written Waveguides

In this chapter, we aim to find the effects of different laser parameters on the resulting glass material modification properties by performing tests to inscribe straight waveguides under different settings. For waveguide evaluation, the mode field diameter (MFD) will been presented. This work was done with Timothy Lee and is also one part of a company project. This offers useful insight as knowledge of the MFD allows us to estimate the laser induced refractive index change, which must be first assessed before we are able to design and fabricate diffractive elements (in a later chapter). Furthermore, based on the waveguide writing method, a stress control technique for fs laser written structures will be discussed. Aside from helping us to evaluate the induced index change, the waveguide structures themselves have numerous applications, which we demonstrate by presenting a waveguide assisted multicore fibre directional sensor.

## 3.1 Characterization of Index Change

### 3.1.1 Waveguide Writing Method

As a fundamental structure and building block for more complex devices, a waveguide has a relatively simple geometry which is advantageous as a tool for fabrication parameter testing. By measuring the waveguide properties like loss and output mode profile, we can easily study the influence of (and optimise) fabrication parameters.

For fs laser writing, the regions of the sample where we wish to induce an index change are normally inscribed using a line-by-line scanning method (multiscan) Nasu et al. (2005), in which multiple lines are written closely together to form a wider structure with quasi-uniform refractive index distribution (Fig. 3.1). The blue dashed

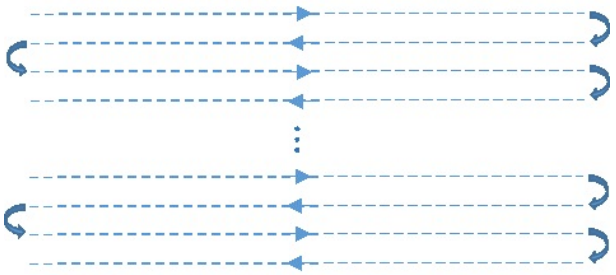

FIGURE 3.1: Schematic of multiscan laser writing method. Typical line spacing is $s = 200$ nm.

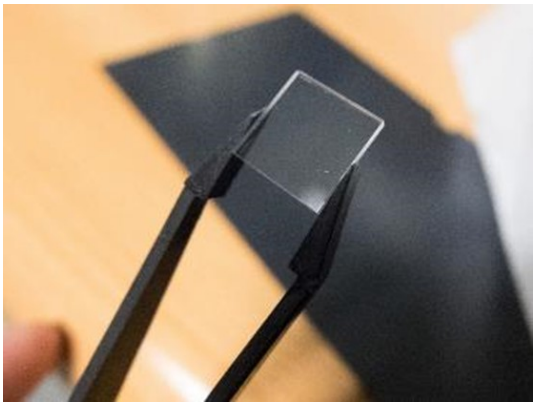

FIGURE 3.2: Fused silica substrate with $10 \times 10 \times 1$ mm size.

line shows the laser writing direction. It is worth noting that the separation $s$ between each scan line determines the pulse density perpendicular to the scan direction, which is also an important parameter for laser writing.

In the previous chapter, Fig. 2.1 shows the laser writing setup; note for waveguide writing using the 1030 nm beam, the SHG and Bessel beam generation parts are omitted. Our sample is fused silica substrate manufactured from commercial glass 'Spectrosil 2000' by Heraeus, which is high purity, homogeneous, free of bubbles and inclusions, and low loss over wavelengths 180∼2000 nm (see Fig. 3.2).

### 3.1.2 Parameter Testing

In this section, we will use the laser written waveguides to show how the laser parameters affect the written structures. Fig. 3.3 shows the transmission microscope images of several waveguide cross-sections. The four sets of the waveguides are written with a fixed density $D$=5000 pulses/mm and $k_B$=1, $s$=200 nm, $v$=10 mm/s. The waveguides are written at a 0.5 mm depth below the substrate surface. They all have the same widths of 10 $\mu$m and lengths of 10 mm. In Fig. 3.3, we found with a higher writing power (35 mW to 55 mW), the cross-section micrographs of waveguides become brighter which indicates a stronger light confinement and higher

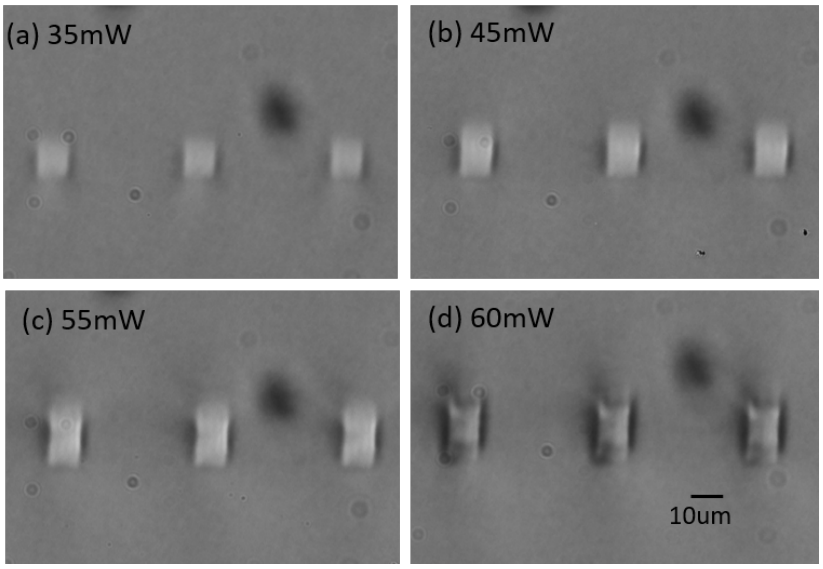


FIGURE 3.3: Microscope images ($\times$50) of waveguide cross-sections with writing powers of (a) $P_w$ = 35 mW, (b) 45 mW, (c) 55 mW and (d) 60 mW. Other parameters: 0.4NA objective, $D = 5000$ pulses/mm, $k_B = 1$, $s = 200$ nm and $v = 10$ mm/s.

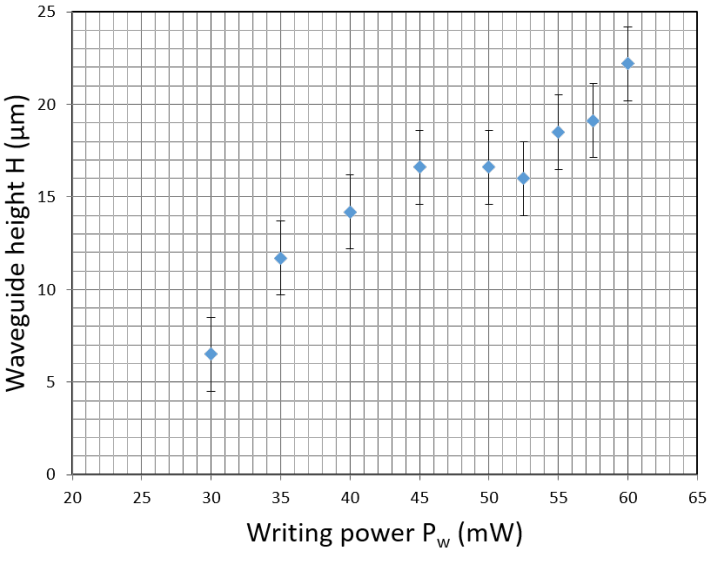


FIGURE 3.4: Height of waveguide vs laser writing power. Other parameters are: $D = 5000$ pulses/mm, $k_B = 1$, $s = 200$ nm and $v = 10$ mm/s.

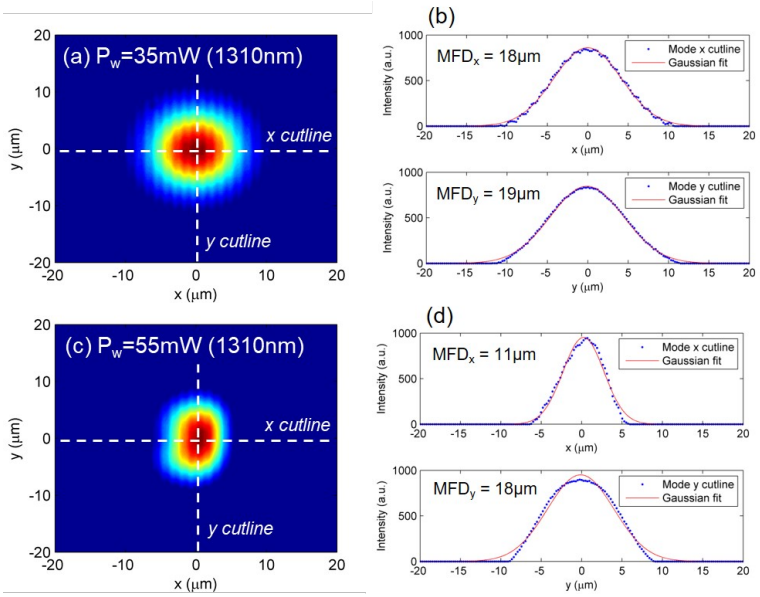


FIGURE 3.5: Fundamental mode intensity profile and cutlines with MFD measurement in waveguides inscribed with writing powers of (a-b) $P_w$=35 mW and (c-d) $P_w$=55 mW.

refractive index difference between the waveguide core and surrounding material. Fig. 3.4 plots waveguide height against writing power. With higher writing power, the waveguide height is increased, which is caused by the greater intensity at the laser focal area. However, for the power of 60 mW, the cross-section of waveguides becomes dark which indicates poor guidance of light. This could come from laser induced damage by the cumulative stress, of which a detailed discussion will be presented in section 3.2. By tuning the laser parameters, the best waveguide loss we got is 0.1 dB/cm.

### 3.1.3 Characterisation

For a better quantification of the waveguide profile, the MFDs were measured with the setup in Fig. 2.6. Figure 3.5(a) and Figure 3.5(c) show the mode profiles of our waveguides inscribed with writing powers of 35 mW and 55 mW. We then fitted a Gaussian curve to the mode cutline in the $x$ and $y$ directions and calculated the mode field diameters in MATLAB (Figs. 3.5(b) and Fig. 3.5(d)).

Repeating these measurements at 1310 nm and 1550 nm, for waveguides written at different powers, we obtain the following trends in Fig. 3.6. The decreasing MFD with increasing power indicates tighter guidance of light and thus higher induced index change. With increased writing power, the MFD decreased in the $x$ direction for both wavelengths, which means higher power induces higher index change. However, in the $y$ direction, MFD is affected by both waveguide height and $\Delta n$, so it has the lowest value at $P_w$ = 45 mW.

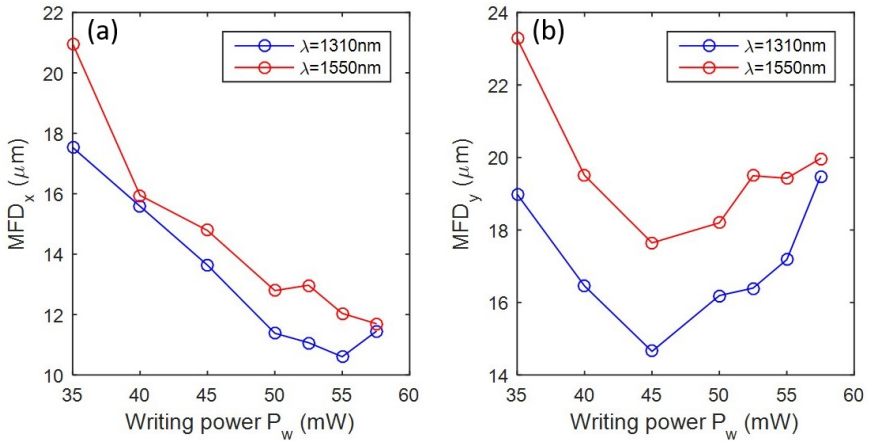


FIGURE 3.6: Mode field diameter in $x$ and $y$ directions with 1310 nm and 1550 nm laser sources vs laser writing power.

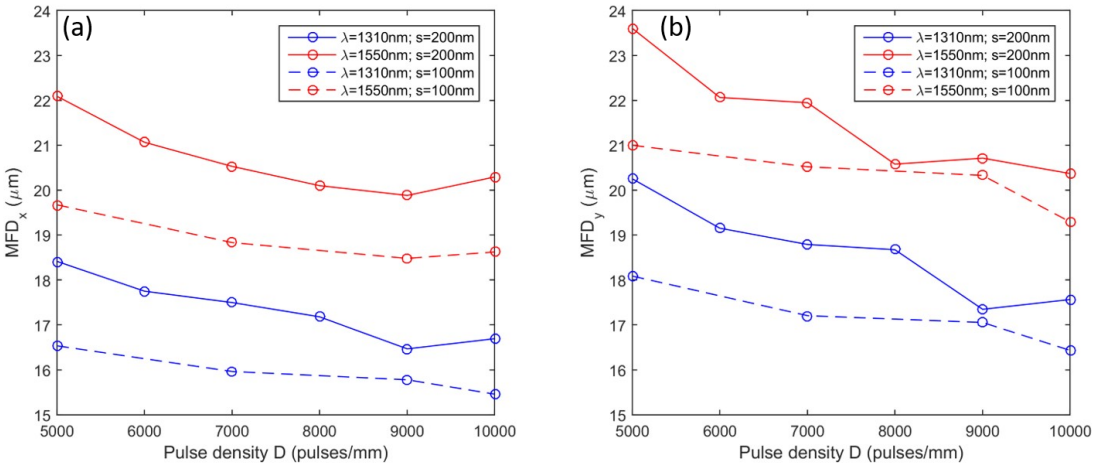


FIGURE 3.7: Mode field diameter in $x$ and $y$ directions with 1310 nm and 1550 nm laser sources vs laser writing density and scan separation.

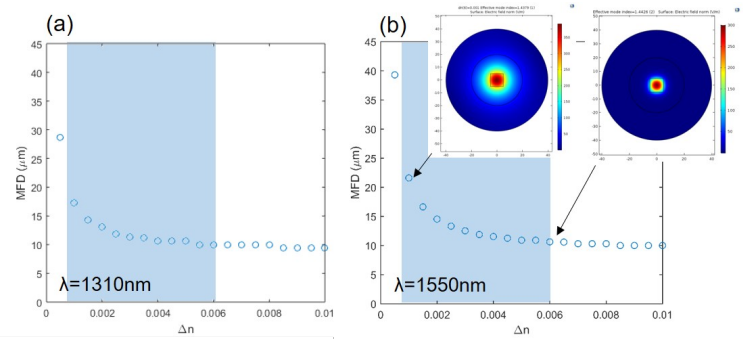


FIGURE 3.8: Simulated MFD vs $\Delta n$ for (a) $\lambda$=1310 nm and (b) 1550 nm, for a $10 \times 10$ $\mu$m silica waveguide (MFD$_x$=MFD$_y$). Shaded region corresponds to range of experimentally observed MFDs from test waveguides.

For different pulse density $D$ and line separation $s$, Fig. 3.7 shows the results. With the density increased, the MFD for the $y$ direction has a decreasing trend as expected. However, for a density of 9000 pulses/mm, in the $x$ direction the MFD reaches a lowest level, implying that $\Delta n$ has reached a maximum and plateaued.

While for inscribing waveguides, we are able to quantify the laser parameters' influence on MFD, for other more complex structures such as gratings and Fresnel lenses, MFD is not a relevant parameter but $\Delta n$ is the key parameter. Therefore to estimate $\Delta n$ based on these MFD measurements, we simulated the MFD in COMSOL with different refractive index changes, and compared them against the experimental MFDs.

Fig. 3.8 shows the simulated MFD for a $10\times$ 10 $\mu$m waveguide cross-section. Comparison with measured MFD, it suggests that the experimentally induced $\Delta$n ranges between $7\times10^{-4}$ to $6\times10^{-3}$ (see shaded region) for $P_w$=35 mW to 55 mW. We will use the estimated $\Delta n$ as a reference to design the diffractive Fresnel lens in a later chapter.

## 3.2 Stress Distribution Analysis

While optimising the waveguide, we found that not only the writing parameters but also the laser writing method can affect the waveguide structure. More specifically, the material is traditionally modified by scanning the writing beam in a raster line pattern known as 'multiscan' Nasu et al. (2005), which leads to an asymmetric stress distribution and even crack formation, for example under higher powers. However, by applying different scanning techniques, we are able to control the refractive index and stress profile to minimise the negative impacts of stress (such as cracks and damage). This section will demonstrate the refractive index distribution formed under different writing methods and investigate a new approach for controlling the laser induced stress distribution.

### 3.2.1 Methods

The experiments were carried out with the setup in Fig. 2.1. We used the second harmonic beam instead of the pump beam because the shorter 515 nm writing wavelength can be exploited to achieve a higher index change Shah et al. (2005). An axicon with a 179° apex angle was then used to generate the Bessel beam, which creates a writing beam capable of modifying a much larger height than a focused Gaussian beam. A 0.4 NA objective was used to focus the beam in order to reduce its axial Bessel zone length (over which it is non-diffractive) and hence control the height

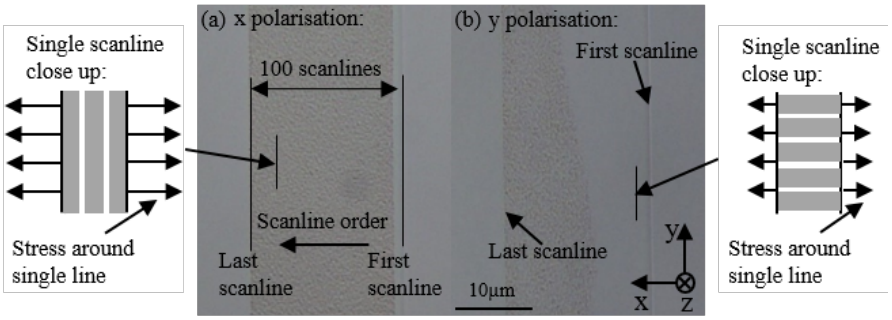


FIGURE 3.9: Top view of Bessel beam written waveguide with laser linearly polarised (a) perpendicular to waveguide direction ($x$ direction) and (b) along waveguide direction ($y$ direction). Single scanline close up schematics indicate the direction of nano grating and stress around scanline Champion et al. (2013). The shadow zones are the nano-gratings inside a single scanline. $x$ polarization laser writing gives higher level of the stress around the scanline than the $y$ polarization.

of the inscribed structure, as well as improve resolution by reducing the beam width. The fused silica substrates (UVFS C7980 0F) used in our experiments were manufactured by Corning Ltd.

Initially, we investigated stress distribution around laser written high-aspect-ratio waveguide-like structures. Each waveguide was written with the stage moving in the $x$ and $y$ directions, to inscribe 100 closely spaced raster scanlines. Each scanning line is written within the 10 mm sample in the $y$ direction with a typical scanning line separation of 200 nm in the $x$ direction. The edges of the substrate were polished before laser writing to reduce surface scattering. The buried waveguides were written 0.5 mm below the sample surface. A typical pulse energy for Bessel beam writing is approximately 0.5 $\mu$J and pulse density is $10^5$ pulses/mm along each scanning line.

The $\Delta n$ of the structure induced by femtosecond laser depends on the laser parameters (pulse density, pulse energy) within the continuous modification region. Beyond the material damage threshold, we found different damage (nanograting) formation behaviours for the two orthogonal linear polarisation states of the writing beam (see Fig. 3.9). This is caused by the different stress distribution around laser writing lines. For a $y$ polarised laser beam, the generated nanograting planes are perpendicular to the $y$ direction (Fig. 3.9(b)) and thus has lower stress distributed around a single line than the $x$ polarised beam Champion et al. (2013) (Fig. 3.9(a)). In order to eliminate the polarisation-dependant damage formation, we use circular polarisation for laser writing, which generates a more isotropic stress distribution McMillen and Bellouard (2015).

Stress profiles of the waveguides were obtained via retardance measurements using an optical microscope system with a VariLC liquid crystal device controlled by OpenPolScope software. For further investigation on diffractive optics, we wrote diffractive 50/50 gratings and Fresnel lenses. A detailed explanation of these

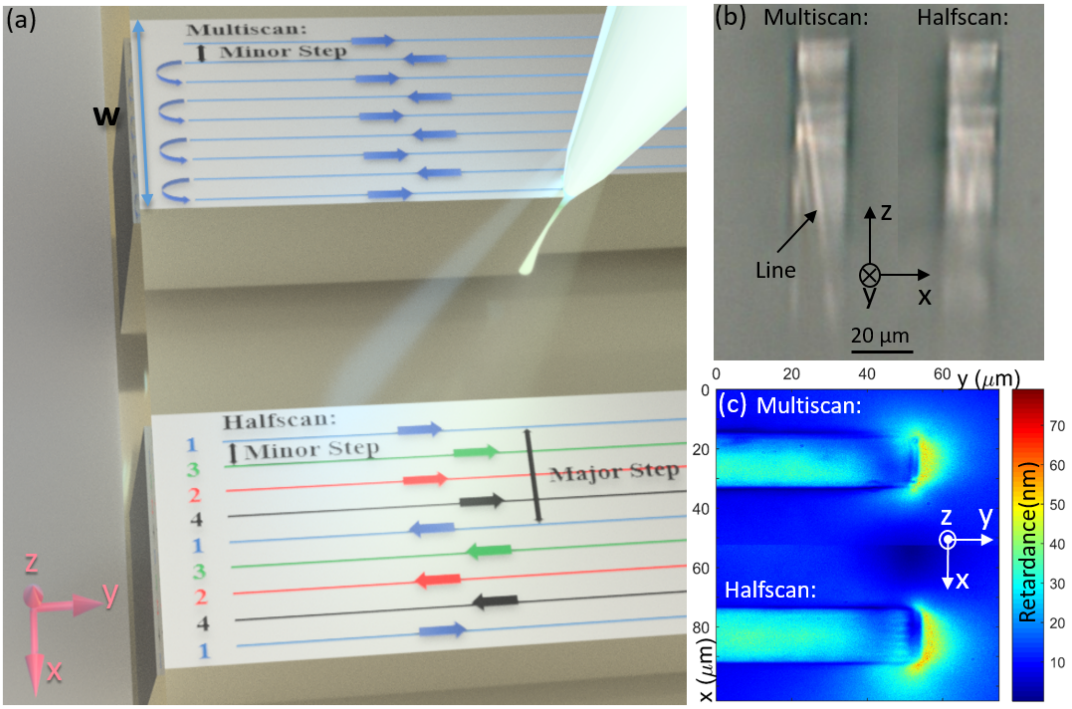


FIGURE 3.10: (a) Schematic of multiscan (top) and halfscan (bottom) laser writing methods. Arrows show laser moving direction. For halfscan, colours denote different writing order (blue-red-green-black). (b) Microscope image of Bessel beam written waveguide cross sections with multiscan (left) and halfscan (right) methods. Both waveguides have a minor step of 0.2 $\mu$m and the halfscanned waveguide has a major step of 1.6 $\mu$m. Both waveguides have widths (in $x$ direction) of 20 $\mu$m and are written with a laser pulse energy of 0.65 $\mu$J and pulse density of $10^5$ pulses/mm. (c) Top view (-$z$ direction) retardance measurement of waveguides in (b).

diffractive elements is shown in Chapter 5. The grating has a 10 $\mu$m period and $1 \times 1$ mm size, while the Fresnel lens has a 2 mm diameter and 10 mm focal length. Both the gratings' first order diffraction efficiencies and Fresnel lenses' focal efficiencies were characterised with a 632.5 nm wavelength HeNe laser.

### 3.2.2 Results

Fig. 3.10(a) compares the schematic of femtosecond laser written waveguides with multiscan (laser scanlines are written one next to the other with a minor step) and halfscan (laser scanlines are rearranged so that the later scanline has a larger step next to previous one) writing methods. The width $w$ (in the $x$ direction) of each waveguide is 20 $\mu$m. For the multiscan method, the laser scanlines are written consecutively one next to the other with a minor step of 200 nm in the $x$ direction. As a result, each scanline will be affected by the stress distribution of the previous line, which results in the stress accumulation. The left side of the microscope image in Fig. 3.10(b) shows a traditionally written (i.e. multiscanned) waveguide cross section. The brighter area

shows the higher laser induced index change and thus stronger guidance of microscope illumination light. The uneven index distribution in the $z$ direction is a result of uneven axial intensity distribution of Bessel beam itself McGloin and Dholakia (2005). Due to stress accumulation, the multiscanned waveguide forms a gradient index change which results in a visible index cross line. This line forms and can be easily observed by microscope when the laser pulse energy is high, approximately 0.65 $\mu$J for our Bessel beam writing set up. However, even when the index cross line is not obvious for lower powers, the asymmetric stress distribution still exists with the conventional multiscan technique. These features remain present in the cross section after polishing, which also can introduce large cracks due to the high stress. The inhomogeneous stress distribution produces an uncontrollable index profile thus reducing the efficiency of any diffractive optics based on such structures.

To reduce the stress asymmetry, we use a new 'halfscan' method depicted in the bottom waveguide in Fig. 3.10(a), where the line order is rearranged. Different colours denote the line writing order (blue-red-green-black). The main principle is to keep each scanline separated from the previously written scanline by a major step (8 times larger than the minor step) and finally achieve an overall minor step structure. As the gap between each consecutive scanline is larger than for the multiscan method, this reduces the effect of the previous scanline on the writing of the next line. Also, the larger scan step reduces the chances of damage. The right waveguide in Fig. 3.10 shows the improved profile obtained with 1.6 $\mu$m major step halfscan writing method, compared to the multiscan written waveguide which shows an obvious index contrast line.

In order to investigate how the stress was distributed for each laser scanning method, we then performed top view retardance measurements of the waveguides (Fig. 3.10(c)). Note that for these test waveguides, only one end reaches the sample end face (to allow cross section imaging), and the other end terminates within the silica. Indeed, for our analysis we focus on the portion away from the extremities, since the anisotropy around the ends is not representative of the rest of the structure. The halfscanned waveguide shows a more even retardance profile across the waveguide's width in the $x$ direction compared to the multiscanned waveguide. The retardance distribution is related to the stress profile of the structure, which will be analysed in the discussion section.

To demonstrate that this technique can be applied to more complex multilayer structures, we wrote 50/50 diffractive gratings (which has equal width modified and unmodified zones in one grating period) and 2-layer Fresnel lenses. Fig. 3.11 shows the microscope image of a two layer Fresnel lens cross section region near the centre (the dotted line shows the Fresnel lens central axis). The Fresnel zones with increased refractive index are clearly visible, and decrease in width with radial distance (in the $-x$ direction) from the centre. The Fresnel lens was written with a Bessel beam using

TABLE 3.1: Efficiency of diffractive optical elements inscribed with different writing methods.

| | 50/50 Grating | 2-layer Fresnel Lens |
|---|---|---|
| Multiscan | 17.7% | - |
| Halfscan | 24.1% | 55% |

the halfscan technique at a power of 90 mW. The thickness of each layer (in $z$ the direction) is 100 $\mu$m. Some of the laser affected Fresnel zones are marked in the image. Notice that the laser affected zone appears quite smooth compared to the left multiscanned waveguide in Fig. 3.10(b). Table 3.1 shows the diffractive efficiency results at a measurement wavelength of 633 nm. The efficiency of the 50/50 grating is the first order diffraction efficiency tested with the HeNe laser with 632 nm wavelength. For the halfscanned grating, the first order diffraction efficiency of grating improved by 36% (from $\eta$ = 17.7% to 24.1%) compared to the multiscan method. With the halfscan method writing, the Fresnel lens reached a focal efficiency of 55%, with a theoretical limit of 65%.

The observed benefits are not limited to Bessel beam writing, as we also achieved a more symmetric structure with the halfscan technique whilst writing low-aspect-ratio waveguides (10×10 $\mu$m cross section) with a Gaussian beam. The pulse energy was 0.3 $\mu$J and pulse density $5 \times 10^3$ pulses/mm, using 50 scan lines per waveguide. Fig. 3.12(a) and Fig. 3.12(b) show the output modes from waveguides inscribed using multiscan and halfscan methods, respectively. The mode profile was captured by an IR camera (MicronViewer 7290A, Electrophysics). These waveguides were written with a 1030 nm Gaussian beam with a pulse energy of approximately 0.3 $\mu$J and pulse density of $5 \times 10^3$ pulses/mm along each scanning line. According to the mode intensity plot comparison in Fig. 3.12(c), the waveguide written with the halfscan method has a more symmetric mode profile than that of the multiscan method.

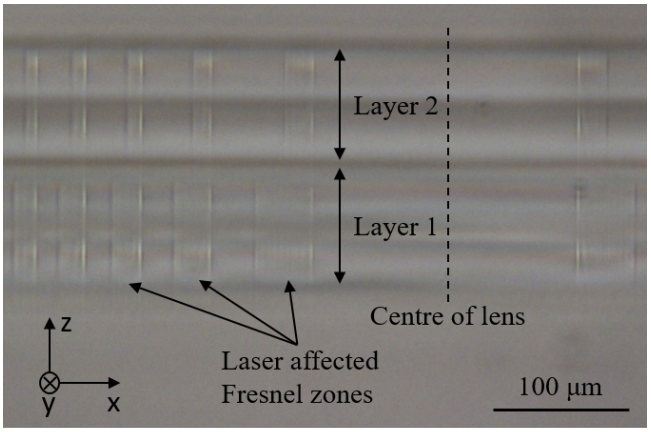


FIGURE 3.11: Cross section of part of a 2-layer Fresnel lens written with a Bessel beam using halfscan technique at power of 90 mW. Diameter of Fresnel lens is 2 mm and thickness of each layer is 100 $\mu$m. Dashed line indicates central axis of lens.

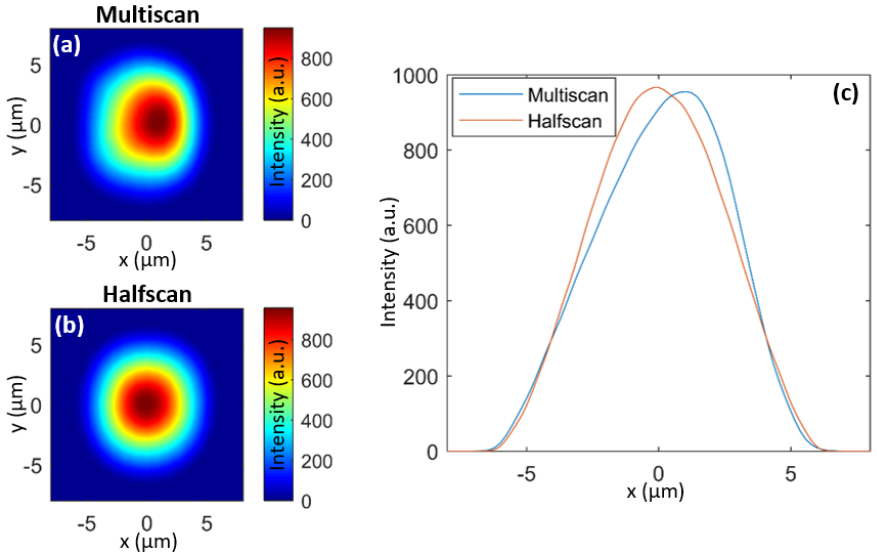


FIGURE 3.12: Mode intensity profile of Gaussian beam written waveguides fabricated by (a) multiscan and (b) halfscan. (c) Central intensity cut-line along $y = 0$. The $x$ axis is centred on the middle of the 10 $\mu$m width waveguide.

### 3.2.3 Discussion

Returning to the structure written with the Bessel beam in Fig. 3.10(c), with the retardance distribution $R$ across waveguide width $w$, we calculated the principle stress difference McMillen and Bellouard (2015) $\Delta\sigma$ by Eq. 3.1 (see right axis in Fig. 3.13(a)):

$$\Delta\sigma = \frac{R}{C \cdot T} \tag{3.1}$$

where $C = 3.55 \times 10^{-12}$ Pa$^{-1}$ is the photoelastic coefficient between two principal stresses in silica, and $T = 100$ $\mu$m is the thickness of waveguide in $z$ direction. Flipping the left side of the waveguide stress distribution curve along $x = 0$ in the Fig. 3.13(a) produces Fig. 3.13(b), which is more convenient for comparing and analysing the symmetry of the waveguide profiles. Fig. 3.14 shows the flipped waveguide stress profiles at 3 laser writing powers (90, 110 and 130 mW, corresponding to pulse energies of 0.45, 0.55 and 0.65 $\mu$J, respectively) for both multiscan and halfscan waveguides.

With both scanning methods, the peak stress level increases with increasing writing power. However, for the 130 mW multiscan written waveguide (Fig. 3.14(c)), the stress maintains the same level with that written at 110 mW. This is due to the stress accumulation in one direction finally forming a nano-crack inside the waveguide at the higher power. These nano-cracks then release part of the stress inside and lower the overall stress level McMillen et al. (2016). For the halfscan writing method, the evenly distributed stress across the waveguide enables a higher tolerance of laser writing power thus higher achieved overall stress level. For different waveguide

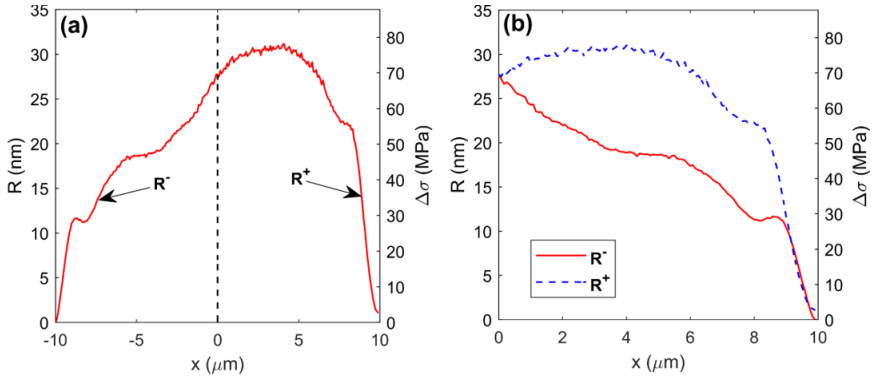


FIGURE 3.13: (a) Retardance $R$ and principle stress difference $\Delta\sigma$ distribution across Bessel beam written waveguides of width $w = 20\mu$m, for multiscan method at laser power of 130 mW. $x$ axis shows the distance to the waveguide centre (half width point). (b) Flipped image of (a) along waveguide centre point (i.e. along $x = 0$ in (a)) where red solid $R^+$ curve and blue dashed $R^-$ curve indicate left and right sides respectively.

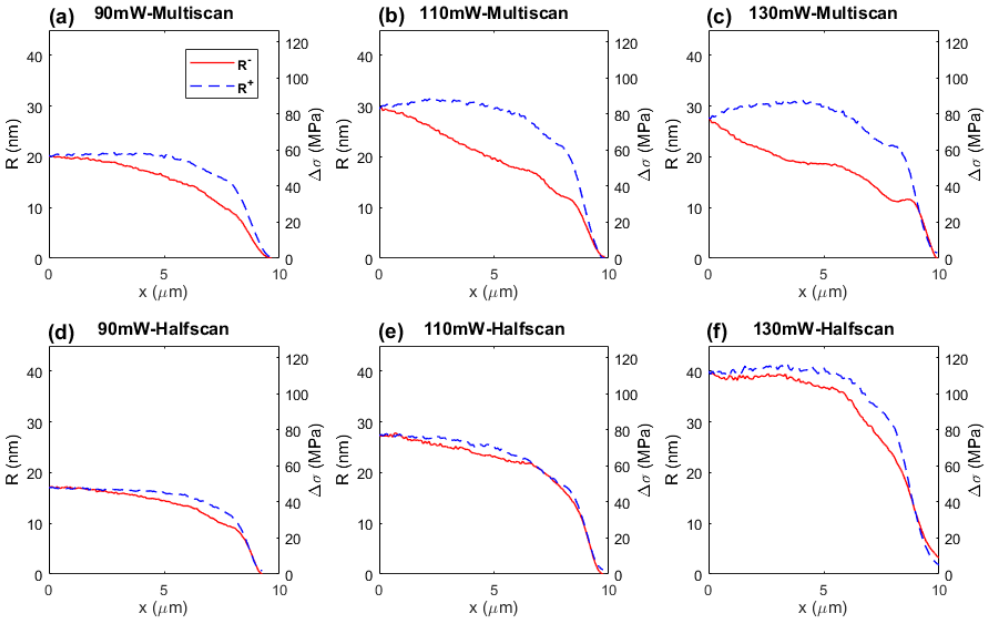


FIGURE 3.14: Flipped stress distributions for Bessel beam written structures, with different power level and scanning method.

widths, further waveguides with a similarly symmetric profile have been written with the halfscan method to confirm that the results are indeed reproducible. For laser written structures, especially DOEs, higher writing power normally leads to higher laser induced index change. With the halfscan method, it is easier to achieve the same phase change in a shorter device depth, which is beneficial for compact device fabrication and saving writing time. For a quantitative comparison, we calculated the average mean square error (AMSE) of the $R^+$ and $R^-$ curves in each figure in Fig. 3.14 with Eqs. 3.2 and 3.3.

$$\overline{R}(x) = \frac{1}{2}(R^+(x) + R^-(x)) \tag{3.2}$$

TABLE 3.2: AMSEs of waveguide stress symmetry.

| | 90 mW | 110 mW | 130 mW |
|---|---|---|---|
| Multiscan | 2.75 $nm^2$ | 14.02 $nm^2$ | 19.85 $nm^2$ |
| Halfscan | 0.48 $nm^2$ | 0.32 $nm^2$ | 2.12 $nm^2$ |

$$AMSE = \frac{1}{w}\int_0^{w/2}[R^+(x) - \overline{R}(x)]^2 + [R^-(x) - \overline{R}(x)]^2 dx \tag{3.3}$$

Table 3.2 shows the AMSE results. The AMSE of multiscanned waveguides rapidly increases from 2.75 $nm^2$ to 19.85 $nm^2$ with increasing writing power from 90 mW to 130 mW, which shows a badly degraded asymmetric stress profile. For the halfscan method, the AMSE maintains a low level (2.12 $nm^2$) even with a high power writing (130 mW).

The maintenance of symmetry and stress uniformity is beneficial for more complex structure fabrication. Indeed, the 50/50 grating shows a 36% efficiency improvement by using halfscan over multiscan. For the Fresnel lens, the efficiency is high and approaches the theoretical maximum limit; the discrepancy being due to the theoretical value assuming an infinitely thin device with ideal step-transitions in profile phase, neither of which can be perfectly realised in practice. Finally, it is worth noting that the performance of the DOEs could be further enhanced by varying the pulse density of the scanlines while writing, so as to provide a continuously varying phase profile (rather than a discrete single or two level phase profile) which allows a higher theoretical efficiency limit. The halfscan method would be especially advantageous in this instance as very precise control of the phase profile is essential, and multiscan writing would introduce too much distortion.

As for the waveguides inscribed with the Gaussian beam, we also calculated the AMSE of their mode intensity profiles to compare the modal symmetry obtained by the multiscan and halfscan approaches. Fig. 3.15 shows the comparison of flipped images of the central mode intensity cut-lines. To eliminate the error from different peak intensities, we normalised the peak intensity to unity. The AMSEs of the halfscanned and multiscanned waveguide mode intensities are $2.5 \times 10^{-4}$ and $7.3 \times 10^{-3}$ respectively. The halfscanned waveguide therefore achieves a much more symmetric mode profile than the multiscanned waveguide (30 times more symmetric in terms of AMSE).

Generally, index symmetry and index uniformity are two distinct properties and their importance (or lack thereof) is application-dependant. As an example, it is worth noting that for some applications like waveguides bends or gradient gratings, an asymmetric index distribution could be in fact preferential. Meanwhile, a straight waveguide might benefit from index profile symmetry, but not necessarily transverse uniformity (both graded and top-hat profiles have their benefits, for example).

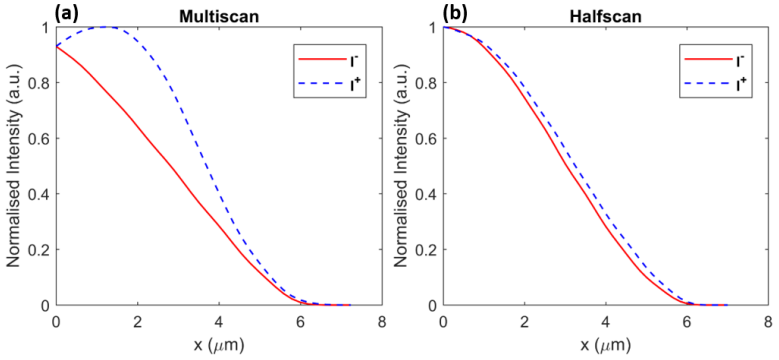


FIGURE 3.15: Flipped normalised mode intensity distributions for waveguides written by (a) multiscan and (b) halfscan.

For different index change based femtosecond laser written applications, we thus propose five different scan methods: multiscan, inward scanning, outward scanning, segmented multiscan, and halfscan. Each method has its advantages and disadvantages. While the multiscan method is the simplest and quickest among all methods, it leads to the strongest asymmetry of the refractive index and stress. The inward scanning method scans from outside edges of structure to the central line. In contrast, the outward scanning method scans from the central line to outside edges. Both inward and outward methods produce a symmetric profile with different refractive index distribution. For waveguide writing, outward scanning gives a smaller mode field diameter than inward scanning because the stress in the centre of the waveguide is higher. However, while symmetric, the index profile is not even (because it is essentially similar to two multiscans joined back-to-back), which is unsuitable for devices requiring uniform profile such as diffractive optics. The multiscan, inward, and outward scan techniques benefit from their simplicity, being quick to code for prototype testing.

The more complex segmented multiscan approach divides the structures into several parts, and scans in a multiscan way for each part, with the scanning order cycling through each part. For Gaussian beam written waveguides, the modification is fairly symmetric and also uniform. However, with Bessel beam writing for high aspect ratio structures, it does not give sufficient uniform index modification, because after the first set of major-separation scan-lines are written, the second set is written next to it, separated only by minor separation. Finally, the halfscan can be considered an improved version of the segmented multiscan and works well for Gaussian and Bessel beams, i.e. for both low and high aspect ratio modifications. It gives both symmetric modification as well as much improved uniformity, especially with high power writing. Apart from DOEs and waveguides, our stress controlling method could be further extended to laser machining and large waveguide fabrication, where uniform stress control is essential but challenging.

## 3.3 Multicore Fibre Sensor

While we have so far focused on inscribing test waveguides as a tool to evaluate the index change, determine suitable writing parameters, and optimise the scanning technique to improve stress distribution, the waveguides themselves benefit from low loss, highly precise geometry and excellent consistency. As such, they may be utilised in many applications. In this section, we applied the waveguide writing technique to fabricate a multicore fibre (MCF) directional bend sensor. The work was conducted in collaboration with the University of the Basque Country Arrizabalaga et al. (2020). We present a 7-core fibre based sensor capable of distinguishing curvature orientation. I am responsible for the fabrication part of the fibre sensor.

### 3.3.1 Working Mechanism

In principle, for a multicore fibre, each of the fibre cores can act as a separate waveguide, so light can independently propagate through those cores. However, if the distance between the cores is small, mode coupling between the cores takes place because the corresponding mode fields have a significant spatial overlap Yamashita et al. (1985). That is to say, the light which is initially coupled into one core can eventually be coupled over to other cores. The exchange of light between the cores is extremely sensitive to external influences such as strain or temperature changes. A MCF sensor has already been reported Villatoro et al. (2017), however, it was fabricated with an identical index for all cores and with symmetric geometry. This fact restricts efficient exploitation of the mode coupling between cores because the effect is not sensitive to complementary actions e.g. distinguishing curvature orientation. With the help of the fs laser induced stress, we can distinguish the orientation by breaking the symmetry.

Our sensor is based on a strongly-coupled 7-core fibre fabricated at the University of Central Florida (Orlando, USA) by the well-established stack and draw method. The MCF consists of a symmetrical structure formed with a central core surrounded by another six cores made of silica doped with germanium and embedded in pure silica cladding. The numerical aperture of the cores at $\lambda = 1.55$ $\mu$m is 0.14, matching with a standard SMF. The radius of each core is $r = 4.5$ $\mu$m with a core-to-core pitch of $d = 11$ $\mu$m.

The sensing mechanism is based on breaking the refractive index symmetry around the central core. One of the external cores is modified by femtosecond laser direct writing to increase the refractive index of a selected volumetric region within the fibre (see Fig. 3.16(a)). The laser pulses permanently change the refractive index of the irradiated zone. The index profile is asymmetric with respect to the bending plane and

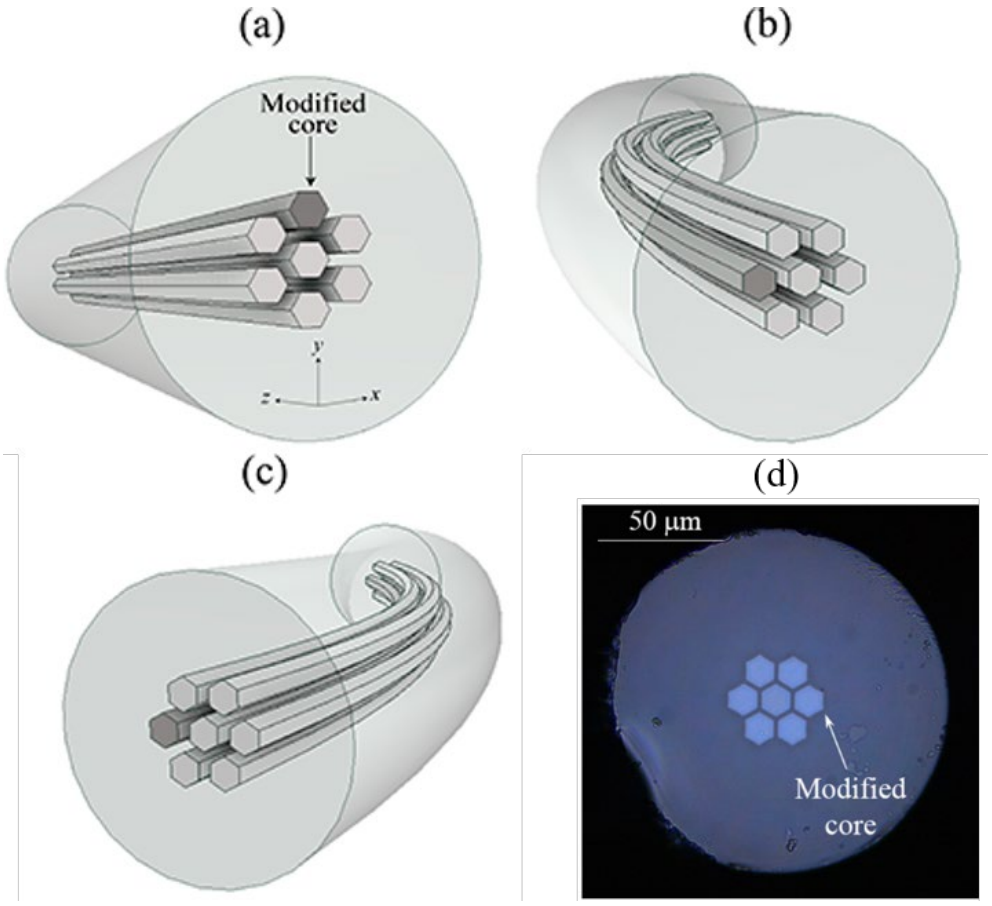


FIGURE 3.16: (a) Illustration of the distribution of the cores of the modified MCF when the index profile is symmetrical respect to the bending plane. (b) and (c) Illustrations when the modified MCF is rotated 90 degrees with respect to the reference. The index profile is asymmetrical with respect to the bending plane and it varies depending if the written core experiences tension or compression. (d) Microscope image of the multicore fibre cross-section. The modified core is not able to visually observe because the refractive index change is relatively small.

it varies depending if the written core experiences tension or compression (Fig. 3.16(b) and (c)), thus detuning coupling conditions with the neighbouring cores. Fig. 3.16(d) shows the microscope cross-section image of our MCF.

The dimensions of the inscribed structure were $10 \times 10$ $\mu$m in cross section and 4 cm in length, similar to a segment of the waveguide. During inscription, the laser writing power was set to 6 mW after the 0.4 NA objective, which corresponds to a single laser pulse energy of 30 nJ (due to the presence of dopants in the fibre, this energy is lower than for pure silica which would be $\sim$100 nJ). Since the purpose was to break the symmetry of the fibre core region, the multiscan method was applied. The pulse density was $3\times10^5$ pulses/mm along each scanline, and the separation between scanlines was 200 nm. With the help of the monitoring camera, it is possible to resolve the edges of the cores when focusing at different heights, and the fibre can be positioned with high repeatability using the laser writing stages to ensure the pulses

focus into one of the non-central cores. The written structure has a height and width of about 10 $\mu$m, which allows the fully cover of one fibre core region. In fact, since the symmetry break can be realized even with the structure only partially inscribed in the core, the writing process has a large positioning tolerance.

### 3.3.2 Results

We launched broadband light from a supercontinuum source coupled to the MCF to a single mode fibre, and connected the output to an OSA (Yokogawa AQ6370D) for spectrum monitoring. As the output spectrum consists of a series of peaks from supermode beating, here we focus on one peak and study its peak wavelength shift. By bending the MCF in the directions shown in Figs. 3.16(b) and (c), we found when the bending causes expansion (tension) in the written core as it is illustrated in Fig. 3.16(b), the spectrum red-shifts, while when the bending causes contraction (compression), the spectrum blue-shifts. The wavelength shift is caused by the supermode beating, the MCF is designed so that there are two mainly supermodes beating in the cores Villatoro et al. (2017). As such, it is able to discriminate the bend direction by the shift polarity. In Fig. 3.17(d) we have plotted these wavelength shifts versus the bend angle. From this calibration, we found that the sensitivity of our sensor for positive and negative bending is -1.4 nm/degree and 1 nm/degree, respectively.

## 3.4 Conclusions

In this chapter, the laser writing parameters were tested by fabricating waveguide structures. By calculating the output mode field diameter of the waveguide's fundamental mode, the laser induced refractive index has been estimated as $7\times10^{-4}$ to $6\times10^{-3}$ for writing powers of $P_w$=35 mW to 55 mW. Then based on the waveguide writing method, a stress control technique for femtosecond laser written structures has been investigated. With this technique, we are able to eliminate the structural asymmetry in the index profile and stress distribution of waveguide-like structures. A more symmetric stress profile also improves the damage threshold so higher writing powers can be used, giving stronger $\Delta n$ and phase change. For high aspect-ratio Bessel beam written diffractive optics elements, a 36% of diffractive efficiency improvement for a 50/50 grating was achieved compared to the standard multiscan writing technique. A two-layer Fresnel lens with a focal efficiency of 55% was also demonstrated. For low aspect-ratio Gaussian beam written waveguides, a more symmetric mode profile was achieved using the improved scanning technique. Finally, as for the application side, the waveguide writing technique was applied to

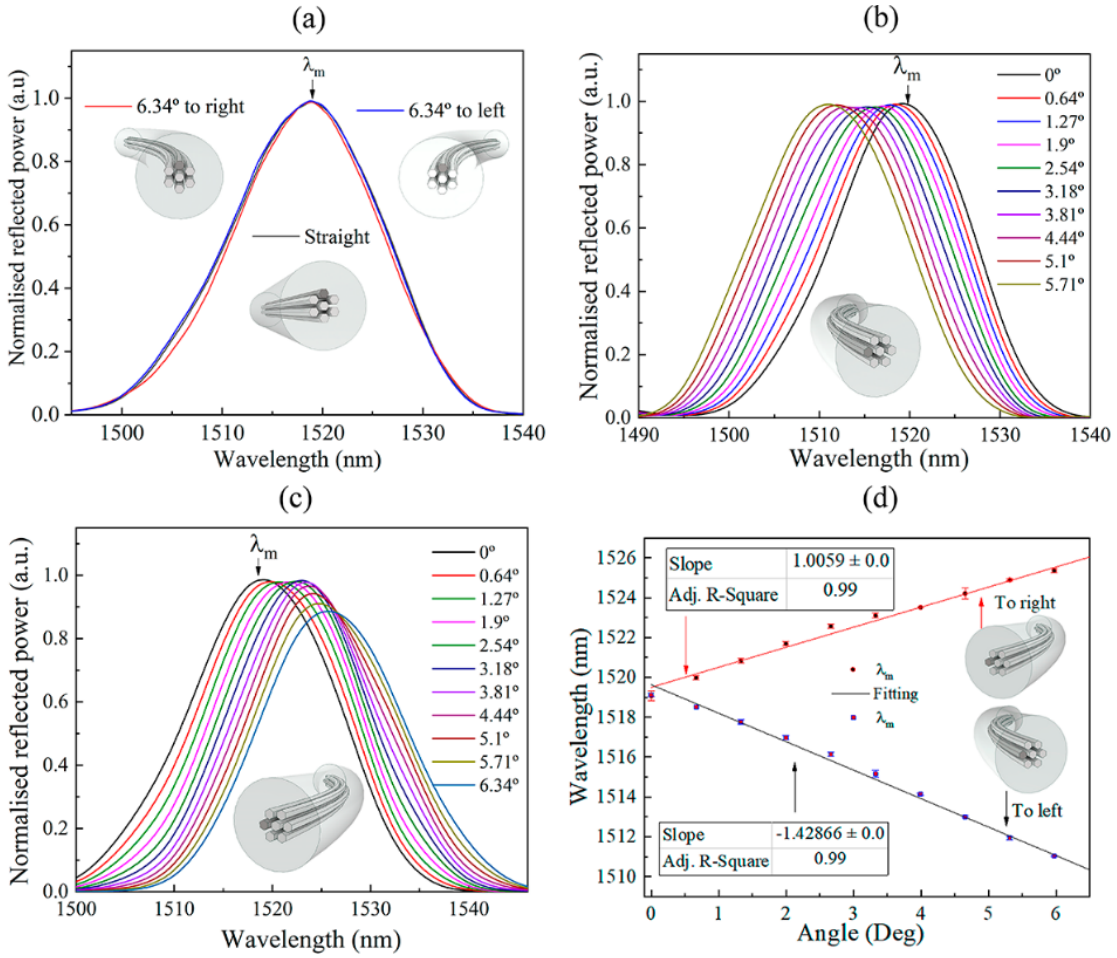


FIGURE 3.17: (a) Experimental vector bending spectrum of the MCF device with symmetric index profile with respect to the bending plane. (b) and (c) The same but with asymmetric index profile. (c) Peak wavelength versus angle for both directions of vector bending.

fabricate a multicore fibre based bending sensor capable of resolving bend direction, for which a sensitivity of -1.4 nm/degree was achieved.

# Chapter 4

# Diffractive Optical Elements

In this chapter, having now estimated the $\Delta n$ induced by laser writing, we will start to design, fabricate and test the femtosecond laser written Fresnel lens. We will first simulate the Fresnel zone plate (FZP) in MATLAB to determine the focal properties and diffraction efficiency. Then, for experimental writing, the suitability of Gaussian and Bessel inscription beams will be compared. Next, the focal and imaging characterisations of the written FZP will be evaluated at different wavelengths and the diffraction efficiency will be also measured. Finally, by inscribing and characterising diffractive gratings, an alternative method for estimating induced index will be presented.

## 4.1 Fresnel Lens

### 4.1.1 Design and Simulation

A binary Fresnel zone plate (FZP) model was first been simulated as shown in Fig. 1.9. To simplify our model, I assume an infinitely thin FZP, which is modelled as a phase mask with the same phase profile as the FZP onto which the input field is incident. This allows the key underlying physics to be studied.

I designed a binary FZP with a maximum phase change of $\pi$ and 1 cm focal length for a wavelength at 550 nm (shown in Fig. 4.1). As I will later characterise the FZP with red, green and blue LEDs, the designed wavelength was chosen to match the central green colour. The phase axis shows how much phase change $\Delta\phi$ should be induced for the ideal binary FZP, and $\Delta\phi$ is related to the physical thickness $h$ of the modified material and induced refractive index difference $\Delta n$ according to Eq. 1.1.

A 2D propagation simulation was performed according to the Rayleigh-Sommerfeld diffraction solution Voelz (2011) to find the intensity distribution after the FZP and

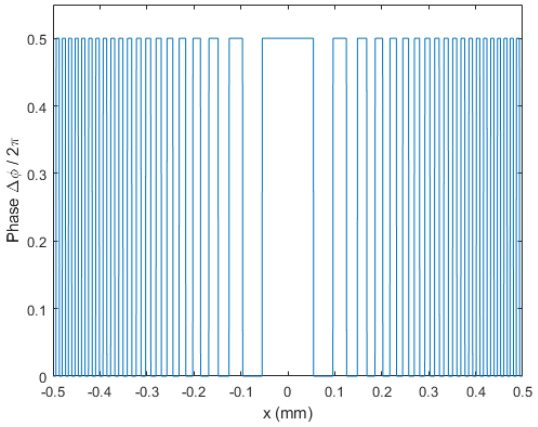


FIGURE 4.1: Phase profile of ideal 1 mm diameter 1-layer (binary) FZP for 550 nm wavelength. Phase axis normalised to $2\pi$. This profile is used as a phase mask to model the FZP in simulations.

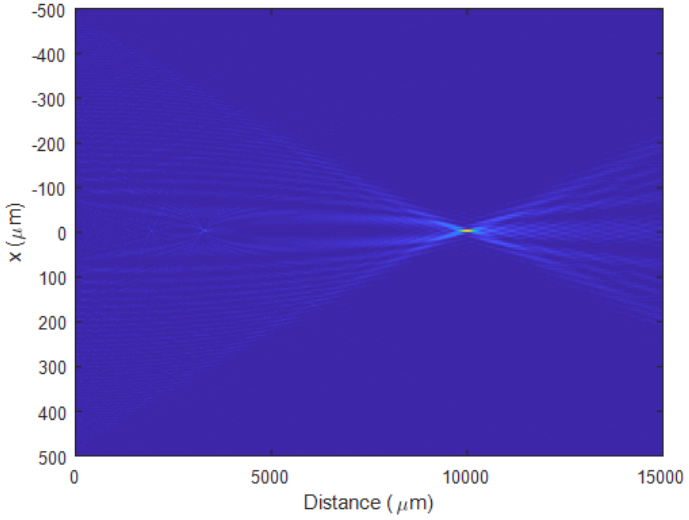


FIGURE 4.2: Propagation simulation of intensity profile after 1-layer (binary) FZP with 550 nm Gaussian beam incidence. $x$ is the transverse FZP axis, same as in Fig. 4.1. FZP plane is at $z$=0 designed with 10 mm focal length and 1 mm diameter.

hence the focal properties, assuming a 550 nm green input light with a Gaussian profile and diameter of 1 mm. The results in Fig. 4.2 show that the main focus appears at 10 mm after the lens, which matches the designed focal length.

After that, the dispersion property is simulated by solving the intensity profiles with wavelengths from 400 nm to 700 nm and taking intensity cutlines along the central FZP axis (along $x$=0). Figure 4.3 shows the results. The FZP shows anomalous dispersion where shorter wavelengths focus further away than longer wavelengths. With the FZP designed for 550 nm, the focal length for 400 nm beam is at 13.75 mm, and for 700 nm, 7.85 mm. We calculate this focal shift per nm as 1.18 $\mu$m/nm. Multiple peaks (secondary focal points) are also found in the figure, they are caused

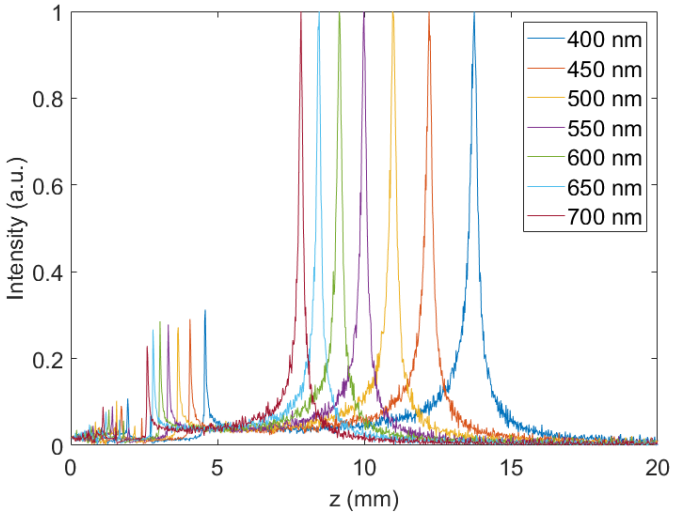


FIGURE 4.3: Simulated intensity cutlines taken along central axis of binary FZP for different wavelengths. Design wavelength is 550 nm with a 10 mm focal length.

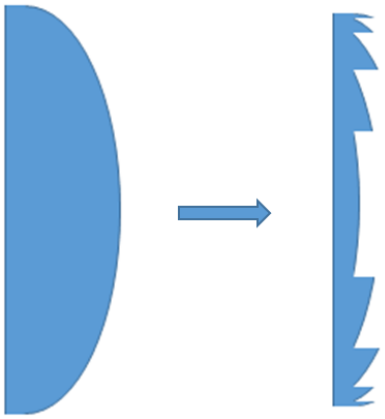

FIGURE 4.4: Principle of Fresnel lens design (right) based on modification of the traditional refractive lens profile (left).

by the unequal gap between each zone of the FZP thus causing different diffraction angles Higbie (1976).

The diffractive Fresnel lens is a multi-layer version of the FZP, with a phase profile which is designed by starting with the traditional refractive lens (shown in Fig. 4.4) and removing the extra material which has no contribution to the total phase change of incident beam (i.e. regions which increase phase by multiples of $2\pi$). Therefore, the ideal Fresnel lens has a thinner structure but similar performance as a refractive lens.

For the structure design of our Fresnel lens phase profile, we start from the phase mask of a traditional parabolic refractive index lens shown in Fig. 4.5(a). After removing all the integer multiples of $2\pi$ phase change inside the lens, which have no contribution to net phase change, the remaining part shown in Fig. 4.5(b) is the Fresnel

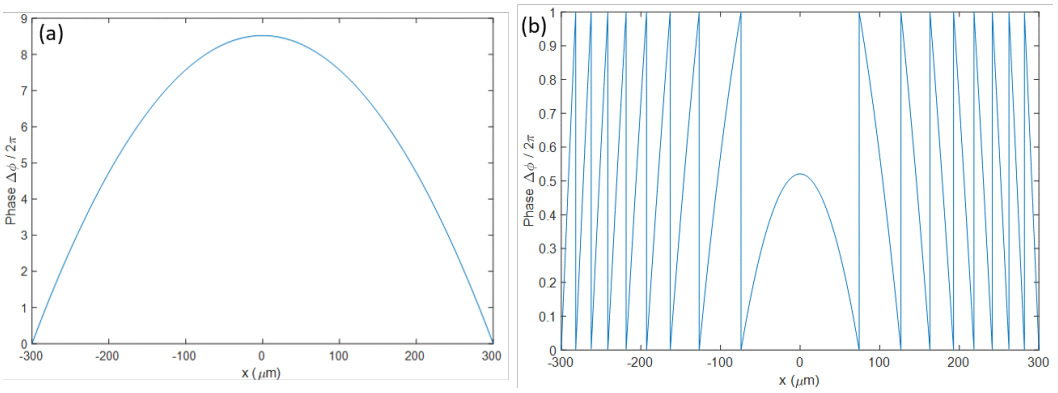


FIGURE 4.5: (a) Phase profile of conventional parabolic lens and (b) designed ideal Fresnel lens.

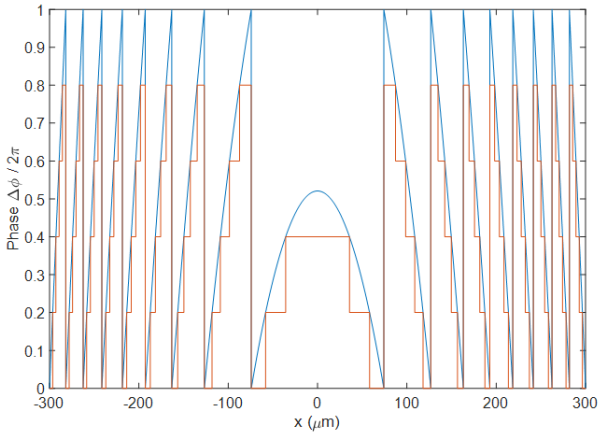


FIGURE 4.6: Design of a 4-layer Fresnel zone plate phase profile (red) based on the ideal Fresnel lens profile (blue). $x$ is in radial direction.

lens. From this, we can produce an $N$-layer FZP by discretizing the profile into $N+1$ levels. For example, a phase mask for a 4-layer FZP is shown by the red profile in Fig. 4.6. Assuming an FZP of $L$ layers, the phase change for each layer $\Delta\phi_s$ is:

$$\Delta\phi_s = 2\pi \cdot \frac{1}{L+1} \tag{4.1}$$

According to equation 1.1, the thickness $h_s$ of each layer can be calculated as:

$$h_s = \frac{\lambda}{\Delta n} \cdot \frac{1}{L+1} \tag{4.2}$$

Compared with the binary FZP in Fig. 4.3, the focal intensities (main peaks) for the 3-layer FZP plotted in Fig. 4.7 are much stronger. For a better comparison, the diffraction efficiency of the FZP, defined as the ratio of the power in the peak (where intensity is within $1/e^2$ of max) and input power, has been calculated. Figure 4.8

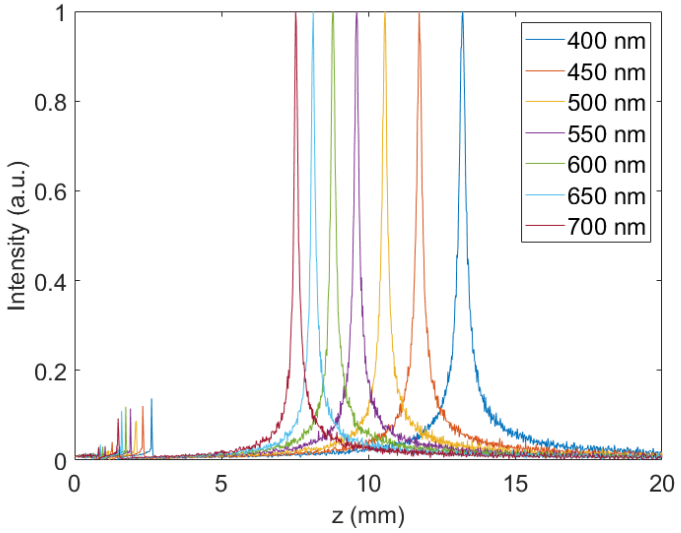


FIGURE 4.7: Simulated intensity cutline after a 3-layer FZP along $x = 0$ with wavelengths from 400 nm to 700 nm. The FZP was designed for the 550 nm wavelength and 10 mm focal length.

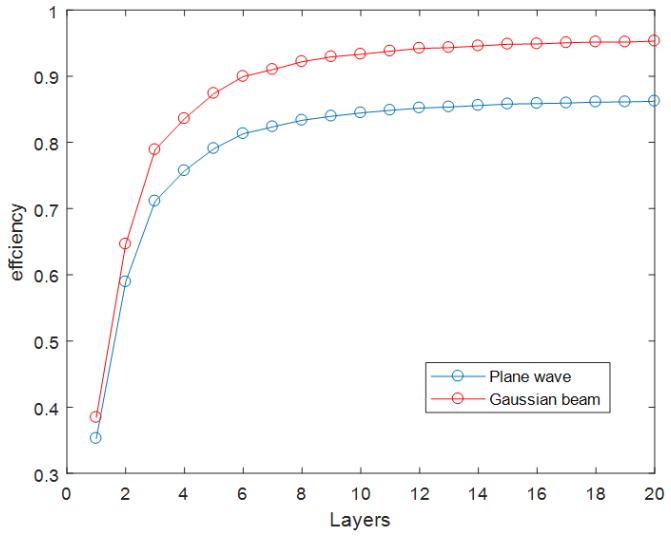


FIGURE 4.8: Simulated diffraction efficiency against number of FZP layers, for Gaussian beam ($\omega_0$ = 300 $\mu$m) and plane wave input. Design wavelength is 550 nm and diameter is 1 mm.

shows the efficiency plotted against number of FZP layers for both Gaussian and plane wave incidences.

The trends for both input waves are similar. The efficiency increases rapidly before 5 layers, then tends to plateau before 10 layers and finally becomes stable. This is reasonable because with more layers, the FZP $\Delta\phi$ profile will become more smooth and hence reduce edge diffraction. For plane wave incidence, the efficiency attains up to 85%, while for Gaussian beam incidence, it finally reaches 95%. The efficiency difference between two incident beams is that plane wave can produce a rectangular

shape beam after FZP and focus into a sinc profile as would be expected through Fourier propagation, which will reduce the intensity of the central peak, while for Gaussian beam, the beam shape will retain the same profile through propagation, hence has a higher efficiency.

### 4.1.2 Experimental Fabrication

#### 4.1.2.1 Gaussian Beam Writing

First, we must investigate whether a focused Gaussian beam or focused Bessel beam would be the more suitable tool for inscribing diffractive structures. From the simulation results in Fig. 4.8, we found that with a 3-layer FZP, the efficiency already reaches ∼80% for Gaussian beam incidence. According to Eq. 4.2, the more layers we have, the shorter the height $h_s$ for each layer. With reference to the $\Delta n$ we calculated in Section 3.1, which is $7\times10^{-4}$ to $6\times10^{-3}$, for a design wavelength of 550 nm the structure height for a binary FZP can be calculated as $50-390$ $\mu$m, while for a 3-layer FZP, it is $20-200$ $\mu$m.

We conducted a waveguide writing test with different writing powers and objectives of various NAs for finding the writing structure depth. With the standard Gaussian beam writing, we found the writing depth is normally $<$25 $\mu$m (shown in Fig. 4.9), which is not enough for a single layer of an efficient 3-layer FZP.

However, notice that in Eq. 4.2, the more layers of the FZP, the shorter the height required for each layer. According to the $\Delta n$ we calculated in section 3.1, we need $\sim 10$ $\mu$m height per layer if we are writing 10-layer grating. This then can be achieved by Gaussian beam writing.

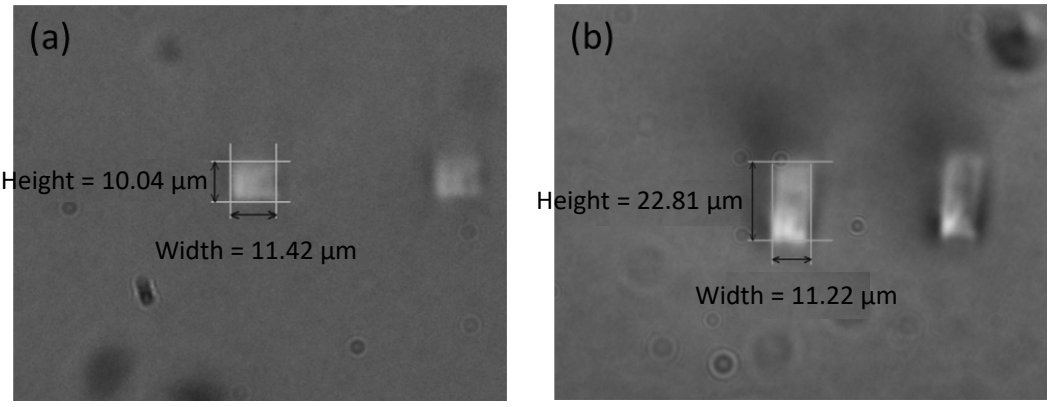


FIGURE 4.9: Microscope image of test waveguide cross sections written with (a) 0.6 NA with writing power of 25 mW and (b) 0.4NA and 60 mW. A weaker NA and stronger power offers taller structure height.

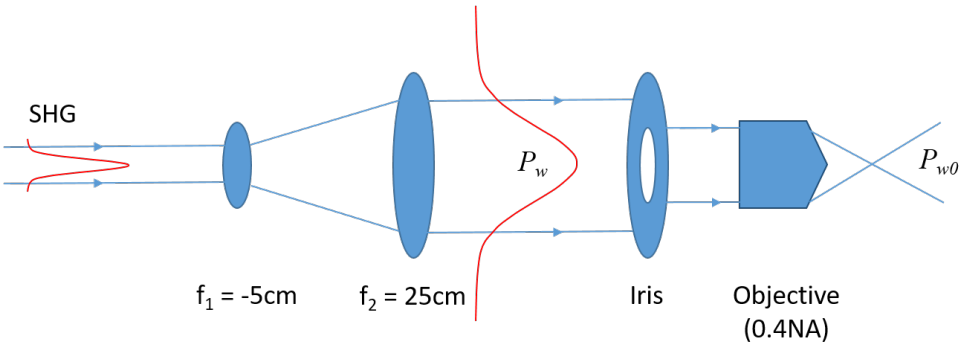


FIGURE 4.10: Experimental setup for modified second harmonic writing. The beam is magnified by beam expander system with ratio M = 5, which enhances intensity uniformity in the central area of beam. Iris sets NA of beam focus.

In order to increase the writing depth with a Gaussian beam, we added an iris before the objective (see Fig. 4.10). By reducing the diameter of iris, we can reduce the NA of the beam focus, which will increase the laser writing region's height. During laser writing, here we define the average power before iris as $P_w$ and power after objective as $P_{w0}$. With the improved setup, using different transmission of iris to control beam width and focusing NA, we wrote and measured test straight waveguides with different pulse densities (shown in Fig. 4.11).

The transmission percentage of iris means the power measured after objective compared to the power with 100% iris open. As the transmission increases, we obtain a shorter waveguide due to the tighter focus.

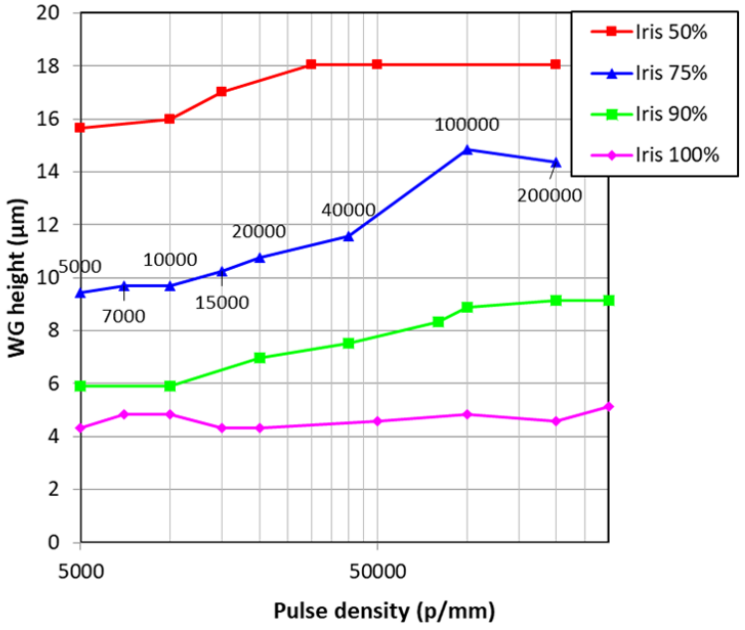


FIGURE 4.11: Waveguide height against pulse density, for different iris apertures. Percentage indicates fraction of light passing through iris.

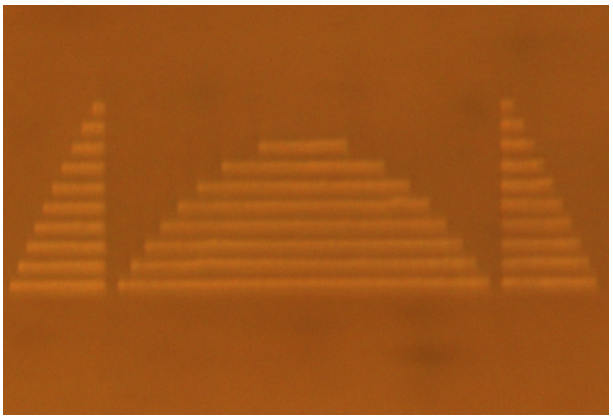

FIGURE 4.12: Microscope image of test Fresnel grating cross-section with writing density of 10,000 pulses/mm, writing speed = 10 mm/s, power before iris $P_w$ = 22 mW, writing power after objective $P_{w0}$ = 12 mW, layer height is 10 $\mu$m. The structure is written 0.5 mm below substrate surface.

Tests were then conducted to fabricate the multi-layer structure. To begin with, we wrote a 2D version of the FZP, i.e. a Fresnel grating, which enables us to observe and verify the cross-section easily. In our case, we chose an iris setting of 75% as it produces roughly 10 $\mu$m writing depth, which is suitable for multi-layer ($\sim$10 layers) structures. Also, we used a pulse density less than 40,000 pulses/mm to maintain the height and save writing time.

Fig. 4.12 shows the central zones of a 10-layer Fresnel grating. From the cross-section, we can now observe a visually smooth multi-layer structure . We are here showing that the Gaussian beam is well suited for writing FZPs with a larger number of layers. However, the more layers we write, the more overlap or gap between layers and thus greater error from the ideal profile. On the other hand, more layers also means longer fabrication time. For these reasons, we will use the Bessel beam writing in the next section, as well as for most lens fabrication work discussed subsequently.

#### 4.1.2.2 Bessel Beam Writing

For extending the writing height, as discussed in section 1.2.1.3, the Bessel beam can be applied in our experiment. The setup for Bessel beam generation using an axicon is shown in Fig. 2.1. Also, for achieving a higher writing resolution, the writing experiments were carried using the 515 nm second harmonic beam.

With the Bessel beam, in order to optimise the writing conditions and check depth, a series of straight test waveguides were inscribed and characterized using different powers and objective NAs (shown in Fig. 4.13). In Fig. 4.13(a), the middle of the structure is damaged by the Bessel beam (dark area) due to a relatively high writing power (105 mW) and uneven intensity distribution along the Bessel beam. In Fig. 4.13(b), by decreasing the writing power and objective NA, we achieved a clearer

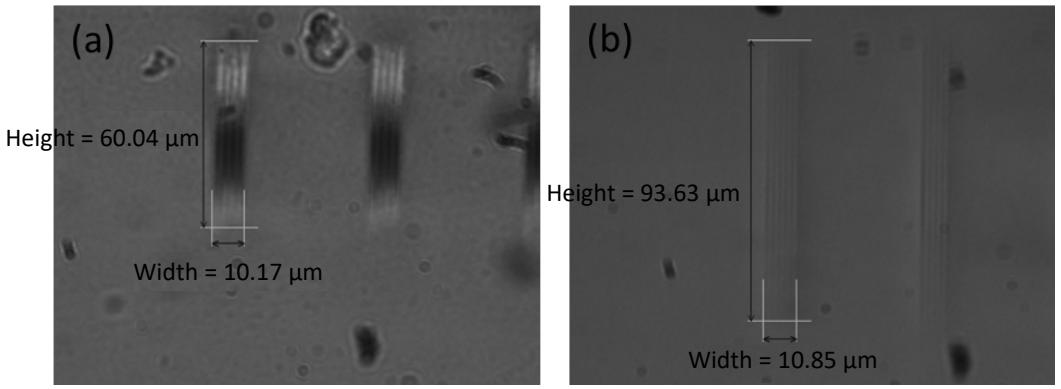


FIGURE 4.13: Microscope image of the test waveguide cross section written using a Bessel beam for (a) a writing power $P_w$ = 105 mW with 0.4 NA and (b) 70 mW with 0.25 NA.

structure with $\sim 100\mu m$ height, which is 5 times greater than that of Gaussian beam writing (Fig. 4.9). This is within the required height range we calculated for a single layer FZP.

For a more detailed parameter test, Fig. 4.14 shows the cross section of Bessel beam written waveguides with different writing powers and pulse densities. As the Bessel beam has a long Rayleigh range, the average writing power is much higher than with a Gaussian beam but the writing depth is much longer.

Along the laser firing direction (left to right in Fig. 4.14), we noticed an uneven brightness along the waveguide cross section due to the uneven intensity distribution along the Bessel beam axis. Additionally, we also noticed that the writing density and power do not seem to change the height of waveguide structure significantly. This is because the long Rayleigh range of Bessel beam means the power must be increased considerably to observe a noticeable height change as it is distributed over a larger volume. Since the silica modification relies on a nonlinear absorption process, the required intensity for elongating the structure height will be much greater than for smaller sized beam focus. Besides, even at sufficient power levels, the higher intensity middle part will be damaged first. So varying the normal writing conditions will not significantly affect the thickness of the Bessel beam written structure.

With a suitable writing power and density, we then wrote several FZPs. Figure 4.15 shows the microscope cross section view of a 3-layer FZP written by Bessel beam. The height of each layer is $\sim$100 $\mu$m and total height is $\sim$300 $\mu$m. With a writing speed of 10 mm/s, the first (bottom) layer takes 3.5 min to write and the overall writing time for the 3-layer FZP is 7.5 min.

Fig. 4.16 shows the top view of a binary FZP and 4-layer FZP. The top view of the 4-layer Fresnel zone plate (Fig. 4.16(b)) shows a higher contrast compared to the binary FZP (Fig. 4.16 (a)).

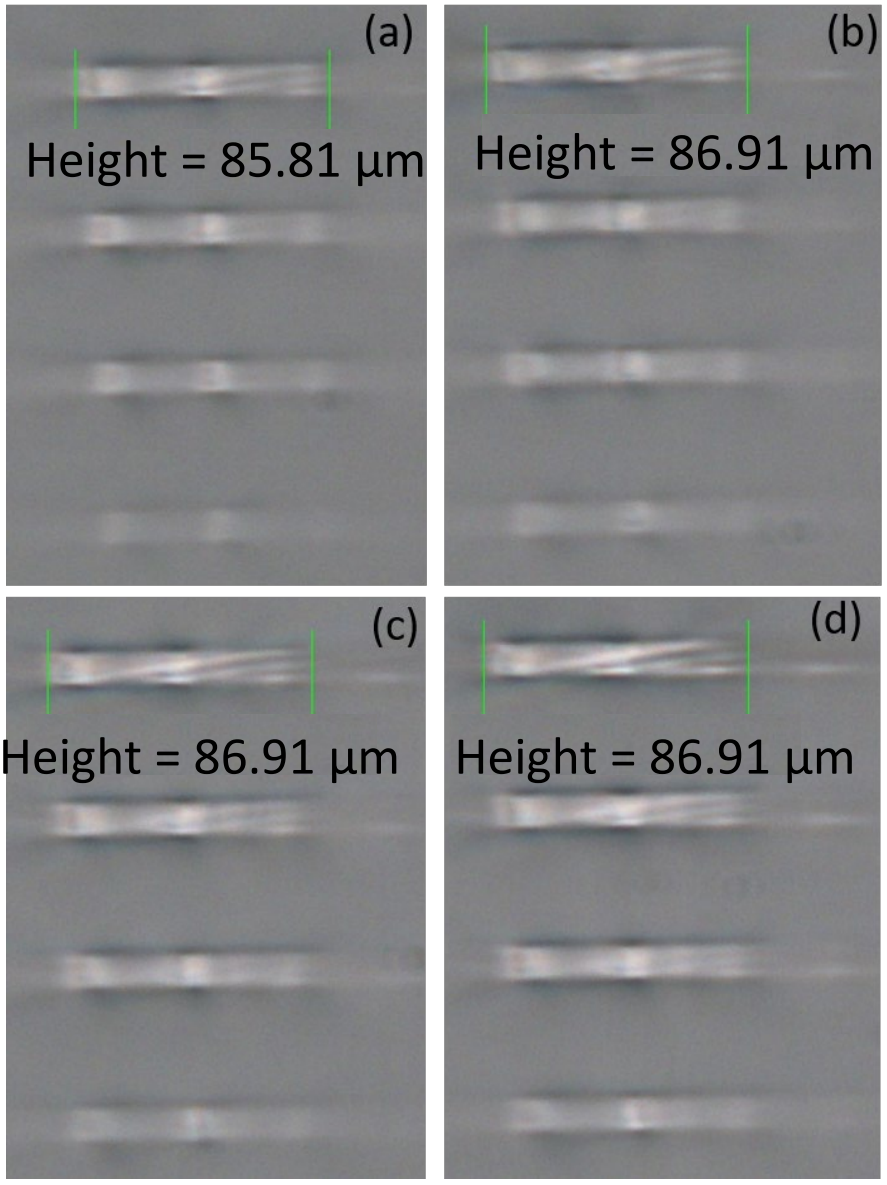


FIGURE 4.14: Cross sections of Bessel beam written waveguides with writing powers of (a) 130 mW, (b) 140 mW, (c) 150 mW, and (d) 160 mW.Writing beam direction is left to right, scanlines written bottom to top.

Compared to Gaussian beam writing, the Bessel beam is an ideal option for writing FZPs with a few layers, which require a relatively tall height for each layer. However, for writing more layers (>10), as the Bessel beam has a deep writing depth, the total thickness would be limited by sample thickness. Also, there are drawbacks for Bessel beam writing, particularly the uneven intensity distribution along the writing direction, which will increase the uncertainty of total $\Delta n$ and thus total phase change when increasing layers. So for different applications, choosing the most appropriate writing beam is also very important.

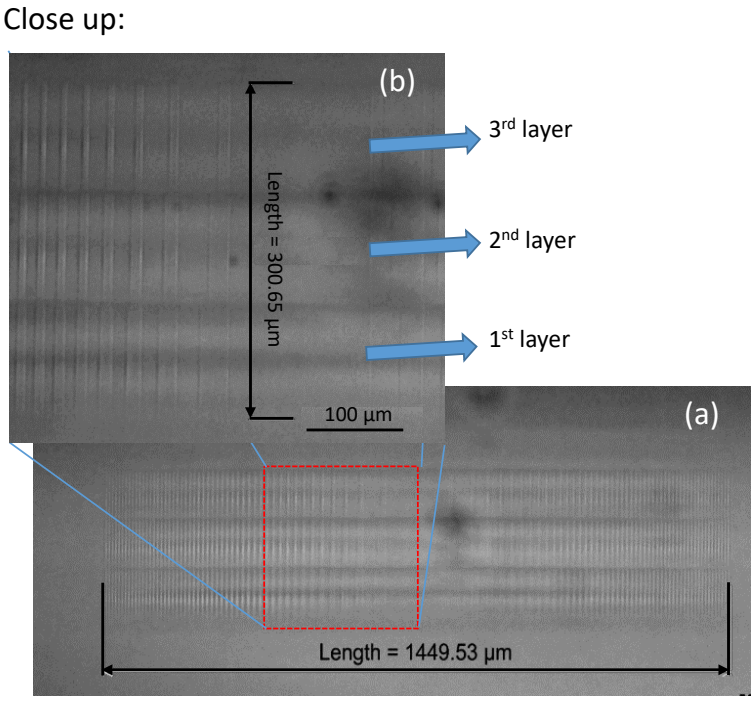


FIGURE 4.15: (a) Cross-section of a three-layer FZP written by Bessel beam with writing power of 70 mW. (b) Close up view.

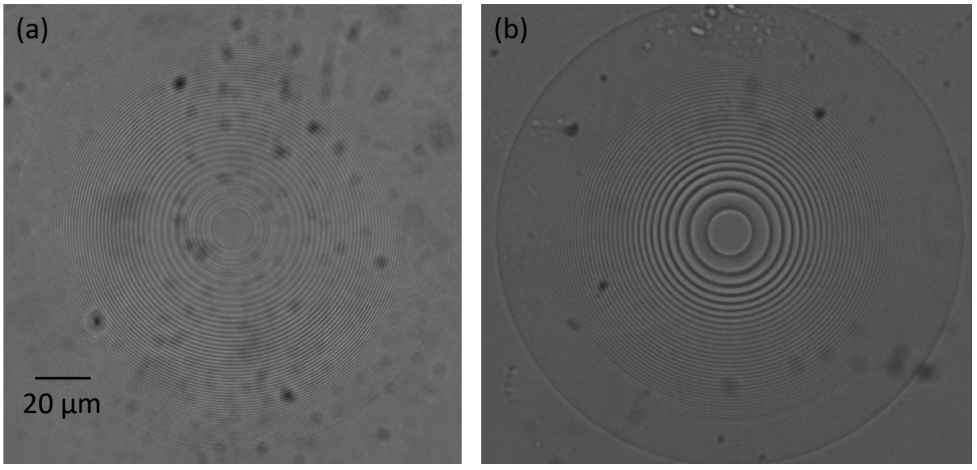


FIGURE 4.16: Microscope image top view of (a) binary FZP and (b) 4-layer FZP. The diameter of the FZPs is 1.45 mm. The writing power $P_w$ = 70 mW, pulse density $D$ = 4000 pulses/mm, objective NA = 0.25.

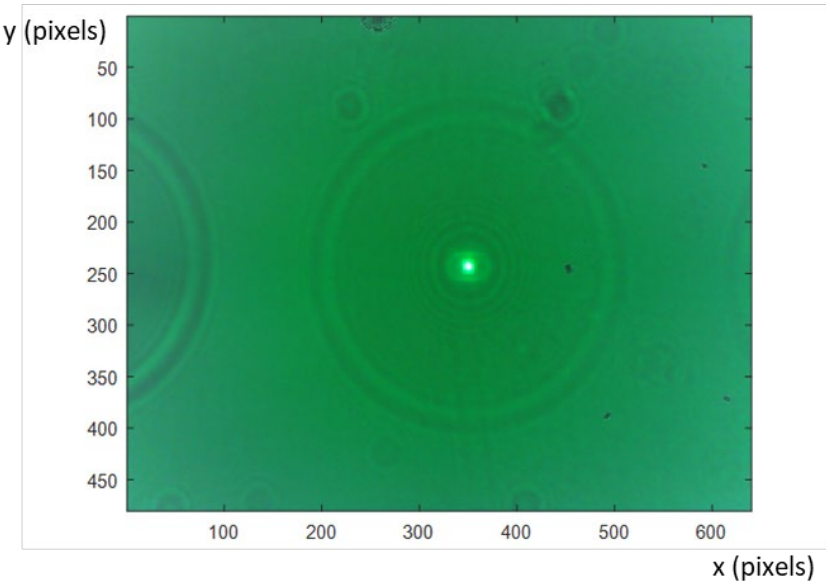


FIGURE 4.17: Image captured at focal plane of 3-layer Fresnel lens with a diameter of 1.45 mm and 1 cm designed focal length.

### 4.1.3 Characterisation Results

In this section, we will start to characterise the Bessel beam fabricated FZPs with an RGB LED source. A 3-layer FZP was used for the focal and imaging properties investigation, while various FZPs were evaluated for the focal efficiency test.

#### 4.1.3.1 Focal Property

The FZP focal property is characterised with the setup in Fig. 2.8. By changing the longitudinal $z$ position of the camera with the stage, we found the focal image of the 3-layer FZP (Fig. 4.17). From the image, we can also observe the rectangular shape of the LED source in the middle of the image. To characterise the dispersion properties of the FZP, we captured the images at different longitudinal positions near the focal length with the three different wavelengths of the RGB LED (shown in Fig. 4.18: colour scale is logarithmic for a better contrast).

From the graph, the focal length for red is shorter than green and then blue. For a more straightforward comparison, we have set the longitudinal axis to zero at the focal point of green light; therefore, the focal length for red light is $1.25\pm0.25$ mm closer and for blue light it is $1.75\pm0.25$ mm further from the lens. Compared with the simulated results for an RGB LED in Fig. 4.19, the focal position difference between red and green light is 1.59 mm and the difference of green and blue light is 1.53 mm. The discrepancy could come from the measurement error where the focal point is hard to judge precisely by the image.

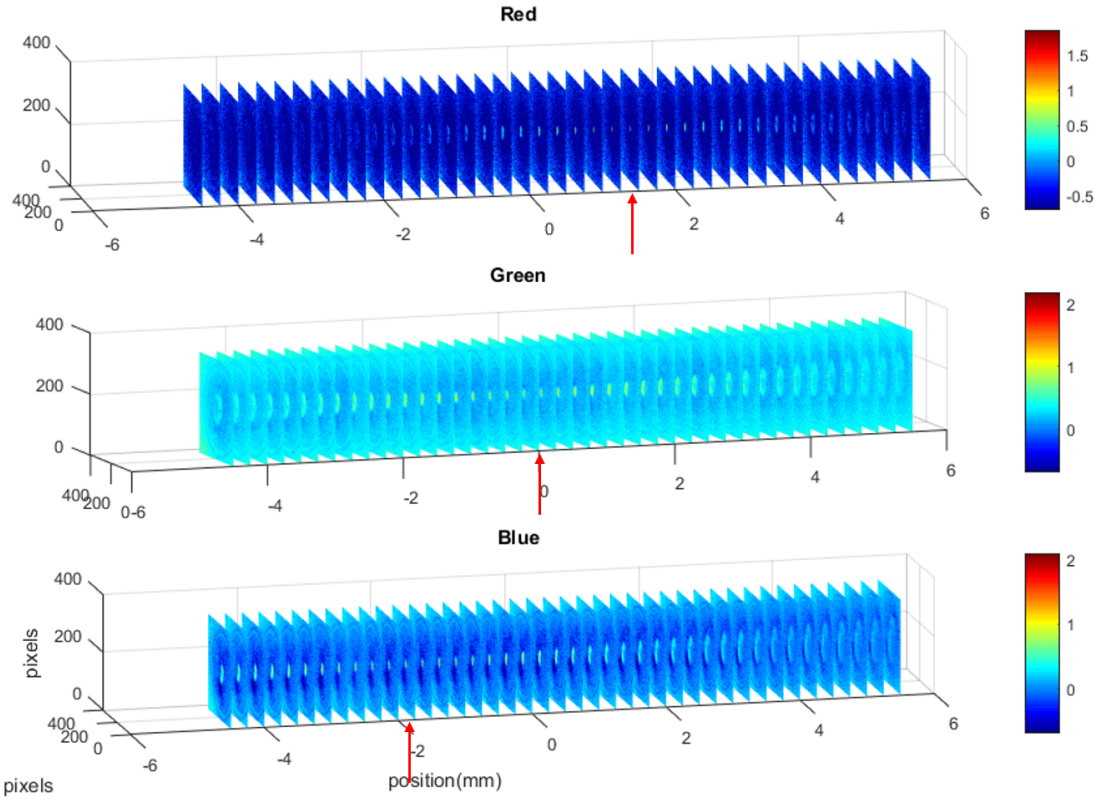


FIGURE 4.18: Measured intensity profile slices after 3-layer FZP around the focal point. The red arrow points at the focal plane. FZP is at right side of graph, larger position axis value means closer to FZP. Colour scale is logarithmic.

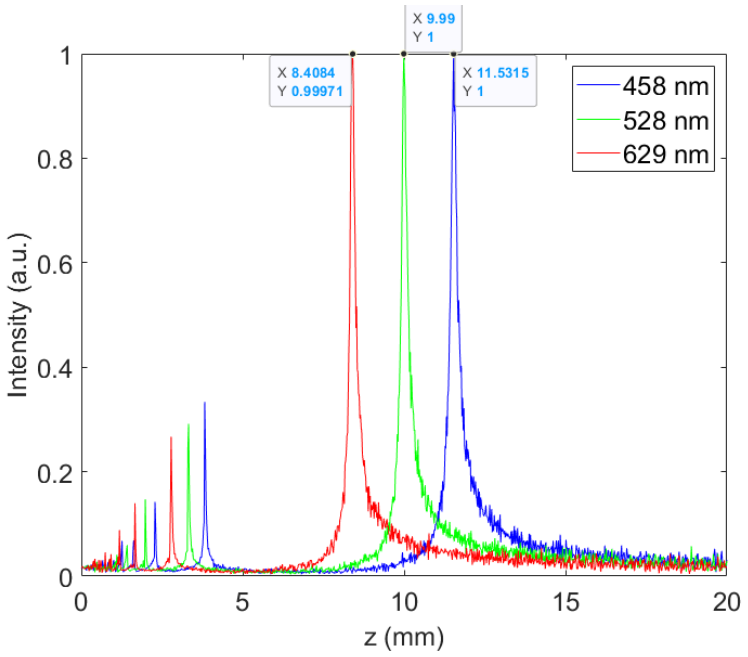


FIGURE 4.19: Simulated intensity cutline along central axis of 3-layer FZP for RGB LED wavelengths. The $z$ axis position data tips show the focal points of RGB LED which is 8.40 mm for 629 nm, 9.99 mm for 528 nm and 11.53 mm for 458 nm.

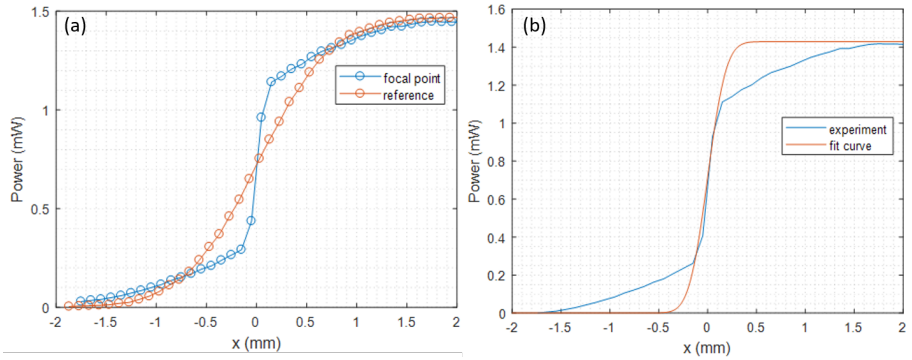


FIGURE 4.20: (a) Knife edge measurement showing transmitted power after edge with (blue) and without (red) the FZP, and (b) fitted curve based on matching theoretical transmission near the $x = 0$ central focal region.

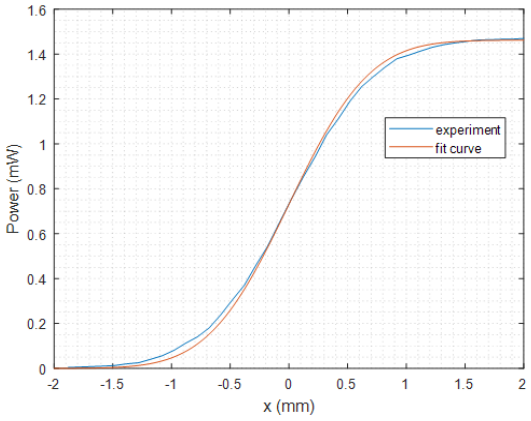


FIGURE 4.21: Knife edge measurement of HeNe laser source beam and its fitting, to confirm 1 mm beam radius.

#### 4.1.3.2 Focal Efficiency

Before measuring the focal efficiency of the FZPs, a beam profile characterisation is performed with the knife-edge profiling method. Figure. 2.10 shows the experimental setup, Figure 4.20(a) shows the power after the moving blade, where the blue curve shows the beam after the Fresnel lens and red curve shows the beam without Fresnel lens. The red curve in Fig. 4.20(b) shows the best-fit curve (based on theoretical blade profiling of a Gaussian beam to match the central region).

The fitting in Fig. 4.20(b) shows the focused beam waist is ∼0.3 mm. We also fitted the collimated beam from the HeNe source light which was confirmed to be ∼1 mm in size (fitting curve shown in Fig. 4.21). The intensity profile measurement confirmed that our lenses are able to focus light well at the designed focal length and wavelength.

With the characterisation setup in Fig. 2.11, the efficiency of Bessel beam written FZPs can be measured. According to Eq. 4.1 and 4.2, the optimum layer thickness $h_s$ depends on the number of layers, which corresponds to different phase change per

TABLE 4.1: Efficiency of single-layer FZPs with different writing parameters.

| FZP | Density(pulse/mm) | Velocity(mm/s) | Separation(mm) | Efficiency | $\Delta n$ |
|---|---|---|---|---|---|
| A | 100,000 | 2 | 200 | 13% | $1.8 \times 10^{-3}$ |
| B | 100,000 | 2 | 100 | 18% | $2.0 \times 10^{-3}$ |
| C | 200,000 | 1 | 200 | 18% | $2.0 \times 10^{-3}$ |
| D | 200,000 | 1 | 100 | 23% | $2.5 \times 10^{-3}$ |

layer. Therefore several binary FZPs were written with different writing parameters to calibrate the index change.

Table 4.1.3.2 shows the diffraction efficiency measured for binary FZPs with different writing density and scanline separation. The scanline separation here can be treated as the inverse of density as evaluated perpendicular to the writing direction. We found as the density in both directions increased, the efficiency increases. According to the simulation, an index change of $6 \times 10^{-3}$ corresponds to $\pi$ rad phase change. So with 23% efficiency for FZP D, which corresponds to $2.5 \times 10^{-3}$ of $\Delta n$, we have a $\sim 0.42\pi$ rad phase change. We can then use FZP D as a tool to build a multi-layer FZP.

With the characterisation setup, the best FZP we wrote has an efficiency of 31% for a single layer FZP, 54% for a 2-layer FZP and 59% for a 3-layer FZP. These have a theoretical limit of 38%, 65% and 79%, respectively. For the 1 and 2 layer FZP, the experimental efficiency is already quite close to the theoretical limit while the 3-layer FZP still has 20% potential improvement. This may due to the structure uniformity issue at the deeper edge (in Fig. 4.14, the right edge is not as flat as the left.) This problem could be solved by using different scanning methods (which are discussed in section 4.2.3).

#### 4.1.3.3 Imaging Quality

The imaging property was investigated with the setup in Fig. 2.12. Figure 4.22 shows the images for 200 $\mu$m array lines and 600 $\mu$m array lines (microscope image shown in Fig. 2.13). The total dimension of our 200 $\mu$m pattern is $5 \times 5$ mm, which means we can get a clear image down to a resolution of 200 $\mu$m within the field of view of $\sim$7 mm diameter.

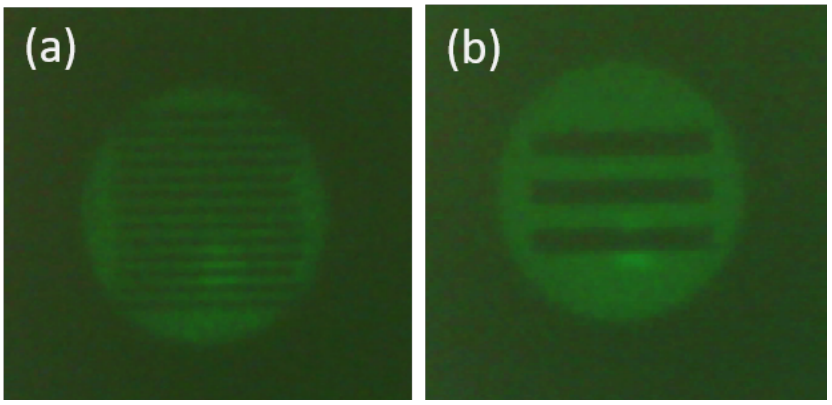


FIGURE 4.22: Focused image of array lines with (a) 200 $\mu$m and (b) 600 $\mu$m width and gap.

## 4.2 Diffractive Blazed Grating

In previous experiments with waveguides, the laser induced $\Delta n$ was calculated with waveguide's MFDs. However, this measurement is likely to have a lot of uncertainty since it involves comparison with simulation that assumes uniform square step index profile (which is probably graded in reality). Also, as now we are investigating diffractive elements, because the laser written strain pattern is not isotropic, measuring index in different directions may give different results. In this section, we will present an alternative more accurate approach to determine the refractive index change $\Delta n$ induced by the laser, through fabricating gratings and measuring their diffraction efficiency. We will characterise gratings written in silica and SF57 lead silicate glass. As the grating is the simplest diffractive element, therefore the characterisation results can also be used to evaluate the property of diffractive FZPs.

### 4.2.1 Design and Simulation

The design of the grating is based on the angle $\theta$ between the 1st order and zero order diffraction peaks. Figure 4.23 shows the $\theta = 1^\circ$ and $3^\circ$ 10-layer grating phase mask designs. For a larger diffraction angle, the grating has a tighter structure. Also, our grating is now designed for the 632.8 nm wavelength for easier characterisation with a HeNe laser beam.

We then use a similar beam propagation method as for the FZP to simulate the field and intensity after the grating. However, for the grating design, instead of using an ideal phase mask, we improved our design by using the true experimentally estimated refractive index change and real height of structure (according to equation 1.1). Figure 4.24 shows the simulated comparison of the ideal phase mask and practical mask.

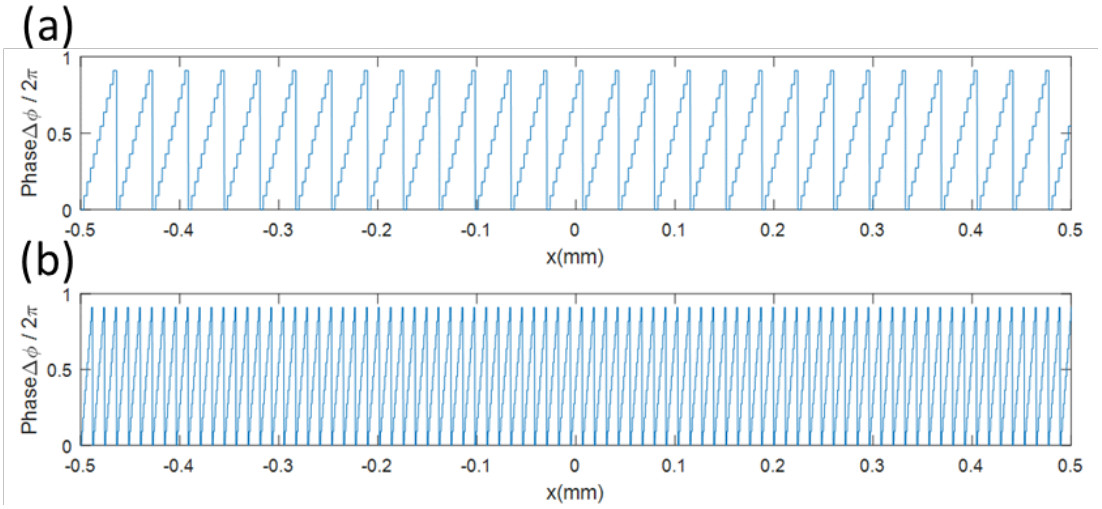


FIGURE 4.23: Grating phase profile design for (a) 10-layer 1° grating and (b) 10-layer 3° grating. Design wavelength is 632.8 nm.

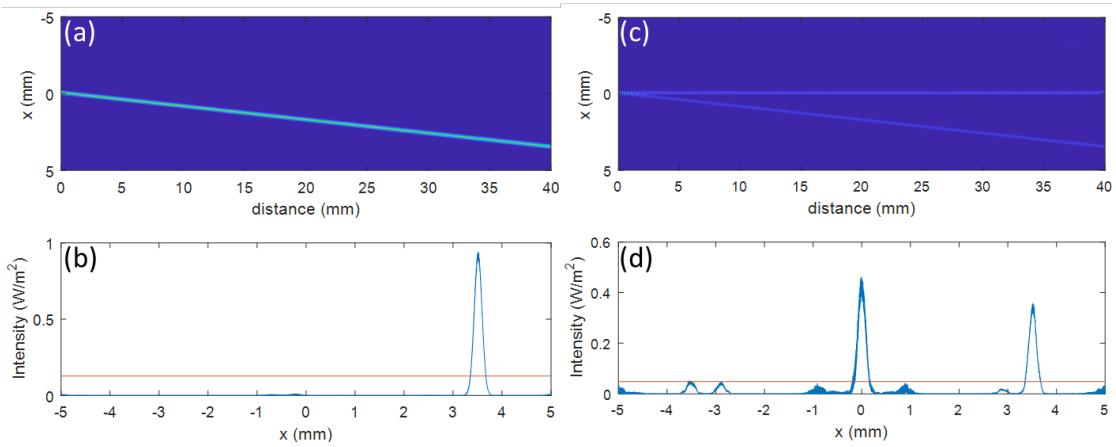


FIGURE 4.24: Simulations of the 10-layer $\theta$=5° grating. (a, c) Propagation simulation with the plane wave of 0.3 mm beam size with (a) perfect phase mask and (c) mask of 100 $\mu$m total thickness and 0.003 refractive index change. (b, d) Transverse (grating direction) intensity distribution at 40 mm away from the grating. Calculated first order diffraction efficiency for (b) is 92.9%, for (d) is 34.5%.

With an ideal phase mask, 93% efficiency can be achieved in theory. By altering the refractive index change, the efficiency for different $\Delta n$ is calculated (shown in Fig. 4.25). The efficiency has not reach 100% because the step phasemask design is an estimation of perfect blazed grating. Also, the experimental efficiency will not reach the theoretical limit because the fs laser will induce slightly uneven index change on the structure. Figure 4.25 is still an essential reference which enables us to determine and tune the refractive index change induced by laser with efficiency measurements later.

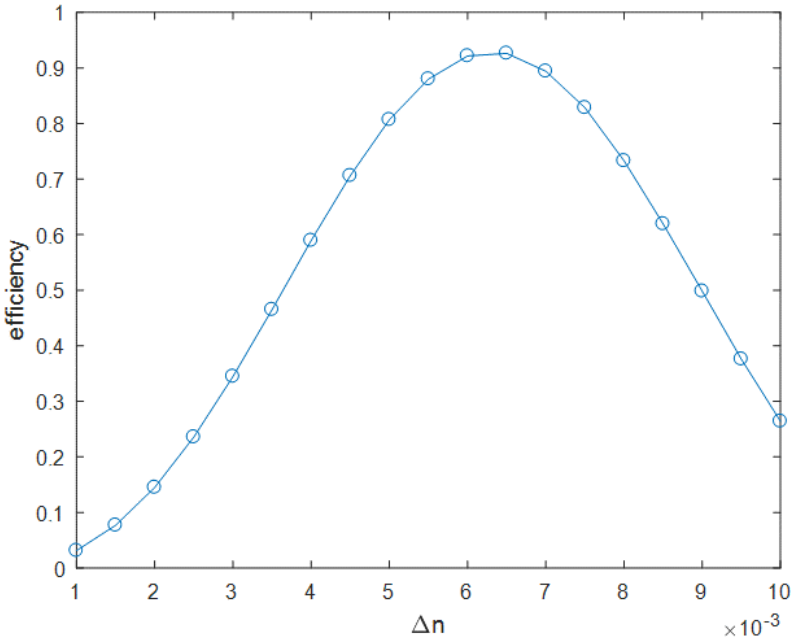


FIGURE 4.25: Efficiency simulation of 10-layer 5° grating with different refractive index change. Total thickness of grating is kept at 100 $\mu$m and grating width is 1 mm. Plane wave input of diameter size 0.3 mm is assumed.

### 4.2.2 Gaussian Beam Writing

#### 4.2.2.1 Writing in Silica

With the optimised writing condition in Fig. 4.12, we wrote a 10-layer 5-degree grating which has a 10 $\mu$m thickness between each layer. We found irregular damage on the grating. According to previous tests, damage is normally caused by a tight structure and thus high stress or high writing power. However, in that case, the damage should build up regularly. Therefore, in our case, the damage may also be caused by the polarisation state of our laser.

To investigate how the polarisation state affects the writing area, we then did some test writings with the beam polarised parallel and perpendicular to the scanning direction. Figure 4.26 shows the typical damage (shaded area) caused by these two polarisations.

For the same writing power and pulse density, we found the two polarisation states present different damage patterns. With the parallel polarisation state, silica is easier to be damaged. To lower the risk of damaging, we then wrote some three-zone testing gratings with the perpendicular polarisation state to find suitable writing conditions.

As a relatively small 10 $\mu$m gap between each layer can easily lead to damage; a 10-layer grating was written but found to be damaged because of the stress

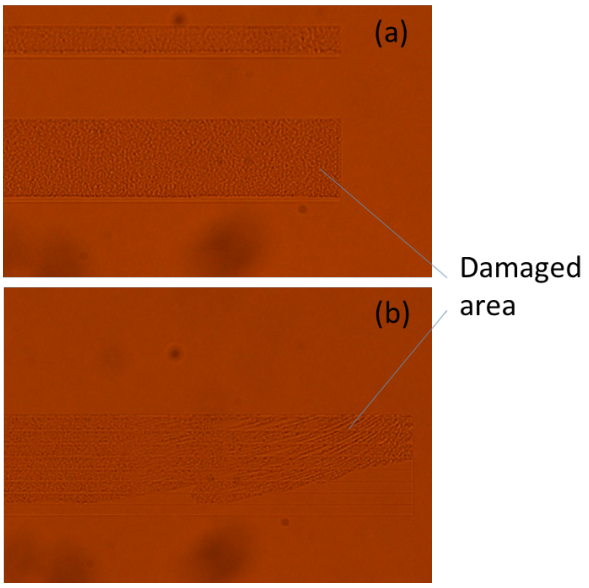


FIGURE 4.26: Microscope images of damage patterns induced by different polarisation states of the second harmonic laser beam, when polarised (a) parallel and (b) perpendicular to the direction of writing.

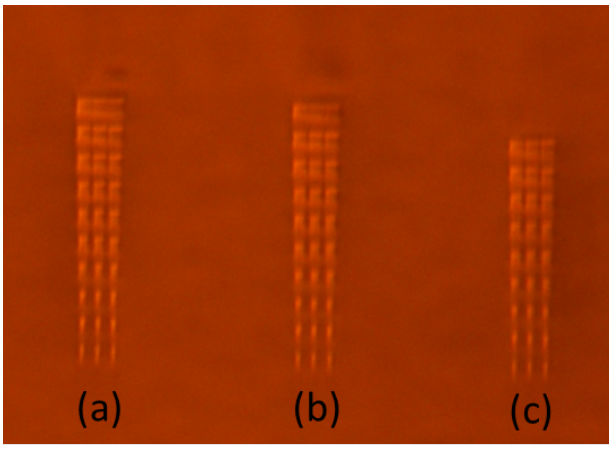


FIGURE 4.27: Microscope images of improved and smooth three-zone 10-layer grating cross-section, without damage. Pulse density is (a) 40000, (b) 30000, and (c) 30000 pulses/mm. Writing order from bottom to top, left to right.

accumulation. To release the stress, a grating was then written inversely (starting from the top layer to the bottom layer), results shown in Fig. 4.27.

With an inverse writing order, which is writing from the thinner top layer to the wider base layer of the grating (bottom to top in the figure), a clear and undamaged cross-section has been achieved with the same parameters as the former writing direction. Also, I found the widest base layer of the grating has only a small gap between each adjacent zone, and thus has less contribution to grating's diffraction effect compared to the other layers. However, this layer will build up the most stress on the structure and takes the most time to write. Therefore, I removed the bottom layer (from Fig. 4.27(b) to Fig. 4.27c).

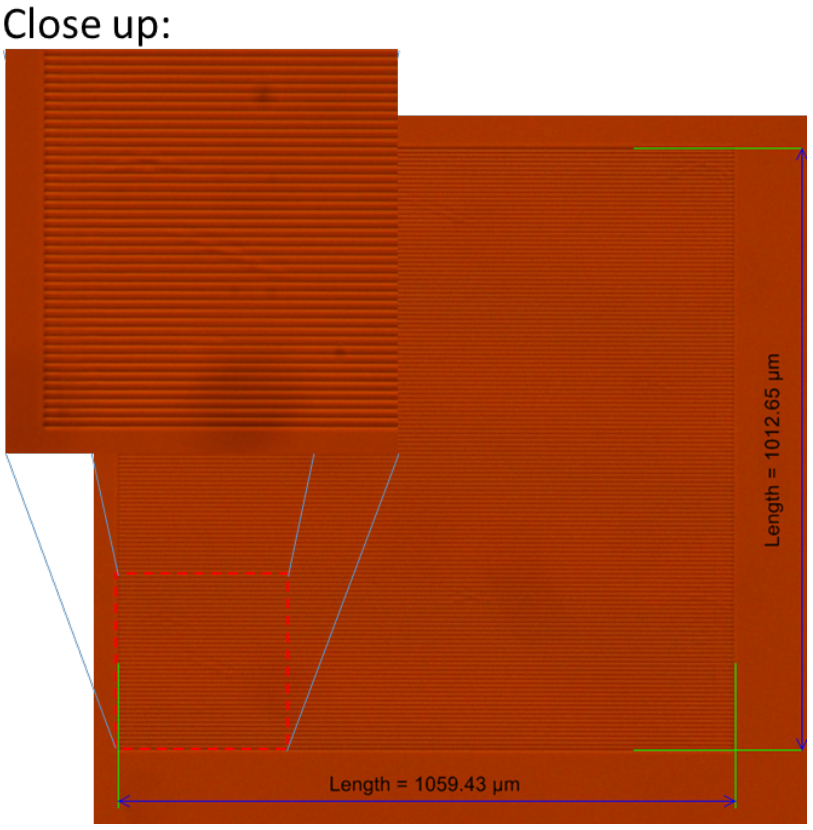


FIGURE 4.28: Microscope image of 10 layer 5 degree grating (1×1×0.1mm). Parameters: 75% of iris transmission, $P_w$ = 20.2 mW, $P_{w0}$ = 12.4 mW, $D$ = 30000 pulses/mm, $v$ = 5 mm/s, writing with perpendicular polarization state.

With the writing parameters of Fig. 4.27(c), we wrote a 5° 10-layer (1×1×0.1 mm) grating (with base layer removed, as shown in Fig. 4.28). The longer length in the writing direction is caused by the acceleration and deceleration margins during writing. With the new inverse writing order, the grating is now clear and has no obvious damage on it. The grating is then characterised with Fig. 2.14 to find the efficiency.

The results shows that inscribing with the parallel polarisation state, the efficiency is 22% at first order, which is higher than for the perpendicular polarisation state, 14%. A 22% efficiency corresponds to a $\Delta n$ of $2.5\times10^{-3}$ according to the simulation result in Fig. 4.25. Compared to the $\Delta n$ calculated from the MFD of straight waveguides in section 3.1 ($\Delta n$=$7\times10^{-4}$ to $6\times10^{-3}$), $2.5\times10^{-3}$ of $\Delta n$ corresponds to the average level.

#### 4.2.2.2 Writing in Lead Silicate Glass

SF57 lead silicate glass is a kind of soft glass which has a higher refractive index (1.86) than silica. Our SF57 sample has a diameter of 3 cm and thickness of 1.5 mm. Compared to pure silica, lead silicate glass has the potential to experience a higher

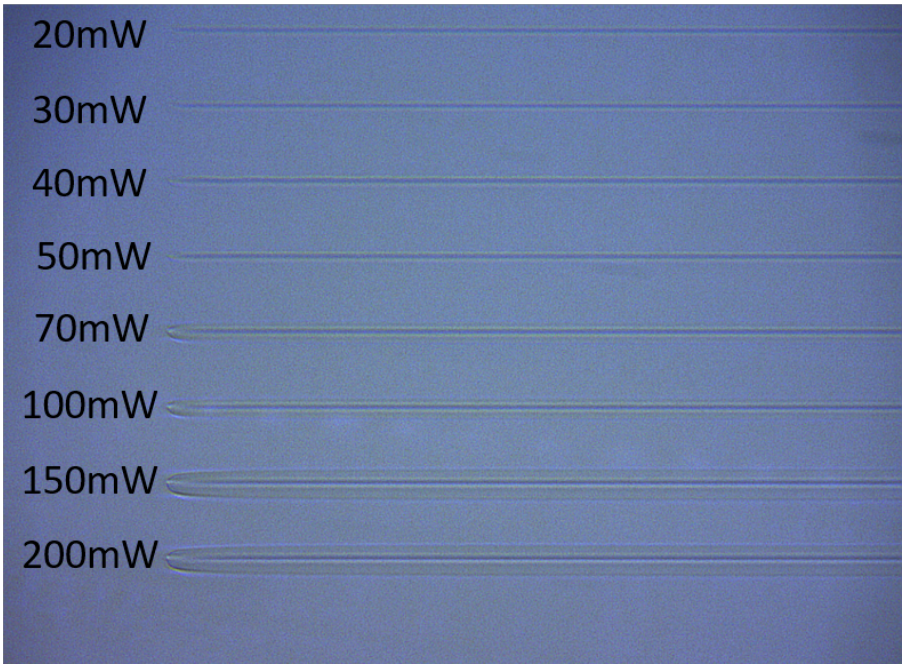


FIGURE 4.29: Top view of single scanlines inscribed in lead silicate with different writing power ($P$ = 20 to 200 mW). Pulse density and writing speed are fixed to 40000 pulses/mm and 5 mm/s, respectively.

refractive index change under modification and thus allow us to fabricate higher diffraction efficiency devices. We will investigate the waveguides written inside lead silicate glass to find out the index change and cross-section properties.

With single scan line testing, we found SF57 has a much wider non-damaging writing power range than silica. Figure 4.29 shows the single scan with different writing powers. Unlike silica, even with very high writing power (200 mW), the structure still seems smooth. Moreover, with powers greater than 70 mW, the thermal effect becomes very strong and easy to observe. With previous writing experience in silica, higher power may lead to a greater laser induced index change.

In order to investigate the cross section profiles of written structures, we cut our sample to a similar shape and size to our silica samples and with a polished facet, we are able to observe the shape of these test waveguide cross sections.

Fig. 4.30 shows the cross section of the waveguides written in SF57. With increasing pulse density, the thickness of the waveguide increases rapidly. However, for 110 mW writing power, with a density of 200000 pulses/mm, the shape of the waveguide starts to become irregular. The middle part of the waveguide is expanded due to the heat accumulation effect with the intense pulse energy which thus causes thermal distortion of the waveguide structure.

With a writing power of 120 mW, thermal effects and waveguide distortion become significant at a lower pulse density threshold of $\sim$100,000 pulses/mm. Also, by

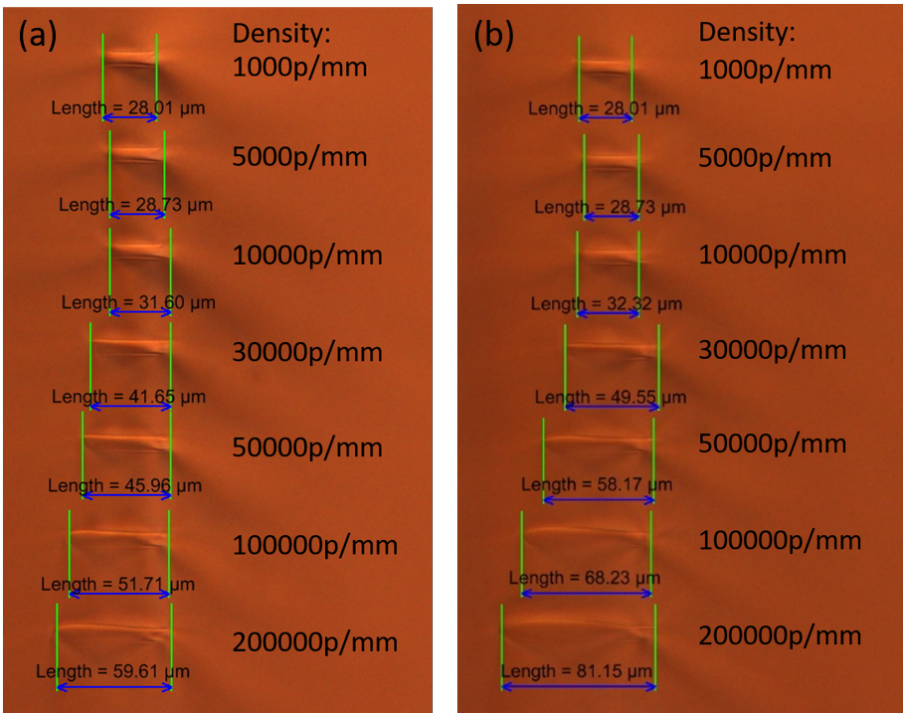


FIGURE 4.30: Microscope image of waveguide cross sections in SF57 lead silicate glass with writing powers of (a) 110 mW and (b) 120 mW, at different pulse densities.

further increasing power, we noticed that with the thermal effect, the thickness of the waveguide structure will reach a plateau at some point even if we keep increasing the writing power (see Fig. 4.31). This limits the structure thickness in terms of writing power.

Figure 4.31 gives a summary of the test waveguide heights for different writing powers and pulse density. The structure heights increase approximately linearly with power, for the different density curves. However, at the power of ∼150 mW, the curves plateau because of the thermal effect.

Next, we tested several parameters for writing thicker gratings in SF57. To avoid the thermal effect, we chose a lower writing density when increasing power. Besides, this also allows us to increase the writing speed. Table 4.2.2.2 shows some comparisons of the results.

Gratings A and B have the same writing condition, but Grating B has one more layer which contributes to 4% efficiency improvement. Gratings B and C have the same layer and total thickness but different writing conditions. However, the similar final efficiency indicates that the thickness is a more important parameter for diffractive grating design. Grating D is a 20-layer grating which has the thickest structure among all gratings. However, the strong stress caused a severe crack on the sample which can be attributed to the limitation of material strength.

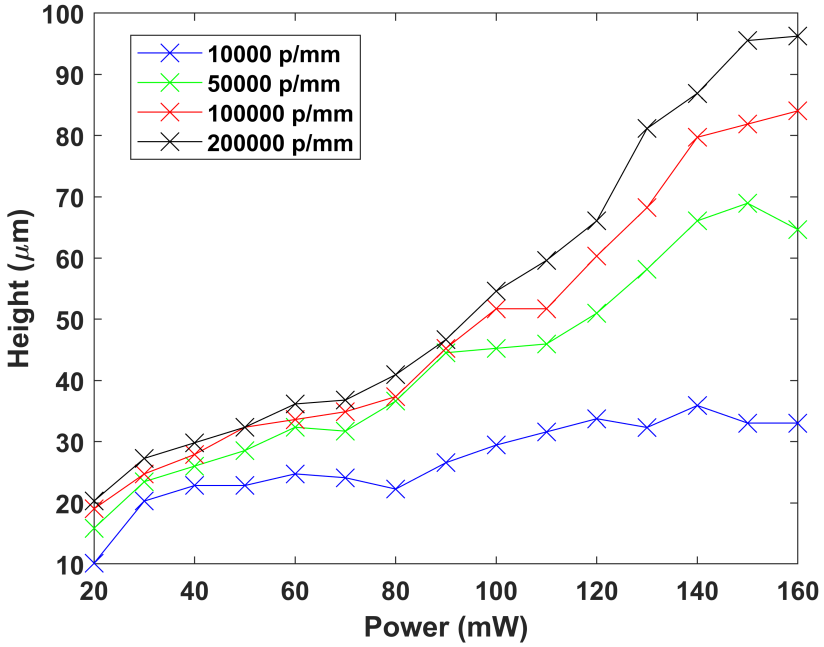


FIGURE 4.31: Waveguide height in SF57 vs writing power for different pulse density.

TABLE 4.2: Summary of gratings written in SF57 lead silicate substrate.

| Grating | Power(mW) | Density(pulses/mm) | Layers | Efficiency | $\Delta n$ |
|---|---|---|---|---|---|
| A | 130 | 50000 | 9 | 52% | $7.1\times10^{-4}$ |
| B | 130 | 50000 | 10 | 56% | $6.9\times10^{-4}$ |
| C | 150 | 30000 | 10 | 57% | $6.9\times10^{-4}$ |
| D | 140 | 10000 | 20 | - | - |

Because of the thermal effect, we cannot further increase the layer thickness by increasing power and pulse density. There are some measures to solve this limitation, for example we can narrow the iris before the objective, which will lengthen the Rayleigh range of the beam thus increasing the height of the written structure. Furthermore, since we have experience in Bessel beam writing in silica substrates, we will investigate the Bessel beam writing in lead silicate glass for creating taller structures. On the other hand, to avoid exceeding the limitations of material strength, we will design more gratings with a layer number between 10-20 and total thickness between 580-700 $\mu$m to find an optimized combination of writing parameters.

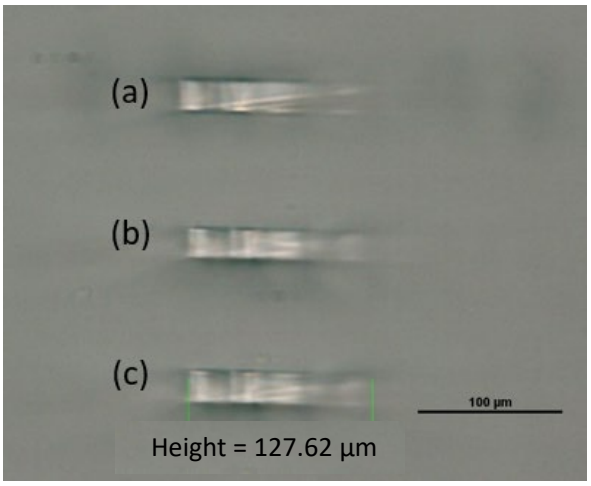


FIGURE 4.32: Cross sections of Bessel beam written waveguide with different scanning methods: (a) standard multiscan, (b) half-scan with 1600 $\mu$m major step and (c) half-scan with 800 $\mu$m major step. Writing beam direction is left to right.

### 4.2.3 Bessel Beam Writing

Similar to Fresnel lens writing, although the Gaussian beam can be used to write a large number of layers and thus achieve high diffraction efficiency, the long writing time is still problematic when inscribing large devices. The Bessel beam writing depth is >4 times longer than that of the Gaussian beam which reduces writing time for tall structures.

However, at a high power and density (see waveguide testing in 4.14(d) with power of 160 mW and density of 200,000 pulses/mm), we noticed an uneven thickness at the edge of waveguide cross section. According to the figure, the waveguide depth is longer at the bottom and shorter at the top. This is because of the stress of material changes during the writing process as discussed in section 3.2. To fix this problem, we altered the laser scanning method from multiscan to halfscan.

The waveguide in Fig. 4.32(a) is written with the standard scanning method, and we can observe the uneven depth distribution. The waveguides in Fig. 4.32(b) and (c) are written with the 'half-scan' method which produces more even structures. Moreover, as the waveguide in Fig. 4.32(b) has a larger major step (1600 $\mu$m) than the waveguide in (c) (800 $\mu$m), it has a more uniform cross-section. In later characterisation, we found that the 'halfscan' method produces a 7% improvement of single layer grating diffraction efficiency compared to the standard multi-scan method.

In order to calibrate the index change produced by Bessel beam writing, we wrote several single-layer gratings with different parameters. Figure 4.33 shows the results, when characterised with light from a HeNe laser source with two different polarisation states. The direction of the polarisation state is relative to the direction of the grating.

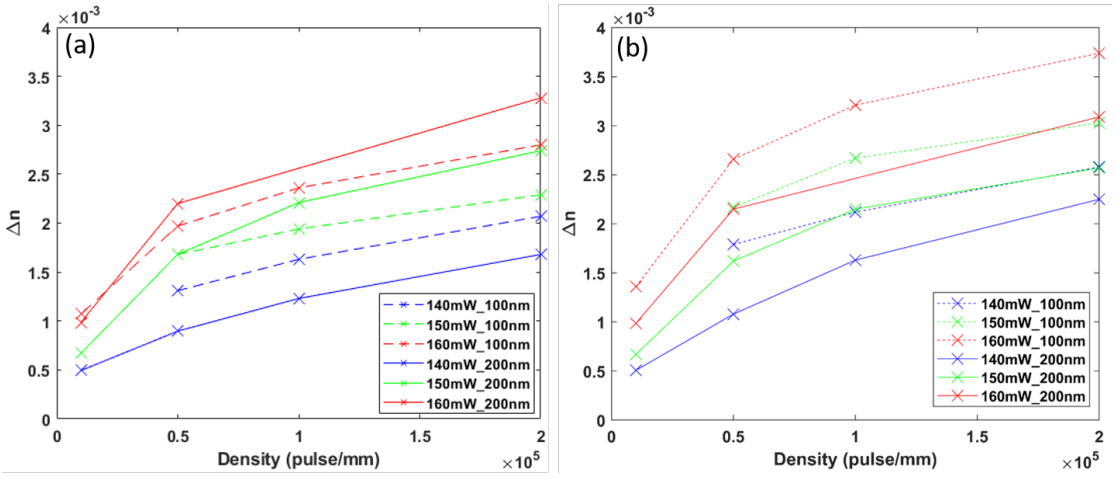


FIGURE 4.33: Single layer grating testing with different laser writing power and scan-line separation for (a) perpendicular and (b) parallel polarisation state writing beam.

All the gratings are written with the 'halfscan' method with a major step of 1600 nm. The main writing parameters we modified are power, pulse density and scanline separation (also termed the minor step in the halfscan method). From the results, we found that we are able to achieve $\Delta n$ ranging from $5\times10^{-4}$ to $3.8\times10^{-3}$ by modifying the laser writing parameters. As for multi-layer structures like the gratings and FZPs, matching the $\Delta n$ for different layers is critical for optimising the total efficiency, and we can use Fig. 4.33 as a $\Delta n$ calibration reference for future design.

## 4.3 Conclusions

In this chapter, the design and propagation simulation of the Fresnel zone plate were investigated. According to simulations, the diffractive FZP shows anomalous dispersion; and up to 85% and 95% diffraction efficiency can be achieved when focusing a plane wave and Gaussian beam input, respectively. For the experimental fabrication, a Bessel beam inscribed waveguide can achieve a modification height of $\sim$100 $\mu$m, which is 5 times greater than that of Gaussian beam writing. Then, through experimental characterisation, the Bessel beam written FZPs were confirmed to show anomalous dispersion. In terms of imaging, the FZPs were able to resolve down to 200 $\mu$m spaced array lines with clarity. For multi-layer FZPs, we achieved a 59% diffraction efficiency with a 3-layer FZP. In the grating writing section, 57% diffraction efficiency was achieved in SF57 lead silicate glass with Gaussian beam writing. For Bessel beam writing, by measuring the diffraction efficiency, the index change has been estimated and characterised for different laser powers and pulse densities.

# Chapter 5

# Scattering Media Based Devices

Conventional spectrometers separate light into a spectrum using a diffractive or refractive element, where the spatial separation of spectral components increases linearly with the distance of propagation. The main purpose of the work in this chapter is to implement a more compact spectrometer based on exploiting the benefits of a scattering medium, which can be engineered using laser direct writing. A femtosecond laser pulse, tightly focused in silica glass, induces a spherical shock wave, which disrupts the material creating a nanovoid without any collateral damage. Due to the high refractive index contrast between the void and substrate, strong optical scattering can be achieved.

## 5.1 Scattering chip design and fabrication

Scattering chips were written with the fs laser with the setup in Fig. 2.1 with 515 nm SHG beam and oil-immersion objective (NA 1.25). High purity fused silica glasses (UVFS C7980 0F) with ultra-low thermal expansion coefficient ($0.57\times10^{-6}K^{-1}$) and OH content of 800-1000 ppm (shown in Fig. 5.1(a)) were used as substrates.

For generating the random scattering matrix patterns, we first design a 500 $\times$ 500 dot regularly spaced matrix in MATLAB (top image in 5.2(a)). The dot spacing of $p_x = p_y = 2$ $\mu$m produces a 1 $\times$ 1 mm matrix. Next, we add a randomized offset $\Delta x$ or $\Delta y$ of up to $\pm$600 nm for each dot in the $x$ or $y$ direction (shown in 5.2(a)). To speed up writing, instead of randomizing both the $x$ and $y$ dot coordinates, we do cross randomized writing, so each layer's dots only have one axis randomization. For a 1 $\times$ 1 mm scattering medium, this reduces writing time from 15 min to 2.4 min per layer.

The scattering matrix is written embedded 20 $\mu$m below the sample surface with a pulse energy of 220 nJ. To increase the fraction of scattered light and facilitate multiple

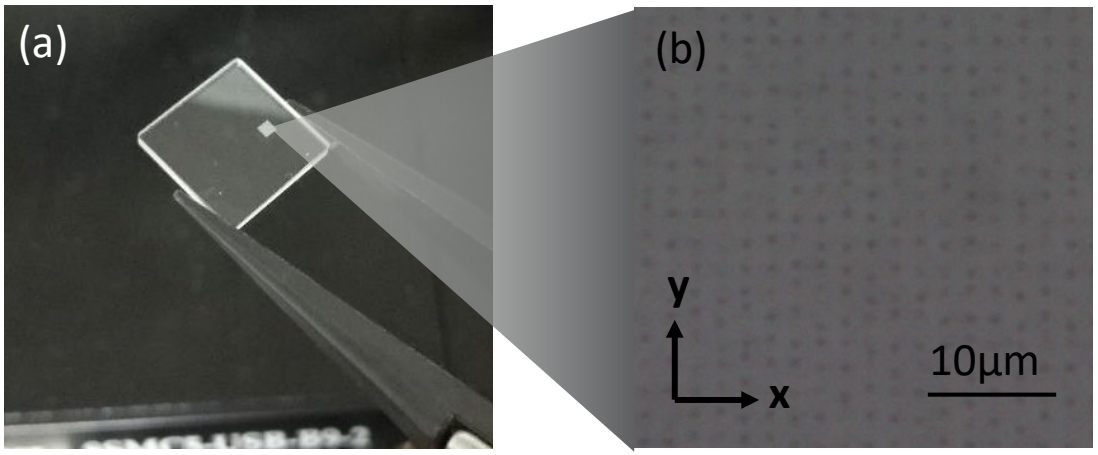


FIGURE 5.1: (a) Photo of 10×10×1 mm silica substrate and 1×1 mm scattering pattern. (b) Microscope image of one layer of a $y$-axis randomized scattering pattern.

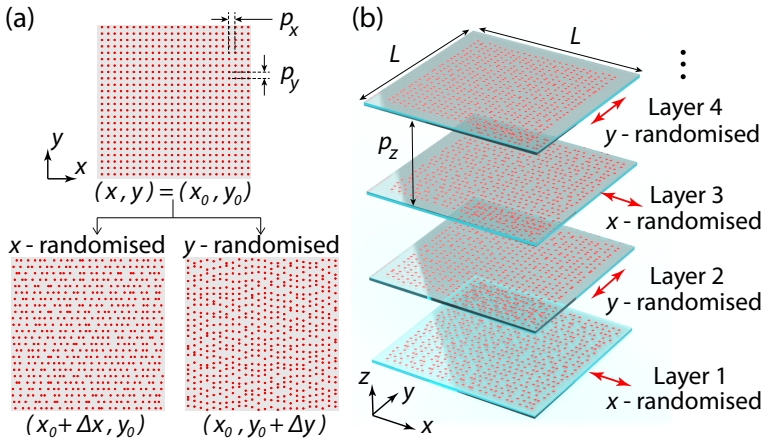


FIGURE 5.2: (a) Design of scattering layers: a regular grid of scattering voids (red dots) is randomised in either the $x$ or $y$ direction, by adding random offsets $\Delta x$ or $\Delta y$ (in the range -0.6 – 0.6 $\mu$m) to the $x$ or $y$ coordinates, respectively. (b) Arrangement of layers within scattering chip, alternating between $x$ and $y$ randomisations (not to scale). Mean transverse pitch $p_x = p_y = 2$ $\mu$m; layer spacing $p_z = 5$ $\mu$m.

backwards and forward passes, we write multilayer random dot patterns spaced 5 $\mu$m apart, where the direction of randomisation alternates between $x$ and $y$ for adjacent layers. Each individual dot is a void formed by a microexplosion induced by a single fs pulse, which can achieve up to 0.45 of refractive index change Glezer et al. (1996).

## 5.2 Scatterer simulation

Based on the scatterer size, there are two regimes of scattering: Mie scattering and Rayleigh scattering. Our scattering chips are working at the Mie scattering range. Based on the simulations by Schafer Schäfer (2011) for the near field solution of sphere structures, we have modelled and studied the effect of scatterer size on scattering directionality and magnitude. This is important as the scattering spectrometer

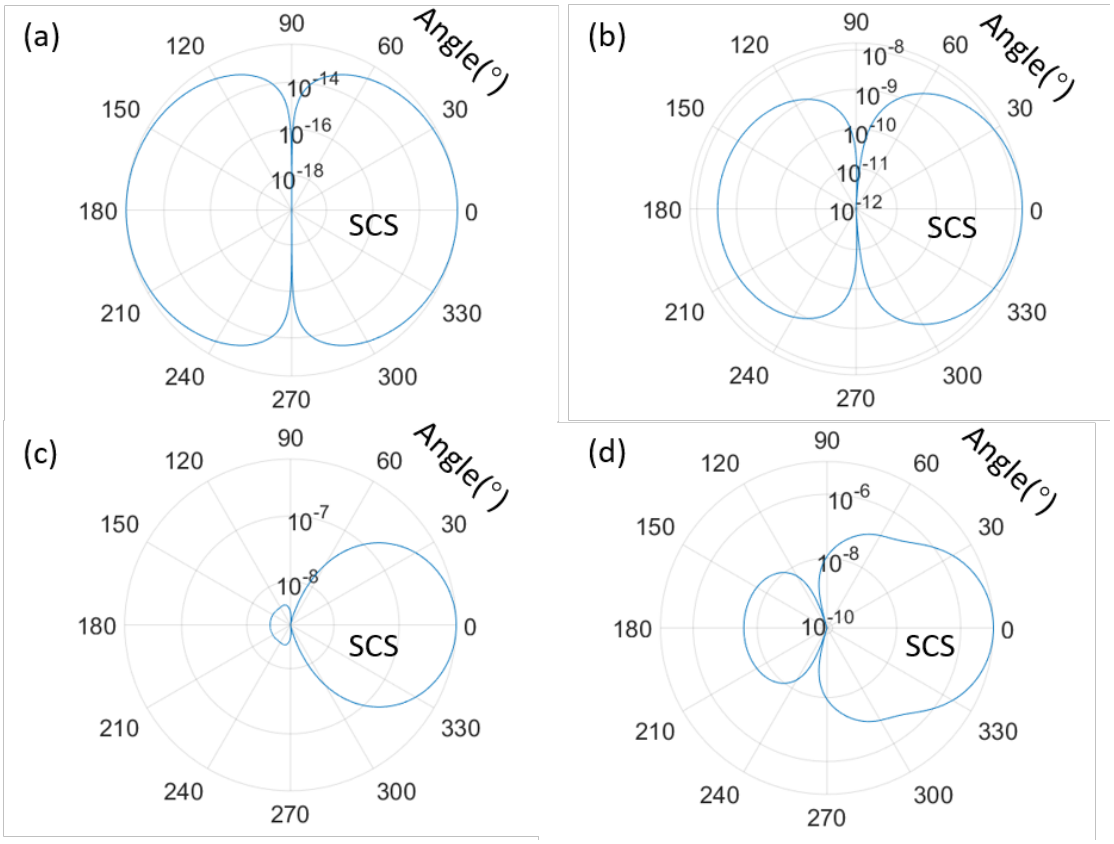


FIGURE 5.3: Polar plot of the differential scattering cross section (SCS) with the scatterer diameter size of (a) 50 nm, (b) 300 nm, (c) 600 nm and (d) 1000 nm.

resolution is highly dependent on the interference between the chip layers, since the greater the back scattering, the more chances of multi-pass interference and thus finer spectrometer resolution we can achieve.

We assume the spherical void scatterer has an inner refractive index of 1.0 surrounding by outer glass medium with 1.45 refractive index. The vacuum wavelength for the simulation is chosen to 1000 nm. Figure 5.3 shows the polar plot of the differential scattering cross section (SCS) vs the scattering angle for scatterer diameters ranging from 50 nm to 1000 nm. An angle of 0° represents the forward direction while 180° is the backward scattering direction. Calculating the ratio between the forward and backward scattering SCS was calculated for each scatterer diameter, we obtain $S_{\text{coeff}}$ = 1, 5, 170 and 400 for scatterer diameters of 50 nm, 300 nm, 600 nm and 1000 nm, respectively. With increasing scatterer diameter, the ratio between the forward and backward scattering increases rapidly. As the fs laser induced scatterer size is normally between 100 nm to 1 $\mu$m, the single sphere scatterer simulation offers insight and guidance for us to optimize the scattering chip.

However, in a multi-scatterer system, the complexity of the simulation would be greatly increased. For this reason, in experiments, we always estimate the scattering properties by the scattering efficiency test: passing the laser light through the

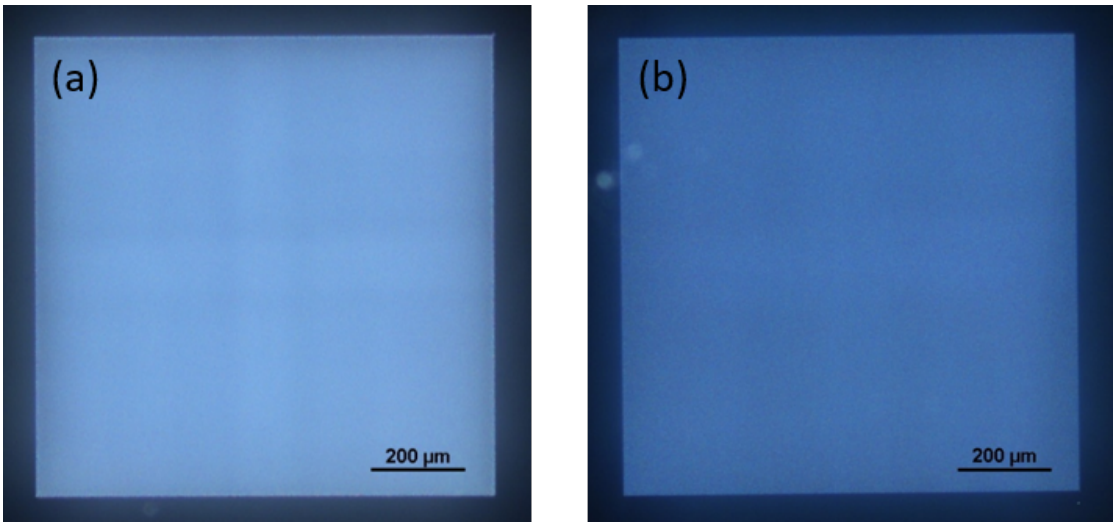


FIGURE 5.4: Dark field ×5 microscope images of two scattering chips fabricated with pulse energies of (a) 800 nJ and (b) 200 nJ. Images were captured with the same reflection illumination and exposure time. The scattering efficiency is (a) 70% and (b) 30%.

scattering chip and calculating the ratio between the scattered power and the incident power. Indeed, the laser writing parameters strongly affect the scattering properties to an extent which can be observed by microscope imaging. Fig. 5.4 shows an example of a chip scattering efficiency comparison under microscope view. Both chips have a 20-layer alternately randomized structure, with the chip in Fig 5.4(a) written with a pulse energy of ∼800 nJ while the chip in (b) is written with ∼200 nJ. The images were captured in dark-field mode, so light from the microscope illumination source which is scattered is captured by the objective. According to scattering efficiency testing results, the chips in Fig 5.4(a) and (b) have scattering efficiencies of 70% and 30%, respectively, for 1100 nm wavelength light. With the same exposure time, we can see the different scattering intensity between Fig 5.4 (a) and (b).

## 5.3 Working mechanism

The scattering chip is characterised with the setup in Fig. 2.15, after passing through the scattering chip, the properties of the light (e.g. wavelength spectrum) are essentially encoded within the speckle pattern. By analysing the speckle pattern, we can then reconstruct these properties of the light. In this section, the reconstruction algorithm for the wavelength will be discussed in two parts: (i) for a wavemeter which measures the specific wavelength of monochromatic light, and (ii) for a spectrometer which measures a spectrum which may contain multiple wavelength components.

### 5.3.1 Wavemeter

Before analysis, a calibration group measurement was done to establish a connection between the wavelengths and the speckle patterns. $N$ speckle patterns were captured corresponding to $N$ wavelengths. Here we use $C(M(x,y),\lambda)$ to represent the calibration matrix, where $M(x,y)$ represents the measured intensity of each pixel of the CMOS sensor. In our case, the size of $M$ is $1280 \times 1024$.

Then in the test group, we have the speckle patterns with unknown wavelengths, $T(M(x,y),r)$, where $r$ represents the number of speckle patterns input. Eq. 5.1 will give the correlation *Corr* between each test speckle pattern and each calibration speckle pattern. By analysing the correlation coefficient, we can then find the most related wavelength. Notice the $M$ in Eq. 5.1 is the 1,310,720 (or $1280 \times 1024$) vectorised pixel elements, and the calibration matrix is transposed to process the matrix multiplication.

$$Corr = C(\lambda, M) * T(M, r) \tag{5.1}$$

### 5.3.2 Spectrometer

For an input beam comprising multiple wavelengths, after passing through the scattering chip, the light produces a speckle pattern that is a direct linear sum of the weighted speckle patterns of its components. If the constituent speckle patterns are sufficiently different, it is possible to distinguish the different wavelength components of the spectrum. Fig. 5.5(a) shows the measured and simulated speckle pattern of a 10-layer $x-y$ alternately randomised chip. Fig. 5.5 (b) is plotted in $k$ space and the visible hues (for speckles corresponding to different wavelengths) indicate that the speckle patterns are clearly visible and differentiable.

The recorded speckle pattern $M(x,y)$ can be modelled as a linear combination of the calibration patterns, $C(x,y,\lambda)$, weighted by the unknown spectrum, $S(\lambda)$, and an error term, $\epsilon$, to account for detection noise:

$$M(x,y) \quad = \quad \sum_{i=1}^{N} C(x,y,\lambda_i) S(\lambda_i) + \epsilon \tag{5.2}$$

where $N$ is the number of wavelengths distinguishable by the spectrometer. This linear set of equations can be written more succinctly in matrix equation as $M = CS + \epsilon$, where (as in the wavemeter section) $M$ is the column vector listing the 1,310,720 (or $1280 \times 1024$) vectorised pixel elements. Ideal noise-free measurements would enable us to calculate the spectrum $S$ by considering that $S = C^{-1}M$ and

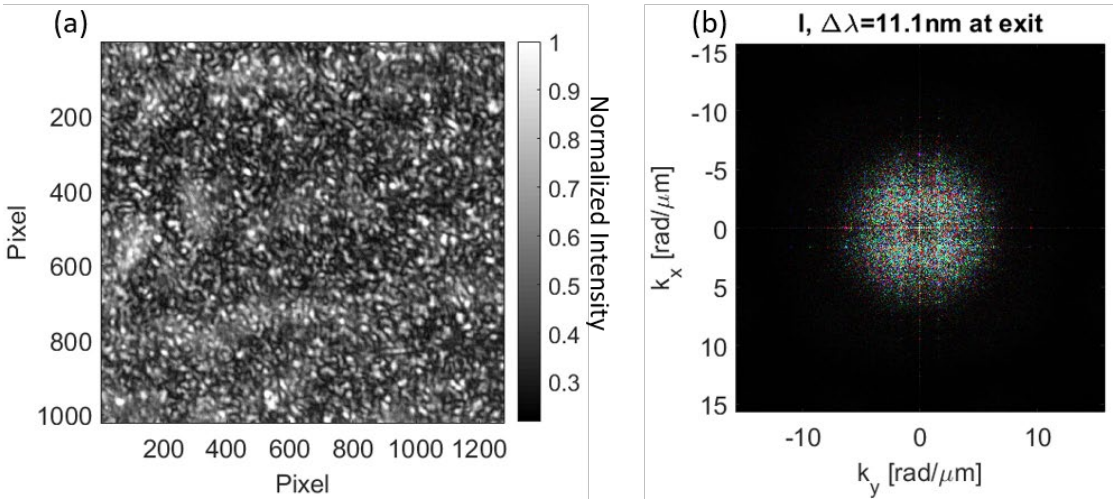


FIGURE 5.5: (a) Experimentally measured and (b) simulated (in $k$-space) speckle patterns, for 10-layer scattering chip alternately randomised in $x$ and $y$. The different hues in (b) correspond to speckles from different input wavelengths.

calculating the inverse from the singular value decomposition $C = U\Sigma V^\dagger$ as $C^{-1} = V\Sigma^{-1}U^\dagger$. Here, $U$ and $V$ are unitary matrices, $^\dagger$ denotes the complex transpose, $\Sigma$ is a diagonal matrix with the singular values, $\sigma_i$, of $C$, and $\Sigma^{-1}$ is a diagonal matrix with reciprocal values, $1/\sigma_i$. The singular values link combinations of wavelengths (columns of $V$) to measurable patterns (columns of $U$). Each singular value thus represents an independent link between the wavelengths and their effect on the measured speckle pattern. The link's contribution is proportional to the singular value.

However, in practice, the matrix $C$ may not be full-rank and division by near-zero $\sigma_i$ values would amplify any measurement error $\epsilon$ that may be present. Error amplification can be avoided by calculating the spectrum as $\hat{S} = C_r M \approx S$, using the Wiener filter $C_r = V\Sigma_r U^\dagger$, where diagonal matrix $\Sigma_r$ has elements

$$\Sigma_{r,ii} = \frac{\sigma_i}{\sigma_i^2 + |n/s|^2}, \tag{5.3}$$

and $n/s$ is an estimate of the noise-over-signal ratio to regularise the inversion. Although more accurate estimates of the spectrum $S$ may be obtained using non-linear methods, these tend to require resource-intensive iterative algorithms. The multiplication with the Wiener filter efficiently minimises the average value of $\|C\hat{S} - M\|^2$ in a single step algorithm.

It can be noted that large singular values are approximately inverted, while singular values below $|n/s|$ are suppressed. The number of independent components with values above the noise level gives an indication of the number of degrees of freedom that can be quantified, and thus the number of wavelengths that can be reliably

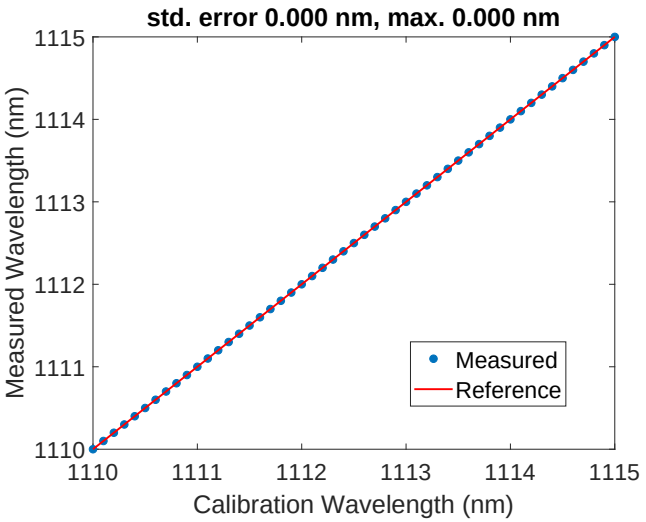


FIGURE 5.6: Wavelength reconstruction test. For each test, the wavelength is increased by 0.1 nm and the measured wavelength based on the speckle pattern analysis is plotted. Also shown is the true reference wavelength for each test.

distinguished by the scattering spectrometer. Here, the ratio $|n/s|$ was set to 0.01, corresponding to a conservative signal-to-noise ratio of 20 dB.

## 5.4 Experimental Results

### 5.4.1 Wavemeter

A set of speckle patterns was captured using parameters identical to those of the calibration set. The wavelengths were then recovered by processing the captured data with the spectrum reconstruction algorithm (Fig. 5.6). In a perfectly matched situation, the blue points should all sit on the red reference dash line. Here, we have perfectly reconstructed the wavelength with a calibration step of 0.1 nm.

In order to test the limits of the wavemeter system, speckle pattern images with a reduced number of pixels were tested. Fig. 5.7 plots the standard deviation (std.) of the reconstructed wavelength error against the number of used pixels.

The wavemeter can reconstruct the wavelength with no error up to a pixel number of 100 pixels, which means with 0.1 nm step of the calibration resolution, we only need to use 100 pixels (e.g. a 10 pixel $\times$ 10 pixel image) to perfectly reconstruct the wavelength. This would enable us to build a real time wavemeter system and process the data in a much shorter time than if using the full number of pixels. Moreover, since our system doesn't have a high requirement for the image detector, a cheap low-resolution CMOS sensor would be enough for achieving a high performance.

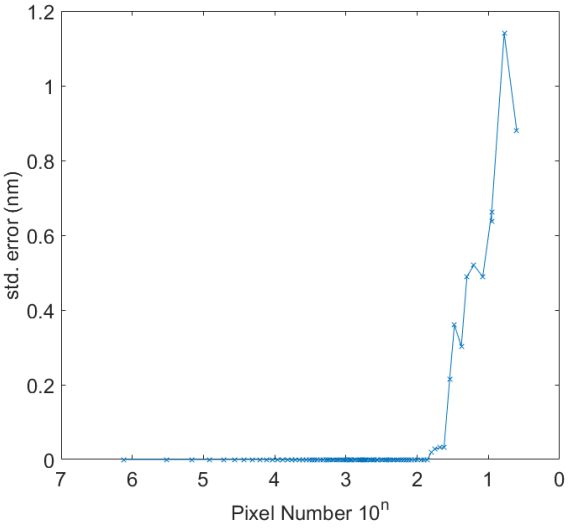


FIGURE 5.7: Standard deviation error of reconstructed wavelength when using speckle patterns with different numbers of pixels.

For even smaller size images, Figs. 5.8 and 5.9 plot the reduced size speckle images and corresponding wavelength reconstruction results. Even with 42 pixels, the wavemeter can still demonstrate a high performance with only 32 pm std. error.

### 5.4.2 Spectrometer

To evaluate the spectrometer performance, we mixed a few speckle patterns to create a probe wavelength array. By testing different spectral separations between these wavelength inputs and reconstructing the wavelengths of the mixed speckle pattern, the resolution of scattering spectrometer can be estimated. Fig. 5.10 shows the closest distinguishable probe wavelengths reconstructed with our algorithm. We obtained 0.2 nm resolution with 0.1 nm calibration wavelength step. The resolution can be further reduced by using finer tuning steps.

For the spectrum reconstruction test, we simulate arbitrary test spectra by applying an intensity modulation $I(N)$ to each speckle pattern $C(M(x,y),N)$ in the calibration group:

$$T(x,y) = \frac{\sum_{i=1}^{N} C(M(x,y),i) * I(i)}{N} \tag{5.4}$$

By averaging all the modulated images, we obtain a mixed speckle pattern $T(x,y)$. The reconstruction result is shown in Fig. 5.11, where the red line is the spectrum modulation function and the blue cross is the reconstructed spectrum. As can be seen, both spectra are reasonably reconstructed, but the gradually changing sinusoidal

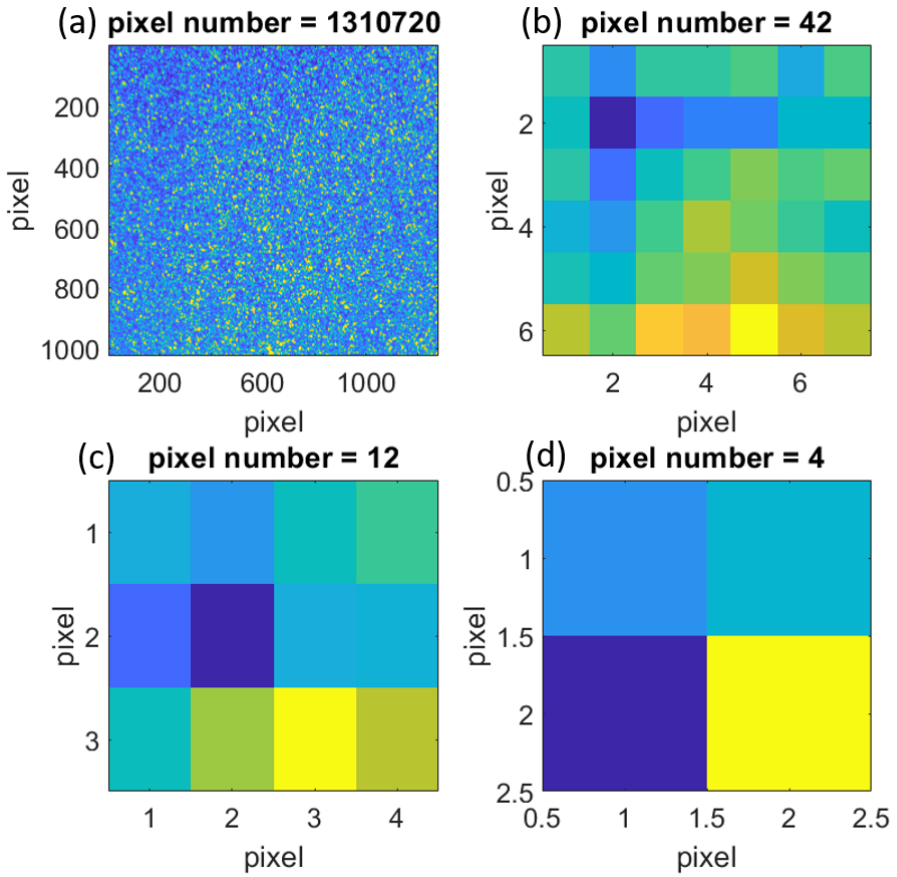


FIGURE 5.8: Speckle images with reduced number of pixels. The size of the image is (a) $1024 \times 1280$; (b) $6 \times 7$; (c) $3 \times 4$; (d) $2 \times 2$.

spectral modulation reconstruction is more faithful and shows roughly 4 times lower std. error than that of the more abrupt square wave modulation.

### 5.4.3 Stability

Stability is one of the most important properties that needs to be evaluated in order to achieve practical use of the spectrometer. Temperature dependence of the material refractive index and thermal expansion are the main factors influencing dispersion and thus the speckle pattern stability, assuming the scattering chip is already secured in a mechanically robust holder. Experimentally, the influence of the environment was evaluated by setting the TLS at a fixed wavelength and taking measurements over a 120 hour period (Fig. 5.12). The blue cross marker shows the reconstructed wavelength over time, the red dashed line shows the set wavelength of the laser source.

The standard deviation of the reconstructed wavelength was found to be 122 pm. It is important to note that the error did not increase with time, indicating the optical

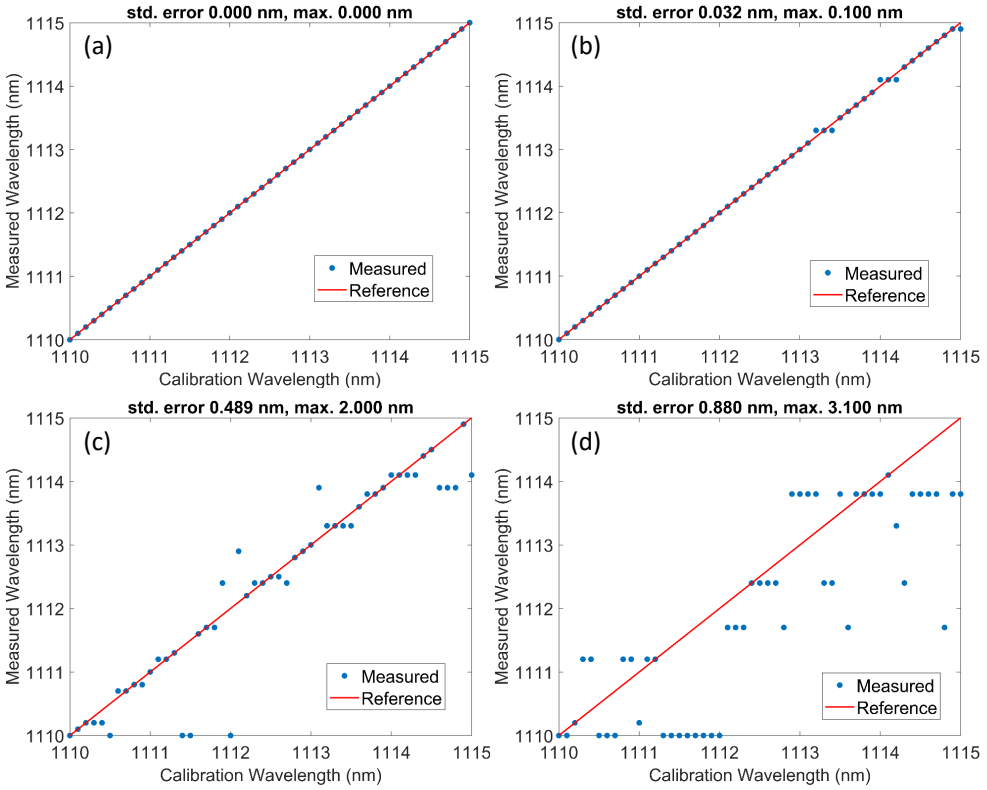


FIGURE 5.9: Wavelength reconstruction from speckle images with reduced number of pixels (corresponding to those in Fig. 5.8). The red line shows the reference wavelegth, and the blue shows the reconstructed wavelength from speckle pattern. The standard deviation (std) of reconstructed wavelength error and maximum error are shown.

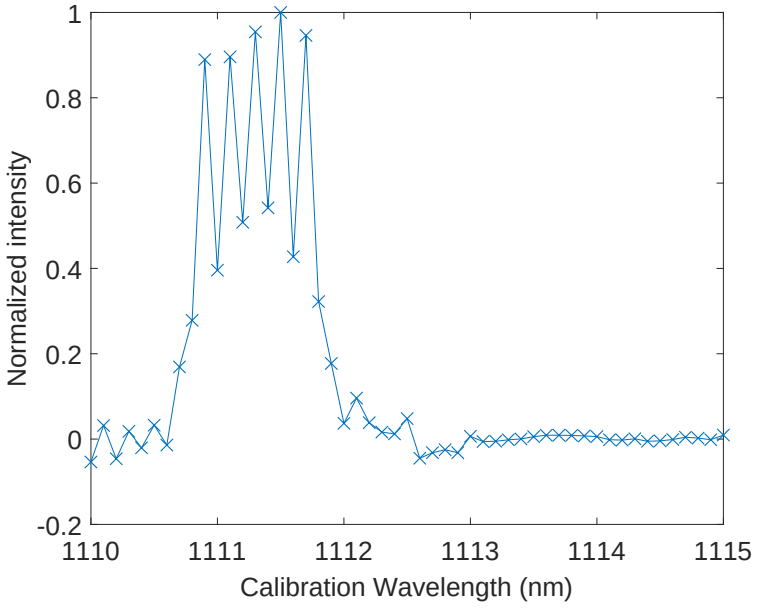


FIGURE 5.10: Wavelength reconstruction of test spectrum using reduced size speckle images.

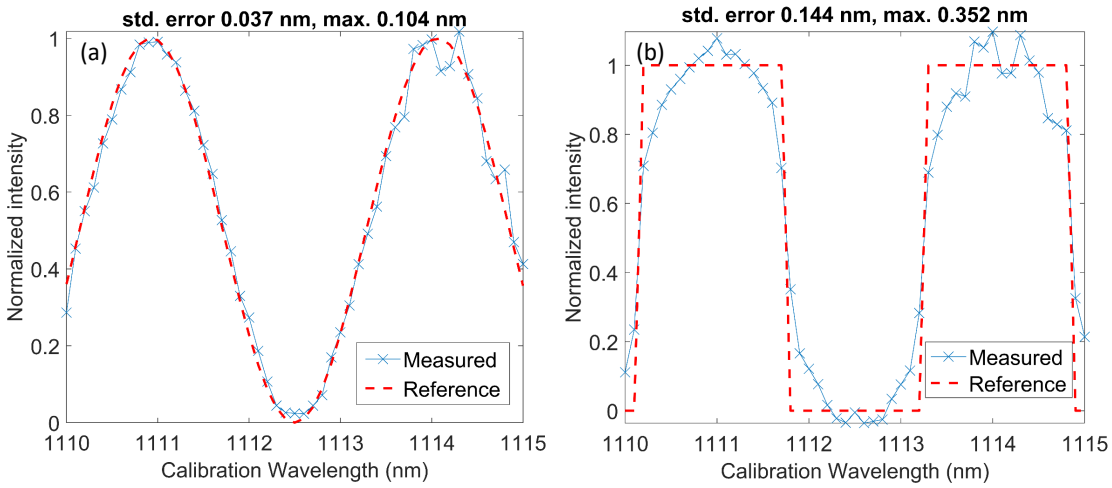


FIGURE 5.11: Spectrum measurement for (a) sinusoidal and (b) square spectra. Dashed line shows the reference spectrum, solid line shows the reconstructed spectrum.

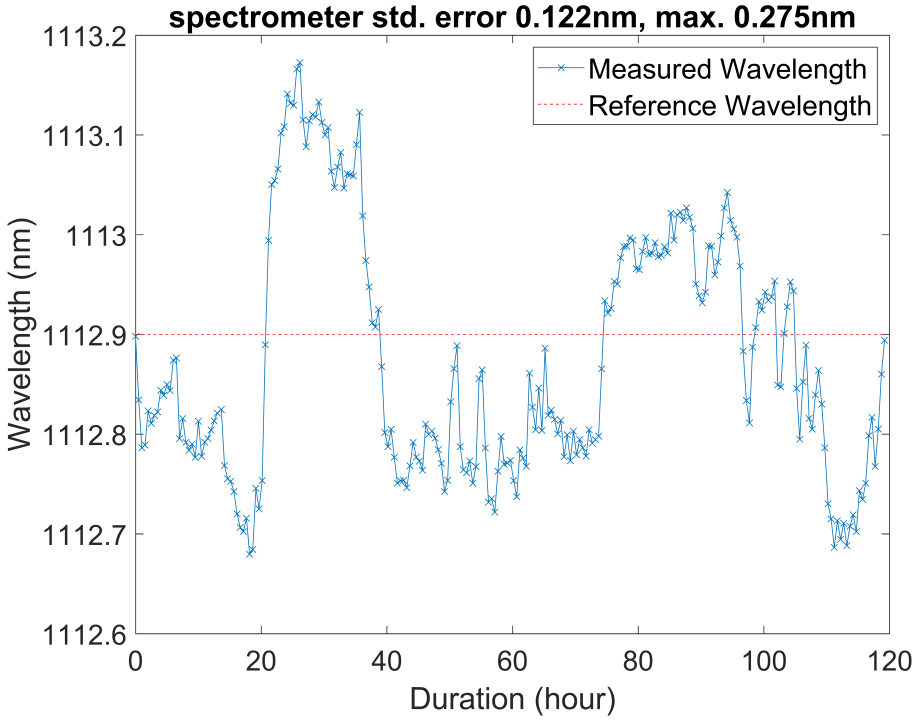


FIGURE 5.12: Experimental stability test over 120 hours. Blue cross markers show reconstructed wavelength every half hour and red dashed line shows real wavelength of the source. Standard deviation of reconstructed wavelengths is 122 pm, maximum error is 275 pm.

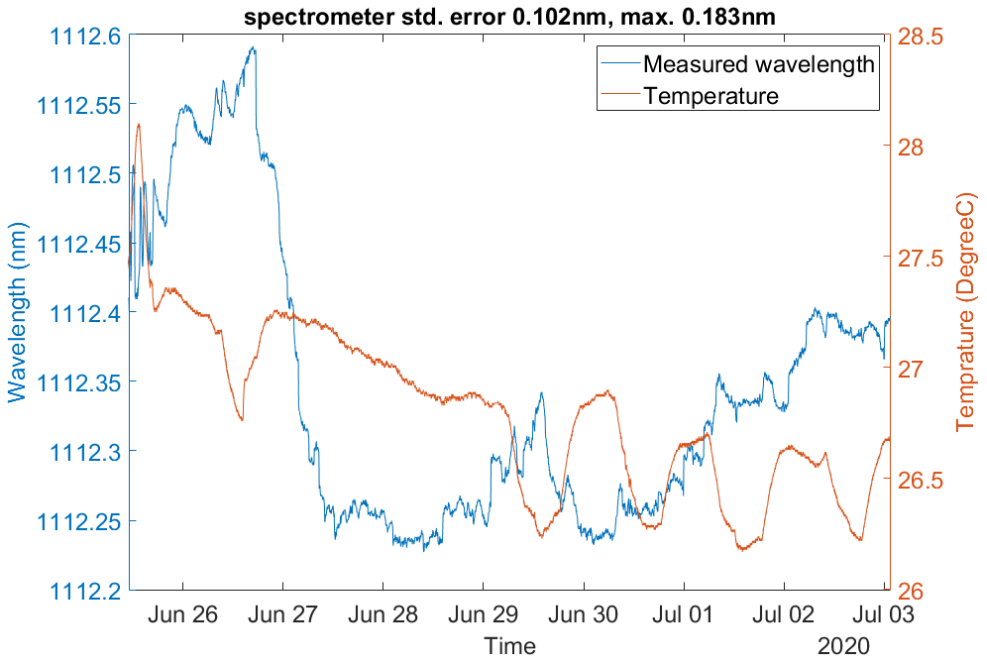


FIGURE 5.13: One week stability test showing reconstructed wavelength (blue) with temperature monitoring (red).

properties of the scattering chip do not diverge over the time and are repeatable. This indicates that a stable performance can be achieved, making a scattering spectrometer a viable solution for practical applications. The variation of the wavelengths is probably because of the temperature change and mechanical perturbations.

In order to investigate how temperature affects the reconstructed wavelengths, a further one-week stability test with temperature monitoring was conducted, as shown in Fig. 5.13. The blue curve shows the measured wavelength fluctuation and the red curve shows the temperature change. From the figure, the correlation between the wavelength and temperature change is not obvious. To study the behaviour further, principle component analysis (PCA) was applied to analysis the results.

PCA is an important tool for data analysis. By decomposing the principle components of a dataset (in our case, the set of speckle patterns in stability test $T(t, M)$, where $t$ is the number of speckle patterns, $M$ is the speckle pattern matrix), we can find the main characteristics among all speckle patterns.

Fig. 5.14 shows the correlation between temperature change and PC values for the tests over the 1 week duration. We found that temperature has the largest impact on the PC3. Fig. 5.15 plots the PC3 eigen value together with measured temperature.

Although the PC value before the green dash line is less related to the temperature change, after the green line, the graph shows a clear inverse relationship. For practical applications, such temperature induced variation can be compensated by integrating

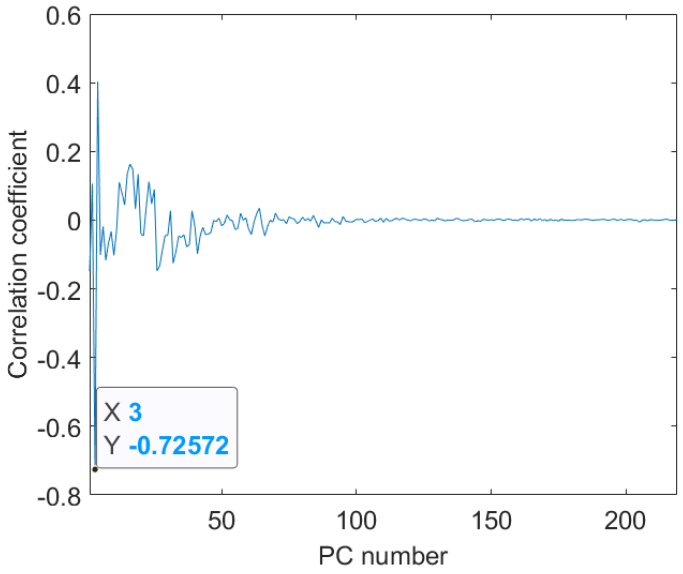


FIGURE 5.14: Correlation between temperature change and the PC values. $x$ axis is the number of PC value. Temperature has the largest impact on PC3.

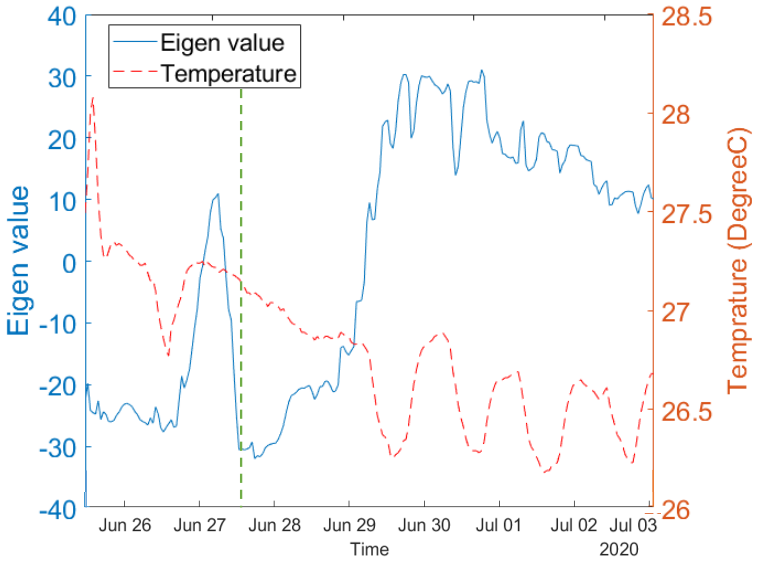


FIGURE 5.15: PC3 eigen value plot. $x$ axis is the number of the test data, recorded spaced equally over 1 week.

all critical components into a single package and introducing an active temperature control.

### 5.4.4 Interferometric Distance Measurement

Besides its application as a spectrometer, the scattering chip and its speckle patterns can also be applied in the field of interferometry. This section describes scattering chip

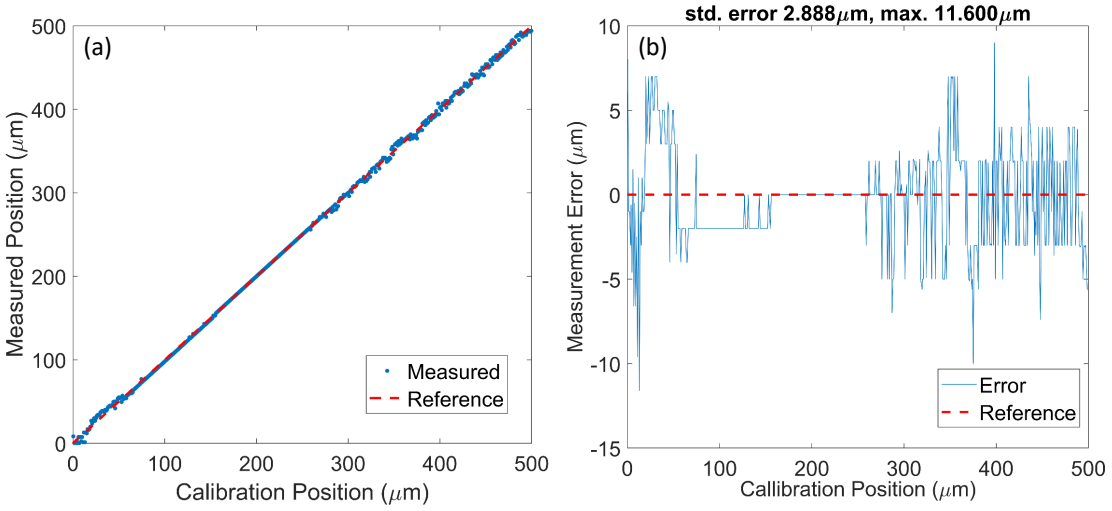


FIGURE 5.16: (a) Position reconstruction test over 500 $\mu$m range. The blue marker shows the reconstructed position with each captured speckle pattern in the test group. The red line shows the actual motor position. (b) The error at each measurement point, the red dashed line shows the zero error reference.

assisted white light interferometry (WLI) for measuring surface topography. The characterisation setup is shown in Fig. 2.16.

#### 5.4.4.1 Results

The characterisation setup is shown in Fig. 2.16. The range of the WLI setup was evaluated following a calibration of the scattering chip spectrometer by translation of the measurement mirror using the PZT to move from $z$=0 $\mu$m to 500 $\mu$m in 1 $\mu$m increments with a speckle pattern captured for each increment. A second set of data, to be used as measurement data, with an increment of 1 $\mu$m is then obtained and the calibration set is used to determine the $z$ position of each pattern. The plot in Fig. 5.16(a) shows the result of position reconstruction results of 500 test speckle images. The $x$ axis shows the test number of the captured speckle image data, and the blue points show the reconstructed position by the algorithm. Fig. 5.16(b) shows the error plot of each measurement point. Over the range of 500 $\mu$m, the reconstructed position has a std. error of 2.9 $\mu$m. Note that since the step-size of the PZT is 1 $\mu$m, the resolution could be further improved with finer PZT calibration steps.

We also found that the measurable position range could be limited by the coherence length of the source. The result in Fig. 5.16 is measured with a SLED with 25 nm bandwidth centered at 830 nm. For an 850 nm SLED with 50 nm bandwidth, we obtained a measurable range over 220 $\mu$m. Beyond 220 $\mu$m, the signal strength decreases and noise increases reducing our ability to determine the surface position. Fig. 5.17 shows the 3D plot of weight coefficient $S$ (see Eq. 5.2) of the system range. The signal becomes weak after 220 $\mu$m, which means the features of the speckle

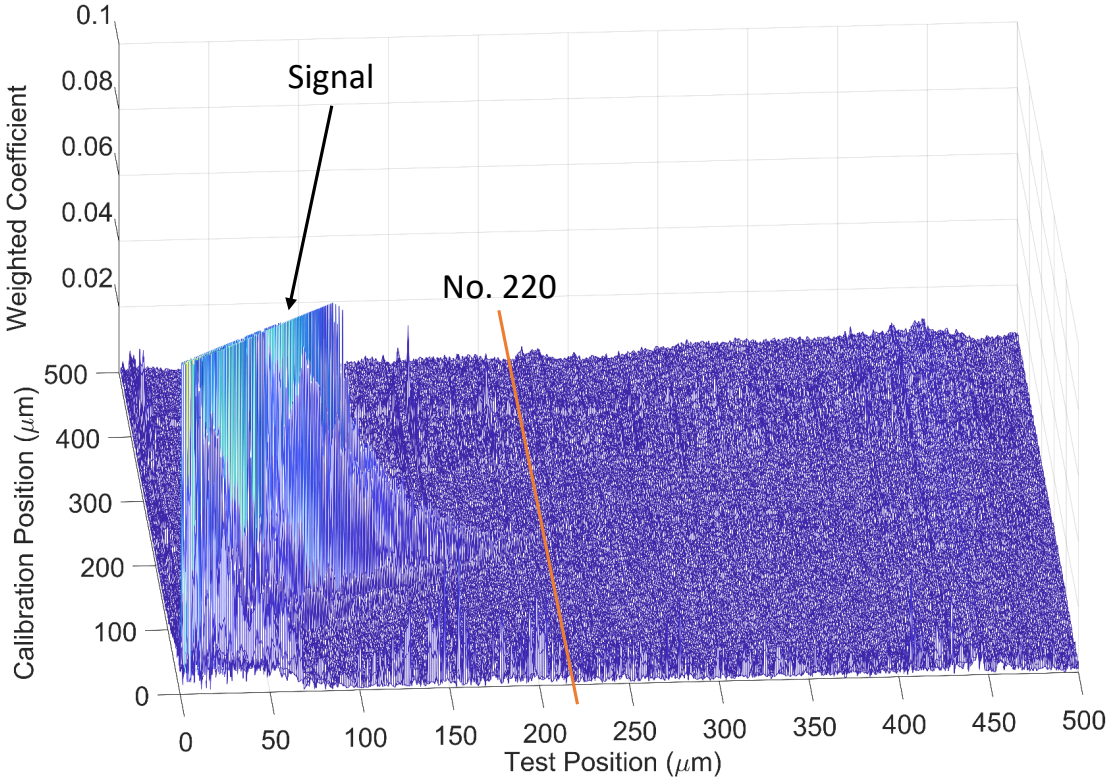


FIGURE 5.17: 3D plot of weight coefficient $S$ of the system range. $x$ axis shows test number of test group, and $y$ axis shows the calibration groups position. The correlation is strong until test data number 220 which corresponds to 220 $\mu$m. After that the signal becomes weak.

pattern are not recognizable by the algorithm and hence it cannot assign strong weighting to any particular position value.

Fig. 5.18 shows the modified speckle patterns (after background removing process) at 220 $\mu$m for (a) 850 nm center 50 nm bandwidth source and (b) 830 nm center 25 nm bandwidth source. The images are cropped from 1024 $\times$ 1280 images. In Fig. 5.18(b) we can see the strong interference fringes which enable the algorithm to recognize and link to the position information. However, Fig.5.18(a) seems more random. Also, from the colorbar we can see the dynamic range of Fig. 5.18(b) is larger than Fig. 5.18(a). To quantify the image quality, we calculated the first eigenvalues for both images, yielding 18.6 for Fig 5.18(a) and 935.8 for Fig. 5.18(b), where a larger number implies better features for analysis.

The resolution of the scattering chip spectrometer for WLI was evaluated by reducing the calibration step increment to 5 nm. The result in Fig. 5.19 shows the reconstructed positions for 200 test speckle patterns as due to the time required for the high resolution calibration, our test of resolution was limited to a 1 $\mu$m range. The results confirm that the method can resolve 28 nm changes in distance.

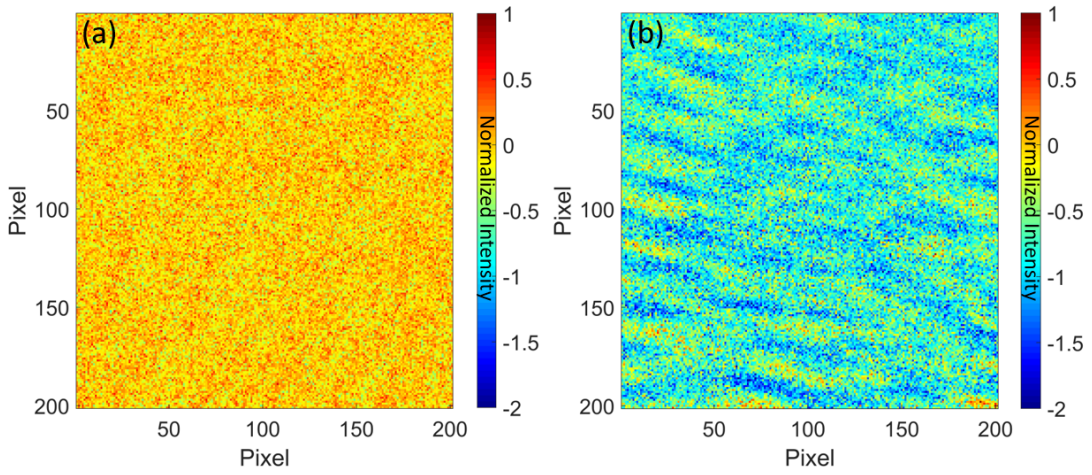


FIGURE 5.18: Speckle patterns at 220 $\mu$m with (a) 850 nm SLED source with 50 nm bandwidth and (b) 830 nm source with 25 nm bandwidth. The images are cropped from 1024 $\times$ 1280 full size speckle patterns.

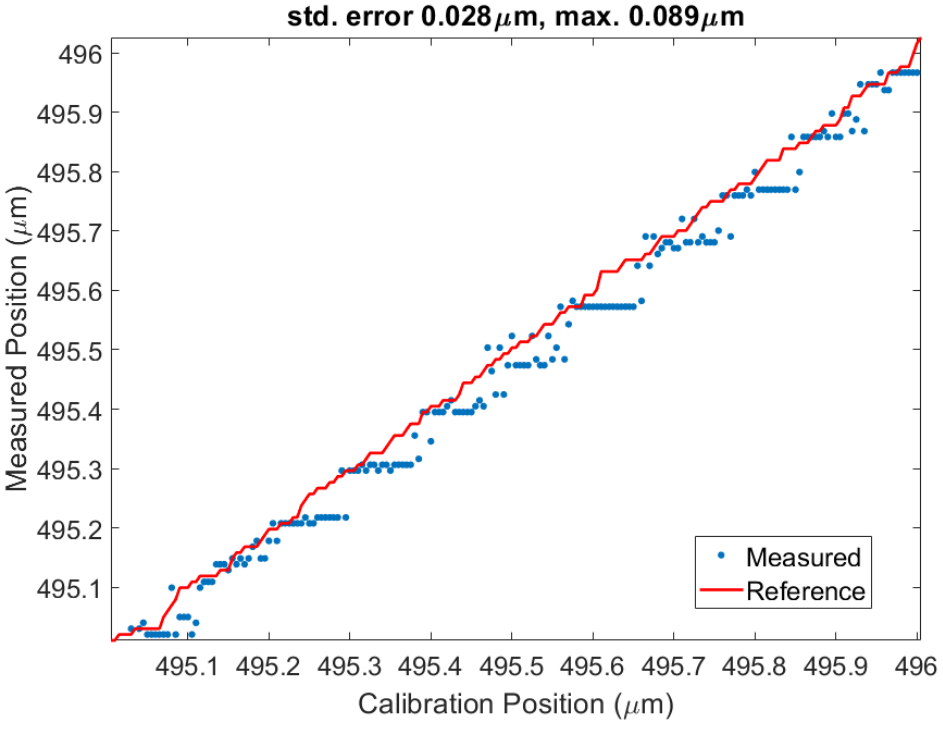


FIGURE 5.19: Resolution test of the scattering chip for WLI position measurements. The blue marker shows the reconstructed position from speckle pattern of test group. Calibration increment is set to 5 nm over the 1 $\mu$m range.

At present the resolution of the method is limited by the positional accuracy and noise of the PZT control loop. The PI Hera PZT used for calibration has a resolution of 1.5 nm; however the range of 500 $\mu$m reduces the stiffness of the assembly and hence has an accuracy of around 20 nm. A shorter range and stiffer PZT would allow calibration at a higher resolution, though increasing the number of calibration steps will have penalties for calibration time and the achievable signal processing rate.

#### 5.4.4.2 Topography Measurement

Following investigation of range, linearity and resolution of the scattering chip WLI setup, the PZT $z$-axis translation stage was replaced by a linear stepper motor. This configuration allows lateral translation of a measurement sample in the $y$ axis direction to record a 2D profile measurement.

A Rubert step height sample (Rubert 513, ISO 5436), with steps of 30, 200, 500 and 1000 $\mu$m, was placed in front of the WLI Michelson probe and the pitch/yaw of the sample adjusted to maximise returned light power into the fibre. A 4 mm lateral scan of the 30 $\mu$m step was performed with a speckle pattern captured at translation stage intervals of 0.01 mm resulting in 400 measured speckle patterns.

Next, the captured measurement data set was post-processed in MATLAB using a 200 $\mu$m range calibration set of speckle patterns, resulting in the D profile measurement of step height seen in Fig. 5.20. The slope shape of the measured position results from a slightly angled position (0.21°) of the sample during the measurement. The measured position was reconstructed to a real sample profile (red dash line) according to the linear fit by least squares method. Notice there are a few surface positions jumps at the 0 $\mu$m positions; this is the edge effect of the system. When the probe beam incidents onto the groove edge, the reflection will be weaker thus giving a lower signal feedback level. The algorithm would then recognize the position as the start position which is at 0 $\mu$m. The edge effect will manifest clearly at abrupt profile changes of the sample.

The measured width of the sample is 0.5 mm which is the same as the real sample. The measured depth has a 0.3 $\mu$m error compared to the real sample depth of 30 $\mu$m. As the scattering chip is very sensitive to the position change, averaging over multiple measurements would improve the accuracy. Also, the calibration step of 0.1 $\mu$m gives a $\pm$0.2 $\mu$m error in the measurement.

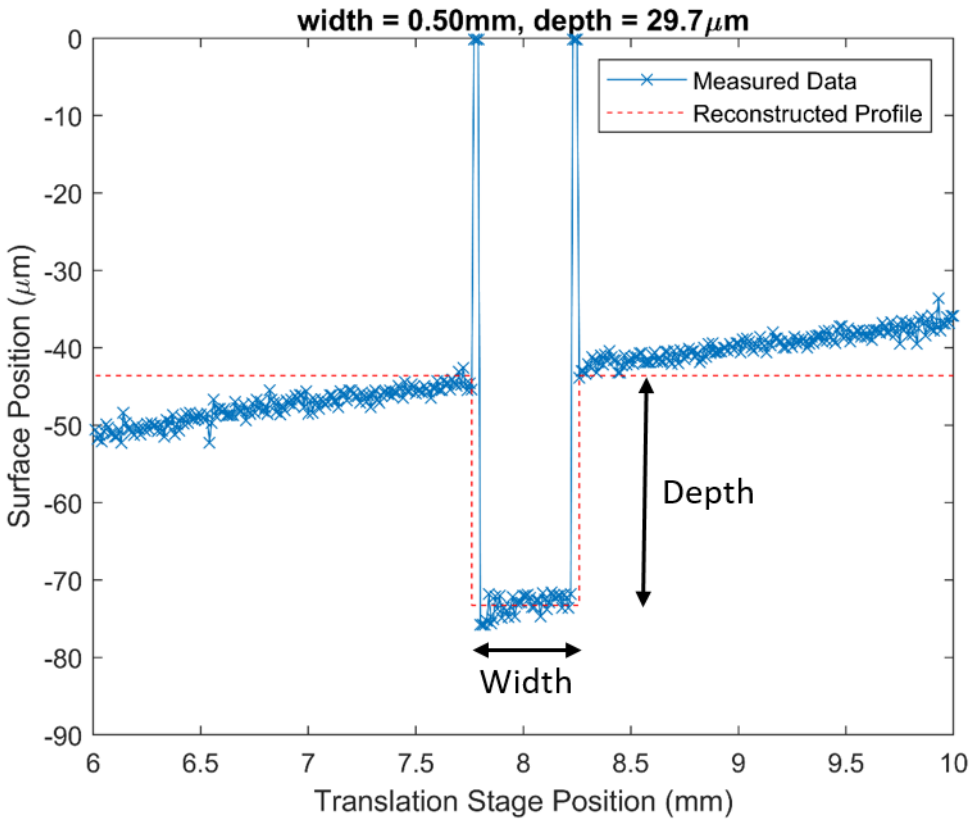


FIGURE 5.20: Measured profile of Rubert 513 step sample. The blue cross shows the raw reconstructed position. The red dashed line shows the reconstructed sample profile after accounting for levelling and edge-effects.

## 5.5 Conclusions

A laser-fabricated scattering chip based on induced voids was presented in this chapter, with applications as a wavemeter, spectrometer, and interferometric distance sensor. The layout of the voids was designed in MATLAB as random matrix layers. To investigate the scattering efficiency, a Mie scattering simulation was undertaken for a single sphere scatterer. For the experimental writing, a chip with 70% scattering efficiency was achieved by optimising the laser writing parameters. In terms of working principle, the wavemeter is based on correlation while the spectrometer relies on the singular value decomposition technique. The wavelength and spectral reconstruction capabilities were confirmed, and the chip only needs ∼100 pixels to reconstruct the wavelength without error, for a 0.2 nm resolution. During a 120-hour stability test, the chip showed only 122 pm error. As part of a distance sensor assisted with white light interferometry, the scattering chip was able to measure distance with a range of 500 $\mu$m. Finally, a topography measurement was done with a step sample, in which the scattering chip achieved 0.3 $\mu$m accuracy.

# Chapter 6

# Future Work and Conclusions

## 6.1 Future Work

### 6.1.1 Diffractive Optics Elements

Over the course of this work, we have obtained high-efficiency gratings and applied the optimised writing parameters to produce efficient Fresnel lenses. Since the Fresnel lens shows anomalous dispersion, we could integrate the Fresnel lens within a traditional refractive lens to create a hybrid lens with the potential to compensate for the chromatic dispersion. This utilises the ability of fs laser writing technology to inscribe embedded structures with precision. Fig. 6.1 shows three possible steps towards the embedded Fresnel lens which we could try.

### 6.1.2 Scattering Media Based Devices

#### 6.1.2.1 Scattering Chip Spectrometer

Unlike traditional grating-based spectrum analysers, the scattering spectrometer has the nature of increasing optical path length by scattering within the chip. Therefore, scattering has the potential to achieve better spectral resolution at the same size as the traditional spectrometer. Furthermore, the chip is fabricated from silica which is cheap and stable, allowing a wide range of uses in daily life.

Spectrometers are not only highly important for their academic use, but also a very common component in many commercial products. In the future, the chip can either be developed as a tiny compact device integrated with a portable device to offer a moderate spectral resolution for daily use, or on the other hand, developed as a chip and low-cost compact spectrometer device for academic use.

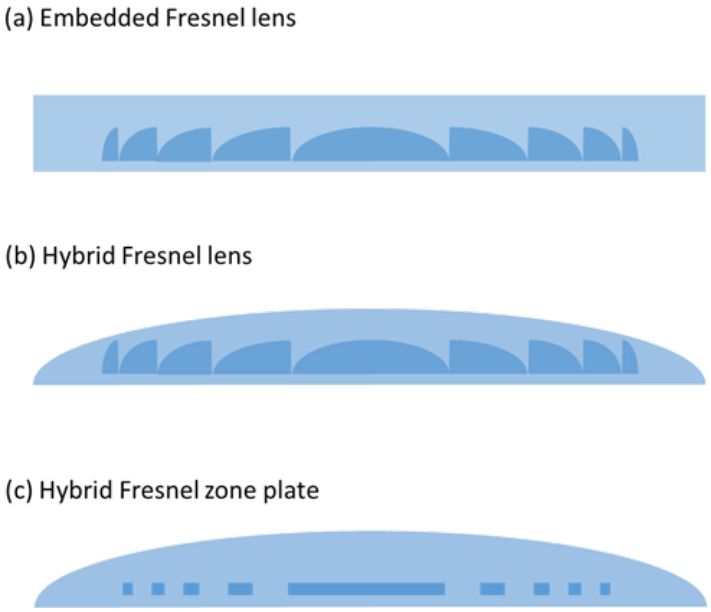


FIGURE 6.1: Three types of embedded optical elements: (a) Fresnel lens embedded in a planar substrate, (b) hybrid Fresnel lens, a combination of a refractive lens and Fresnel lens, and (c) hybrid Fresnel zone plate.

#### 6.1.2.2 "Light Converter"

The chip is not limited to its application as a spectrometer, as several properties of the input light can be converted to significant speckle pattern changes via the scattering process. In this thesis, we have also presented one of them, which is the scattering chip assisted white light interferometry system for distance measurement. Besides this, there are a few more applications we can try in the future:

- FBG assisted strain sensor:
  Fibre Bragg gratings (FBGs) are widely used as sensors. When we launch light inside the FBG, the grating will reflect a specific wavelength. FBG sensors often operate by detecting shifts in this reflected wavelength using an OSA. However, with a scattering chip, this shift will be converted to a speckle pattern change, so strain applied to the fibre can be detected.
- Temperature monitor:
  In this thesis, when we conducted the stability test over one week, we found the speckle pattern changes with temperature variations. In the future, we could investigate the scattering chip as a thermometer. Using a chip substrate with large thermo-optic and thermal expansion coefficients would be advantageous in this situation.
- Polarimeter:
  In the laser induced stress distribution section, we found that when writing with different polarisation states, there were different types of damage appearing in

the written structure. The scattering and transmission properties of nanograting damage are polarisation dependent. Additionally, depending on the induced anisotropy and local stress directions, different polarisations can experience a different refractive index when propagating in the scattering matrix. For the scattering chip, if we could alter the polarization dependence of the laser writing, the scattering chip can respond differently for different polarizations. Thus, by analysing the speckle pattern, we could reconstruct the input polarization state.

## 6.2 Conclusions

In this thesis, we presented the developments of optical devices based on fs laser direct writing in transparent material, including waveguides, Fresnel lenses, diffractive gratings and scattering based chips. A computer controlled direct writing system using a 1.03 $\mu$m 200 fs pulsed femtosecond laser has been set up. For inscription, we used either a 1030 nm wavelength femtosecond laser beam or its second harmonic at 515 nm focused onto a sample. The inscription region can be scanned in 3D using the $x$-$y$ and $z$ translation stages, which are computer controlled via a stage-controller with the help of fabrication design software to compose the scanline paths. For inscribing waveguides and scattering points, we simply focus the writing beam using an objective into the substrate, whereas to fabricate diffractive elements, we may also introduce an axicon to generate a Bessel beam. This allows us to optimise the beam focus profile according to the geometry under fabrication.

For estimating the laser induced refractive index change, waveguides were inscribed and investigated. The laser writing parameters were tested by fabricating waveguide structures. By calculating the output mode field diameter of the waveguide's fundamental mode, the laser induced refractive index was estimated as $7\times10^{-4}$ to $6\times10^{-3}$ for writing powers of $P_w$=35 mW to 55 mW. Then, based on the waveguide writing method, a stress control technique for femtosecond laser written structures was investigated. With this technique, we are able to eliminate the structural asymmetry in the index profile and stress distribution of waveguide-like structures, which would be present using the conventional multiscan writing approach. A more symmetric stress profile also improves the damage threshold so higher writing powers can be used, giving stronger $\Delta n$ and phase change. For high aspect-ratio Bessel beam written diffractive optics elements, a 36% diffraction efficiency improvement for a 50/50 grating was achieved compared to the standard multiscan writing technique. A two-layer Fresnel lens with a focal efficiency of 55% was also demonstrated. For low aspect-ratio Gaussian beam written waveguides, a more symmetric mode profile was achieved using the improved scanning technique. Finally, as for the application side, the waveguide writing technique was applied to

fabricate a multicore fibre based bending sensor capable of resolving bend direction, for which a sensitivity of -1.4 nm/degree was achieved.

For the diffractive elements, the design and propagation simulation of the Fresnel zone plate were investigated. According to simulations, the diffractive FZP shows anomalous dispersion; and up to 85% and 95% diffraction efficiency can be achieved when focusing a plane wave and Gaussian beam input, respectively. For the experimental fabrication, a Bessel beam inscribed waveguide can achieve a height of $\sim$100 $\mu m$, which is 5 times greater than that of Gaussian beam writing. Then, through experimental characterisation, the Bessel beam written FZPs were confirmed to show anomalous dispersion. In terms of imaging, the FZPs were able to resolve down to 200 $\mu m$ spaced array lines with clarity. For multi-layer FZPs, we achieved a 59% diffraction efficiency with a 3-layer FZP. In the grating writing section, 57% diffraction efficiency was achieved in SF57 lead silicate glass with Gaussian beam writing. For Bessel beam writing, by measuring the diffraction efficiency, the index change has been estimated and characterised for different laser power and pulse density.

A laser-fabricated scattering chip was presented in the previous chapter. It was designed with MATLAB code as the random matrix layers. To investigate the scattering efficiency, a Mie scattering simulation has been done with a single sphere scatterer. For the experimental writing, a chip with 70% scattering efficiency has been obtained by optimising the laser writing parameters. The working mechanism of the scattering chip worked as a wavemeter and spectrometer has been discussed, where the wavemeter is based on the speckle correlation and spectrometer is based on the singular value decomposition. The wavelength and spectrum reconstruction has been investigated. The chip only needs $\sim$100 pixels to reconstruct the wavelength with no error. During a 120-hour stability test, the chip has 122 pm error. The scattering chip is also able to measure distance over a range of 500 $\mu$m when assisted with the white light interferometry system. Finally, a topography measurement performed with a step sample confirmed a 0.3 $\mu$m distance accuracy was achieved.

Based on the discussion from this thesis, potential future developments for the diffractive elements include integrating the Fresnel lens into a traditional lens by utilising the flexibility of fs laser writing for more compact lens assemblies. For the scattering chip, we could use it as a ”light converter” which converts strain, temperature or polarization state into speckle patterns. By analysing changes in the speckle patterns, such changes in the properties of the input light or local environment would thus be readily discernible. The inherently low-cost and compact nature of the embedded diffractive elements and scattering chip lend themselves to many exciting applications, which will no doubt evolve and emerge through both academic and commercial spheres in the years to come.

# Appendix A

# Publications

Journal Papers:

- Sun, Q., Lee, T., Beresna, M. and Brambilla, G., 2020. Control of laser induced cumulative stress for efficient processing of fused silica. Scientific reports, 10(1), pp.1-8.
- Arrizabalaga, O., Sun, Q., Beresna, M., Lee, T., Zubia, J., Pascual, J.V., de Ocáriz, I.S., Schülzgen, A., Antonio-Lopez, J.E., Amezcua-Correa, R. and Villatoro, J., 2020. High-performance vector bending and orientation distinguishing curvature sensor based on asymmetric coupled multi-core fibre. Scientific reports, 10(1), pp.1-10.
- Jiang, X., Lee, T., Chen, M., Sun, Q., He, J. and Brambilla, G., 2019. Enhanced UV third-harmonic generation in microfibers by controlling nonlinear phase modulations. Optics letters, 44(17), pp.4191-4194.

In preparation:

- A Scattering Spectrometer For White Light Interferometry
- Compact Spectrometer Chips Based on Fs Laser Written Multi-layer Scattering Medium
- Low bend loss femtosecond laser written waveguides exploiting integrated microcrack
- A new technology for fabricating multi parameter optical gauges based on mode coupling effect in asymmetric index multi-core fibres

Conference Papers:

- Sun, Q., Vettenburg, T., Lee, T., Phillips, D., Beresna, M. and Brambilla, G., 2019, November. Compact spectrometer chips based on fs laser written multi-layer scattering medium. In Asia Communications and Photonics Conference (pp. T4D-5). Optical Society of America.
- Sun, Q., Lee, T., Beresna, M. and Brambilla, G., 2019, June. Control of Laser Induced Stress for Diffractive Optics in Transparent Media. In The European Conference on Lasers and Electro-Optics (p. cm_5_1). Optical Society of America.
- Q. Sun, T. Lee, Z. Ding, M. Beresna, and G. Brambilla, "Diffractive Fresnel Lens Fabrication with Femtosecond Bessel Beam Writing in Silica," in Frontiers in Optics / Laser Science, OSA Technical Digest (Optical Society of America, 2018), paper JW3A.12.
- T. Lee, Q. Sun, R. Ismaeel, M. Castro-Lopez, C. Bocheng, M. Beresna, and G. Brambilla, "Femtosecond Written Silica Waveguides for High Extinction Polarization Filtering," in Frontiers in Optics / Laser Science, OSA Technical Digest (Optical Society of America, 2018), paper JTu3A.16.
- Lee, T., Sun, Q., Ismaeel, R., Beresna, M. and Brambilla, G., 2019, June. Low Bend Loss Femtosecond Written Waveguides Exploiting Microcrack Enhanced Modal Confinement. In The European Conference on Lasers and Electro-Optics (p. cm_4_5). Optical Society of America.
- Wang, Y., Khudus, M.A., De Lucia, F., Sun, Q., He, J., Sazio, P.J., Ismaeel, R., Beresna, M., Horak, P. and Brambilla, G., 2016, October. UV generation in silica fibres. In Frontiers in Optics (pp. FTu1I-1). Optical Society of America.

# References

Anand Agarwal and Minoru Tomozawa. Correlation of silica glass properties with the infrared spectra. *Journal of Non-Crystalline Solids*, 209(1-2):166–174, 1997.

Oskar Arrizabalaga, Qi Sun, Martynas Beresna, Timothy Lee, Joseba Zubia, Javier Velasco Pascual, Idurre Sáez de Ocáriz, Axel Schülzgen, Jose Enrique Antonio-Lopez, Rodrigo Amezcua-Correa, et al. High-performance vector bending and orientation distinguishing curvature sensor based on asymmetric coupled multi-core fibre. *Scientific reports*, 10(1):1–10, 2020.

Yves Bellouard, Ali Said, Mark Dugan, and Philippe Bado. Fabrication of high-aspect ratio, micro-fluidic channels and tunnels using femtosecond laser pulses and chemical etching. *Opt. Express*, 12(10):2120–2129, May 2004. . URL http://www.opticsexpress.org/abstract.cfm?URI=oe-12-10-2120.

Yves Bellouard, E Barthel, AA Said, M Dugan, and Ph Bado. Scanning thermal microscopy and raman analysis of bulk fused silica exposed to low-energy femtosecond laser pulses. *Optics Express*, 16(24):19520–19534, 2008.

Yves Bellouard, Audrey Champion, Benjamin McMillen, Sebabrata Mukherjee, Robert R. Thomson, Charles Pépin, Philippe Gillet, and Ya Cheng. Stress-state manipulation in fused silica via femtosecond laser irradiation. *Optica*, 3(12): 1285–1293, Dec 2016. . URL http://www.osapublishing.org/optica/abstract.cfm?URI=optica-3-12-1285.

Martynas Beresna, Mindaugas Gecevičius, Peter G Kazansky, and Titas Gertus. Radially polarized optical vortex converter created by femtosecond laser nanostructuring of glass. *Applied Physics Letters*, 98(20):201101, 2011.

Martynas Beresna, Mindaugas Gecevičius, and Peter G Kazansky. Ultrafast laser direct writing and nanostructuring in transparent materials. *Advances in Optics and Photonics*, 6(3):293–339, 2014.

Erica Bricchi, John D Mills, Peter G Kazansky, Bruce G Klappauf, and Jeremy J Baumberg. Birefringent fresnel zone plates in silica fabricated by femtosecond laser machining. *Optics letters*, 27(24):2200–2202, 2002.

Audrey Champion and Yves Bellouard. Direct volume variation measurements in fused silica specimens exposed to femtosecond laser. *Opt. Mater. Express*, 2(6): 789–798, Jun 2012. . URL http://www.osapublishing.org/ome/abstract.cfm?URI=ome-2-6-789.

Audrey Champion, Martynas Beresna, Peter Kazansky, and Yves Bellouard. Stress distribution around femtosecond laser affected zones: effect of nanogratings orientation. *Opt. Express*, 21(21):24942–24951, Oct 2013. . URL http://www.opticsexpress.org/abstract.cfm?URI=oe-21-21-24942.

James W Chan, Thomas Huser, S Risbud, and DM Krol. Structural changes in fused silica after exposure to focused femtosecond laser pulses. *Optics letters*, 26(21): 1726–1728, 2001.

George Y Chen, Fiorina Piantedosi, Dale Otten, Yvonne Qiongyue Kang, Wen Qi Zhang, Xiaohong Zhou, Tanya M Monro, and David G Lancaster. Femtosecond-laser-written microstructured waveguides in bk7 glass. *Scientific reports*, 8(1):1–7, 2018.

F Courvoisier, P-A Lacourt, M Jacquot, MK Bhuyan, L Furfaro, and JM Dudley. Surface nanoprocessing with nondiffracting femtosecond bessel beams. *Optics letters*, 34(20):3163–3165, 2009.

K Miura Davis, Kiyotaka Miura, Naoki Sugimoto, and Kazuyuki Hirao. Writing waveguides in glass with a femtosecond laser. *Optics letters*, 21(21):1729–1731, 1996.

Marti Duocastella and Craig B Arnold. Bessel and annular beams for materials processing. *Laser & Photonics Reviews*, 6(5):607–621, 2012.

J Durnin. Exact solutions for nondiffracting beams. i. the scalar theory. *JOSA A*, 4(4): 651–654, 1987.

J Durnin, JH Eberly, and JJ Miceli. Comparison of bessel and gaussian beams. *Optics letters*, 13(2):79–80, 1988.

Shane M Eaton, Haibin Zhang, Peter R Herman, Fumiyo Yoshino, Lawrence Shah, James Bovatsek, and Alan Y Arai. Heat accumulation effects in femtosecond laser-written waveguides with variable repetition rate. *Optics Express*, 13(12): 4708–4716, 2005.

Shane M. Eaton, Mi Li Ng, Roberto Osellame, and Peter R. Herman. High refractive index contrast in fused silica waveguides by tightly focused, high-repetition rate femtosecond laser. *Journal of Non-Crystalline Solids*, 357(11-13):2387–2391, jun 2011. .

Rafael R Gattass and Eric Mazur. Femtosecond laser micromachining in transparent materials. *Nature photonics*, 2(4):219–225, 2008.

Eli N Glezer and Eric Mazur. Ultrafast-laser driven micro-explosions in transparent materials. *Applied physics letters*, 71(7):882–884, 1997.

EN Glezer, M Milosavljevic, L Huang, RJ Finlay, T-H Her, J Paul Callan, and Eric Mazur. Three-dimensional optical storage inside transparent materials. *Optics letters*, 21(24):2023–2025, 1996.

Hengchang Guo, Hongbing Jiang, Ying Fang, Chao Peng, Hong Yang, Yan Li, and Qihuang Gong. The pulse duration dependence of femtosecond laser induced refractive index modulation in fused silica. *Journal of Optics A: Pure and Applied Optics*, 6(8):787, 2004.

Fei He, Junjie Yu, Yuanxin Tan, Wei Chu, Changhe Zhou, Ya Cheng, and Koji Sugioka. Tailoring femtosecond 1.5-$\mu$m bessel beams for manufacturing high-aspect-ratio through-silicon vias. *Scientific reports*, 7:40785, 2017.

J Higbie. Fresnel zone plate: Anomalous foci. *American Journal of Physics*, 44(10): 929–930, 1976.

C. Hnatovsky, R. S. Taylor, P. P. Rajeev, E. Simova, V. R. Bhardwaj, D. M. Rayner, and P. B. Corkum. Pulse duration dependence of femtosecond-laser-fabricated nanogratings in fused silica. *Applied Physics Letters*, 87(1):014104, jul 2005a. ISSN 0003-6951. . URL http://aip.scitation.org/doi/10.1063/1.1991991.

C Hnatovsky, RS Taylor, PP Rajeev, E Simova, VR Bhardwaj, DM Rayner, and PB Corkum. Pulse duration dependence of femtosecond-laser-fabricated nanogratings in fused silica. *Applied Physics Letters*, 87(1):014104, 2005b.

C. Hnatovsky, R.S. Taylor, E. Simova, P.P. Rajeev, D.M. Rayner, V.R. Bhardwaj, and P.B. Corkum. Fabrication of microchannels in glass using focused femtosecond laser radiation and selective chemical etching. *Applied Physics A*, 84(1):47–61, Jul 2006. ISSN 1432-0630. . URL https://doi.org/10.1007/s00339-006-3590-4.

Andrius Marcinkevičius, Saulius Juodkazis, Mitsuru Watanabe, Masafumi Miwa, Shigeki Matsuo, Hiroaki Misawa, and Junji Nishii. Femtosecond laser-assisted three-dimensional microfabrication in silica. *Opt. Lett.*, 26(5):277–279, Mar 2001. . URL http://ol.osa.org/abstract.cfm?URI=ol-26-5-277.

Michael Mazilu, Tom Vettenburg, Andrea Di Falco, and Kishan Dholakia. Random super-prism wavelength meter. *Optics letters*, 39(1):96–99, 2014.

D McGloin and K Dholakia. Bessel beams: diffraction in a new light. *Contemporary Physics*, 46(1):15–28, 2005.

John H McLeod. The axicon: a new type of optical element. *JOSA*, 44(8):592–597, 1954.

Ben McMillen and Yves Bellouard. On the anisotropy of stress-distribution induced in glasses and crystals by non-ablative femtosecond laser exposure. *Opt. Express*, 23(1): 86–100, Jan 2015. . URL http://www.opticsexpress.org/abstract.cfm?URI=oe-23-1-86.

Ben McMillen, Christos Athanasiou, and Yves Bellouard. Femtosecond laser direct-write waveplates based on stress-induced birefringence. *Optics Express*, 24 (24):27239–27252, 2016.

Nikolaus Klaus Metzger, Roman Spesyvtsev, Graham D Bruce, Bill Miller, Gareth T Maker, Graeme Malcolm, Michael Mazilu, and Kishan Dholakia. Harnessing speckle for a sub-femtometre resolved broadband wavemeter and laser stabilization. *Nature communications*, 8:15610, 2017.

Mindaugas Mikutis, Tadas Kudrius, Gintas Šlekys, Domas Paipulas, and Saulius Juodkazis. High 90% efficiency bragg gratings formed in fused silica by femtosecond gauss-bessel laser beams. *Optical Materials Express*, 3(11):1862–1871, 2013.

Yusuke Nasu, Masaki Kohtoku, and Yoshinori Hibino. Low-loss waveguides written with a femtosecond laser for flexible interconnection in a planar light-wave circuit. *Optics letters*, 30(7):723–725, 2005.

Roberto Osellame, N Chiodo, V Maselli, A Yin, Margherita Zavelani-Rossi, G Cerullo, Paolo Laporta, L Aiello, S De Nicola, P Ferraro, et al. Optical properties of waveguides written by a 26 mhz stretched cavity ti: sapphire femtosecond oscillator. *Optics Express*, 13(2):612–620, 2005.

I Pavlov, O Tokel, S Pavlova, V Kadan, G Makey, A Turnali, Ö Yavuz, and FÖ Ilday. Femtosecond laser written waveguides deep inside silicon. *Optics letters*, 42(15): 3028–3031, 2017.

Brandon Redding and Hui Cao. Using a multimode fiber as a high-resolution, low-loss spectrometer. *Optics letters*, 37(16):3384–3386, 2012.

Brandon Redding, Seng Fatt Liew, Raktim Sarma, and Hui Cao. Compact spectrometer based on a disordered photonic chip. *Nature Photonics*, 7(9):746, 2013a.

Brandon Redding, Sebastien M Popoff, and Hui Cao. All-fiber spectrometer based on speckle pattern reconstruction. *Optics express*, 21(5):6584–6600, 2013b.

Brandon Redding, Mansoor Alam, Martin Seifert, and Hui Cao. High-resolution and broadband all-fiber spectrometers. *Optica*, 1(3):175–180, 2014.

Nicolas Riesen, Simon Gross, John D Love, and Michael J Withford. Femtosecond direct-written integrated mode couplers. *Optics express*, 22(24):29855–29861, 2014.

Jan-Patrick Schäfer. *Implementierung und Anwendung analytischer und numerischer Verfahren zur Lösung der Maxwellgleichungen für die Untersuchung der Lichtausbreitung in biologischem Gewebe*. PhD thesis, 2011.

Lawrence Shah, Alan Y Arai, Shane M Eaton, and Peter R Herman. Waveguide writing in fused silica with a femtosecond fiber laser at 522 nm and 1 mhz repetition rate. *Optics Express*, 13(6):1999–2006, 2005.

Pornsak Srisungsitthisunti, Okan K Ersoy, and Xianfan Xu. Laser direct writing of volume modified fresnel zone plates. *JOSA B*, 24(9):2090–2096, 2007.

Pornsak Srisungsitthisunti, Okan K. Ersoy, and Xianfan Xu. Beam propagation modeling of modified volume fresnel zone plates fabricated by femtosecond laser direct writing. *J. Opt. Soc. Am. A*, 26(1):188–194, Jan 2009. . URL http://josaa.osa.org/abstract.cfm?URI=josaa-26-1-188.

Alexander M Streltsov and Nicholas F Borrelli. Fabrication and analysis of a directional coupler written in glass by nanojoule femtosecond laser pulses. *Optics Letters*, 26(1):42–43, 2001.

Alexander M Streltsov and Nicholas F Borrelli. Study of femtosecond-laser-written waveguides in glasses. *JOSA B*, 19(10):2496–2504, 2002.

LIONEL Sudrie, Michel Franco, Bernard Prade, and André Mysyrowicz. Writing of permanent birefringent microlayers in bulk fused silica with femtosecond laser pulses. *Optics Communications*, 171(4-6):279–284, 1999.

H Sugiura and T Yamadaya. Raman scattering in silica glass in the permanent densification region. *Journal of non-crystalline solids*, 144:151–158, 1992.

Qi Sun, Timothy Lee, Ziqian Ding, Martynas Beresna, and Gilberto Brambilla. Diffractive fresnel lens fabrication with femtosecond bessel beam writing in silica. *Frontiers in Optics / Laser Science*, page JW3A.12, 2018. URL http://www.osapublishing.org/abstract.cfm?URI=FiO-2018-JW3A.12.

Qi Sun, Tom Vettenburg, Timothy Lee, David Phillips, Martynas Beresna, and Gilberto Brambilla. Compact spectrometer chips based on fs laser written multi-layer scattering medium. In *Asia Communications and Photonics Conference*, pages T4D–5. Optical Society of America, 2019.

Qi Sun, Timothy Lee, Martynas Beresna, and Gilberto Brambilla. Control of laser induced cumulative stress for efficient processing of fused silica. *Scientific reports*, 10 (1):1–8, 2020.

Joel Villatoro, Oskar Arrizabalaga, Gaizka Durana, Idurre Sáez de Ocáriz, Enrique Antonio-Lopez, Joseba Zubia, Axel Schülzgen, and Rodrigo Amezcua-Correa.

Accurate strain sensing based on super-mode interference in strongly coupled multi-core optical fibres. *Scientific reports*, 7(1):1–7, 2017.

David George Voelz. *Computational fourier optics: a MATLAB tutorial*. SPIE press Bellingham, WA, 2011.

JK Wright. Theory of the electrical breakdown of gases by intense pulses of light. *Proceedings of the Physical Society (1958-1967)*, 84(1):41, 1964.

Kazuhiro Yamada, Wataru Watanabe, Yudong Li, Kazuyoshi Itoh, and Junji Nishii. Multilevel phase-type diffractive lenses in silica glass induced by filamentation of femtosecond laser pulses. *Optics letters*, 29(16):1846–1848, 2004.

Eikichi Yamashita, Shigeru Ozeki, and Kazuhiko Atsuki. Modal analysis method for optical fibers with symmetrically distributed multiple cores. *Journal of lightwave technology*, 3(2):341–346, 1985.

DA Yashunin, Yu A Malkov, LA Mochalov, and AN Stepanov. Fabrication of microchannels in fused silica using femtosecond bessel beams. *Journal of Applied Physics*, 118(9):093106, 2015.

Jingyu Zhang, A Čerkauskaitė, Rokas Drevinskas, Aabid Patel, Martynas Beresna, and Peter G Kazansky. Eternal 5d data storage by ultrafast laser writing in glass. In *Laser-based Micro-and Nanoprocessing X*, volume 9736, page 97360U. International Society for Optics and Photonics, 2016a.

YJ Zhang, GD Zhang, CL Chen, Razvan Stoian, and GH Cheng. Transmission volume phase holographic gratings in photo-thermo-refractive glass written with femtosecond laser bessel beams. *Optical Materials Express*, 6(11):3491–3499, 2016b.